



UPPSALA  
UNIVERSITET

*Digital Comprehensive Summaries of Uppsala Dissertations  
from the Faculty of Science and Technology 1220*

# Reconfigurable and Wideband Receiver Components for System-on-Chip Millimetre-Wave Radiometer Front-Ends

SHAKILA BINT REYAZ



ACTA  
UNIVERSITATIS  
UPSALIENSIS  
UPPSALA  
2015

ISSN 1651-6214  
ISBN 978-91-554-9145-1  
urn:nbn:se:uu:diva-239435

Dissertation presented at Uppsala University to be publicly examined in Högssalen, Ångströmlaboratoriet, Lägerhyddsvägen 1, Uppsala, Friday, 27 February 2015 at 13:15 for the degree of Doctor of Philosophy. The examination will be conducted in English. Faculty examiner: Professor Luca Roselli (University of Perugia, Italy).

### Abstract

Reyaz, S. B. 2015. Reconfigurable and Wideband Receiver Components for System-on-Chip Millimetre-Wave Radiometer Front-Ends. *Digital Comprehensive Summaries of Uppsala Dissertations from the Faculty of Science and Technology* 1220. 94 pp. Uppsala: Acta Universitatis Upsaliensis. ISBN 978-91-554-9145-1.

This thesis presents solutions and studies related to the design of reconfigurable and wideband receiver circuits for system-on-chip (SoC) radiometer front-ends within the millimetre-wave (mm-wave) range. Whereas many of today's mm-wave front-ends are bulky and costly due to having discrete RF components, single-chip receiver modules could potentially result in a wider use for emerging applications such as wireless communication, short range radar and passive imaging security sensors if realised with adequate performances and at a lower cost. Three main topics are considered in this thesis, monolithic integration of low-loss RF-MEMS (Dicke) switch networks and switched LNAs in MMIC/RFIC foundry processes, designs of SiGe wideband (IF) amplifier and broadband power detectors up to W-band (75-110 GHz).

Low-loss and high isolation GaAs and SiGe RF-MEMS switch networks were designed and characterised for the 30-110 GHz range. A GaAs MEMS Dicke switch network has a measured minimum loss of 1 dB and maximum isolation of 19 dB at 70-96 GHz, respectively, making it a potential candidate in Dicke switched radiometer receivers. Furthermore, single-chip 30 GHz and W-band MEMS Dicke switched LNA designs have been realised for the first time in SiGe BiCMOS and GaAs mHEMT processes, respectively.

For a targeted 94 GHz passive imaging application two different receiver topologies have been investigated based on direct-detection and direct-conversion (heterodyne) architectures. An optimised detector design fabricated in a 0.13  $\mu\text{m}$  SiGe process achieves a more wideband input matching than earlier silicon W-band detectors and is competitive with reported III-V W-band detectors in terms of a higher responsivity and similar NEP.

A SiGe 2-37 GHz high-gain differential (IF) amplifier design achieves a more wideband matching and an order of magnitude higher linearity than a recent single-ended SiGe LNA. The SiGe IF amplifier was integrated on-chip with a power detector in a 5-35 GHz IF section. Their broadband properties compared with other IF amplifier/detector RFICs, make them suitable for W-band down-conversion receivers with a larger pre-detection bandwidth and improved sensitivity. The experimental results successfully demonstrate the feasibility of the SiGe 5-35 GHz IF section for high performance SoC W-band radiometers using a more wideband heterodyne receiver architecture.

**Keywords:** Reconfigurable, Wideband, Receivers, Millimetre-Wave, Radiometers, System-on-Chip, Passive Imaging.

*Shakila Bint Reyaz, Department of Engineering Sciences, Solid State Electronics, Box 534, Uppsala University, SE-75121 Uppsala, Sweden.*

© Shakila Bint Reyaz 2015

ISSN 1651-6214

ISBN 978-91-554-9145-1

urn:nbn:se:uu:diva-239435 (<http://urn.kb.se/resolve?urn=urn:nbn:se:uu:diva-239435>)

*To the memory of Abbu and Ammi*



# List of Papers

This thesis is based on the following papers, which are referred to in the text by their Roman numerals.

- I     **S. Reyaz**, C. Samuelsson, R. Malmqvist, S. Seok, M. Fryziel, P.-A. Rolland, B. Grandchamp, P. Rantakari, and T. Vähä-Heikkilä, “W-Band RF-MEMS Dicke Switch Networks in a GaAs MMIC Process,” *Microwave and Optical Technology Letters*, Vol.: 55, Issue: 12, Page(s): 2849–2853, 2013.
- II    **S. Reyaz**, A. Gustafsson, C. Samuelsson, R. Malmqvist, B. Grandchamp, P. Rantakari, and T. Vähä-Heikkilä, “A W-Band RF-MEMS Switched LNA in a 70 nm mHEMT Process,” submitted to the *Int. Journal of RF and Microwave Computer-Aided Engineering*.
- III   **S. Reyaz**, C. Samuelsson, R. Malmqvist, M. Kaynak, and A. Rydberg, “Millimeter-Wave RF-MEMS SPDT Switch Networks in a SiGe BiCMOS Process Technology,” in *Proc. of European Microwave Integrated Circuits Conference (EuMIC)*, Amsterdam, The Netherlands, Oct. 2012, Page(s): 1071-1074.
- IV    **S. Reyaz**, C. Samuelsson, A. Gustafsson, R. Malmqvist, R. Jonsson, M. Kaynak, and A. Rydberg, “Monolithic Integration of an RF-MEMS Dicke Switch Network and a Wideband LNA in a 0.25  $\mu\text{m}$  SiGe BiCMOS Technology,” manuscript to be submitted to the *Int. Journal of Advances in Microelectronic Engineering*.
- V     R. Jonsson, R. Malmqvist, **S. Reyaz**, A. Rydberg, and M. Kaynak, “Design and Results of W-Band Power Detectors in a 130 nm SiGe BiCMOS Process Technology,” in *Proc. of European Microwave Integrated Circuits Conference (EuMIC)*, Rome, Italy, Oct. 2014, Page(s): 289-292.
- VI    R. Jonsson, **S. Reyaz**, R. Malmqvist, and M. Kaynak, “A W-Band Power Detector RFIC Design in 0.13 $\mu\text{m}$  SiGe BiCMOS

Process,” *Microwave and Optical Technology Letters* Vol.: 57, Issue: 2, Page(s): 414-417, 2015.

- VII **S. Reyaz**, R. Malmqvist, A. Gustafsson, and M. Kaynak, “SiGe BiCMOS High-Gain and Wideband Differential Intermediate Frequency Amplifier for W-Band Passive Imaging Single-Chip Receivers,” to be published in the *Int. Journal of IET Microwaves, Antennas and Propagation*, DOI: 10.1049/iet-map.2014.0511.
- VIII **S. Reyaz**, R. Jonsson, A. Gustafsson, R. Malmqvist, A. Strodl, V. Valenta, H. Schumacher, and M. Kaynak, “5-35 GHz Broadband IF Amplifier Section in 0.13- $\mu\text{m}$  SiGe Technology for W-Band Direct-Conversion Radiometers,” manuscript to be submitted to *Microwave and Optical Technology Letters*.

## Comments on the author’s contribution to the papers

- I. Simulations of the RF-MEMS circuits. Writing the manuscript. RF tests were done together with the co-author Carl Samuelsson.
- II. Simulations of the RF-MEMS and LNA circuits. Writing the manuscript. RF testing was done together with the co-authors Andreas Gustafsson, and Carl Samuelsson.
- III. Simulations of the RF-MEMS circuits. Writing the manuscript. Automated on-wafer tests were carried out at the foundry IHP.
- IV. Simulations of the RF-MEMS and LNA circuits. Writing the manuscript. On-chip measurements were made together with the co-author Andreas Gustafsson.
- V. Simulations of the input matching networks of the power detector designs and partially writing the manuscript. Circuit characterisations were made together with the co-author Rolf Jonsson.
- VI. Simulations of the wideband input matching network of the power detector and partially writing the manuscript. Measurements were done with the co-author Rolf Jonsson.
- VII. Design, layout and simulations of the IF amplifier. Writing the manuscript. Circuit characterisations were made together with the co-author Andreas Gustafsson.
- VIII. Design, layout and simulations of the IF amplifier. Writing the manuscript. Measurements were made in cooperation with the co-author Rolf Jonsson.

Reprints were made with permission from the respective publishers.

## Related Papers

The following Papers by the authors are not included due to an overlap in contents or a content which goes beyond the scope of this thesis.

- IX    **S. Reyaz**, C. Samuelsson, R. Malmqvist, M. Kaynak, and A. Rydberg, "A V-Band RF MEMS SPDT Switch Network in a SiGe BiCMOS Process Technology," MEMSWAVE 2012 International Conference, Antalya, Turkey, July 2012.
  
- X     **S. Reyaz**, C. Samuelsson, R. Malmqvist, M. Kaynak, A. Avlandapur, and A. Rydberg, "RF-MEMS Switching Circuits Fabricated in a SiGe Process Technology," Swedish Microwave Days, GigaHertz, Stockholm, Sweden 2012.
  
- XI    D. Dancila, R. Malmqvist, **S. B. Reyaz**, R. Augustine, C. Samuelsson, M. Kaynak, and A. Rydberg, "Wide Band On-Chip Slot Antenna with Back-Side Etched Trench for W-Band Sensing Applications," in Proc. of European Antennas and Propagation Conference (EuCAP), Gothenburg, Sweden, 2013, Pages: 1576-1579.
  
- XII   R. Malmqvist, C. Samuelsson, **S. Reyaz**, A. Gustafsson, S. Seok, P.-A Rolland, B. Grandchamps and R. Baggen, "A GaAs MMIC Single-Chip RF-MEMS Switched Tunable LNA," in Proc. of IEEE Compound Semiconductor Integrated Circuit Symposium (CSICS), Monterey, CA, Oct. 2013, Page(s): 1-4.
  
- XIII R. Jonsson, C. Samuelsson, **S. Reyaz**, R. Malmqvist, A. Gustafsson, and M. Kaynak, and Anders Rydberg, "SiGe Wideband Power Detector and IF-Amplifier RFICs for W-Band Passive Imaging Systems," in Proc. of IEEE Int. Semiconductor Conference (CAS), Sinaia, Romania, Oct. 2013, Page(s): 225-228.
  
- XIV R. Malmqvist, R. Jonsson, C. Samuelsson, A. Gustafsson, **S. Reyaz**, D. Dancila, A. Rydberg, B. Grandchamp, S. Seok, M. Fryziel, P.-A. Rolland, P. Rantakari, M. Lahti, T. Vähä-Heikkilä, and R. Baggen, "RF-MEMS Reconfigurable GaAs MMICs and Antennas for Microwave/MM-Wave Applications," in Proc. of IEEE Int. Semiconductor Conference (CAS), Sinaia, Romania, Oct. 2013, Page(s): 83-88.

- XV R. Malmqvist, C. Samuelsson, D. Dancila, **S. Reyaz**, M. Kaynak, and A. Rydberg, "Design and Test Results of a Wideband SiGe Detector and On-Chip Slot Antenna for W-Band Sensing Applications," in Proc. of IEEE Int. Semiconductor Conference (CAS), Sinaia, Romania, Oct. 2012, Page(s): 205-208.
- XVI R. Malmqvist, C. Samuelsson, A. Gustafsson, P. Rantakari, **S. Reyaz**, T. Vähä-Heikkilä, Anders Rydberg, J. Varis, D. Smith and R. Baggen, "A K-Band RF-MEMS Enabled Reconfigurable and Multifunctional Low-Noise Amplifier Hybrid Circuits," Active and Passive Electronic Components, Vol: 2011, Article ID 284767, 7 Pages, Hindawi Publishing Corporation, 2011.
- XVII R. Malmqvist, C. Samuelsson, W. Simon, D. Smith, P. Rantakari, T. Vähä-Heikkilä, **S. Reyaz**, J. Varis, and R. Baggen, "Reconfigurable Wideband LNAs Using Ohmic Contact and Capacitive RF-MEMS Switching Circuits," in Proc. of European Microwave Integrated Circuits Conference (EuMIC), Manchester, UK, Sept. 2011, Page(s): 160-163.
- XVIII R. Jonsson, C. Samuelsson, **S. Reyaz**, R. Malmqvist, D. Smith, M. Richard, P. Rantakari, T. Vähä-Heikkilä, and R. Baggen "An Experimental Study of Standard Packaged/Unpackaged GaAs MMIC based RF-MEMS Limiter Test Circuits," in Proc. of IEEE Int. Semiconductor Conference (CAS), Sinaia, Romania, Oct. 2011, Page(s): 203-206.



# Contents

1. Introduction and Outline .....	13
1.1 Motivation and Background .....	13
1.2 Aim and Contents of the Thesis .....	15
2. Background to RF and Microwave Circuits .....	16
2.1 RF/Millimetre-Wave Technology and Applications .....	16
2.2 MMIC and RFIC Technologies.....	16
2.2.1 MMIC Technology .....	17
2.2.2 RFIC Technology .....	18
2.3 RF Switches.....	19
2.3.1 Diode and Transistor based RF Switches .....	19
2.3.2 RF-MEMS Switches .....	20
2.4 Low Noise Amplifiers and Performance Parameters .....	21
2.5 Power Detectors .....	25
3. Receiver Architectures and Requirements for a W-Band Passive Imaging System .....	27
3.1 Architectures and Requirements .....	27
3.1.1 Direct-Detection Receivers ( <i>W-band power detector</i> ) .....	29
3.1.2 Direct-Conversion Receivers ( <i>IF amplifier and detector</i> ) .....	30
3.1.3 Millimetre-Wave <i>Dicke</i> Switch and Switched LNA.....	31
4. W-Band RF-MEMS Switch Networks in a 0.13 $\mu\text{m}$ GaAs pHEMT Process Technology .....	32
4.1 Motivation and Background .....	32
4.2 GaAs RF-MEMS Switch Designs and Results .....	33
4.2.1 RF-MEMS SPST Switch Network .....	33
4.2.2 W-Band RF-MEMS <i>Dicke</i> Switch Networks .....	34
4.3 Summary and Discussion .....	36
5. W-Band RF-MEMS Switched LNA MMIC in a 70 nm GaAs mHEMT Process .....	39
5.1 Motivation and Background .....	39
5.1.1 Target Specifications for a W-Band MEMS Switched LNA .....	40
5.2 W-Band RF-MEMS LNA Designs and Results .....	40
5.2.1 RF-MEMS <i>Dicke</i> Switched LNA ( <i>Micro-strip designs</i> ) .....	40
5.2.2 RF-MEMS <i>Dicke</i> Switched LNA ( <i>CPW designs</i> ) .....	41
5.3 Summary and Discussion .....	46

6. Millimetre-Wave RF-MEMS SPDT Switch Networks in a SiGe BiCMOS Process .....	48
6.1 Motivation and Background .....	48
6.2 SiGe RF-MEMS Switch Circuits and Results .....	49
6.2.1 RF-MEMS SPST Switch Network .....	49
6.2.2 RF-MEMS SPDT Switch Networks .....	50
6.3 Summary and Discussion .....	52
7. Monolithic Integration of a SiGe RF-MEMS Dicke Switch Network and a Wideband LNA .....	53
7.1 Motivation and Background .....	53
7.1.1 Target Specifications for a 30 GHz MEMS Switched LNA .....	54
7.2 SiGe RF-MEMS and LNA Designs and Results .....	55
7.2.1 RF-MEMS Dicke Switch Network .....	55
7.2.2 Wideband LNA .....	56
7.2.3 RF-MEMS Dicke Switched LNA .....	59
7.3 Summary and Discussion .....	60
8. Wideband SiGe Power Detectors for SoC W-Band Direct-Detection Radiometers .....	63
8.1 Motivation and Background .....	63
8.2 SiGe Power Detector Designs and Results .....	64
8.2.1 Detector design based on a narrow-band matching network .....	64
8.2.2 Detector design based on a wideband matching network .....	66
8.3 Summary and Discussion .....	68
9. Wideband SiGe IF Amplifier and IF Section for W-Band Direct-Conversion Radiometers .....	70
9.1 Differential IF Amplifier and IF Section .....	70
9.1.1 Motivation and Background .....	70
9.2 Differential Wideband IF Amplifier .....	71
9.2.1 Circuit Design and Results .....	71
9.2.2 Summary and Discussion .....	74
9.3 Differential Broadband IF Section .....	76
9.3.1 Circuit Design and Results .....	76
9.3.2 Summary and Discussion .....	77
10. Conclusions and Future Work .....	79
10.1 Conclusions .....	79
10.2 Future Work .....	81
11. Summary in Swedish .....	82
Acknowledgements .....	83
Bibliography .....	85

# Abbreviations

A/D	Analog/Digital
ADS	Advance Design System
BCB	Benzo-Cyclo-Butene
BEOL	Back-End-of-Line
CMOS	Complementary Metal Oxide Semiconductor
BiCMOS	Bipolar Complementary Metal Oxide Semiconductor
COTS	Commercially-off-the-shelf
CPW	CoPlanar Waveguide
DC	Direct Current
DR	Dynamic Range
EM	Electro-Magnetic
EMI	Electro-Magnetic-Interference
FET	Field Effect Transistor
$f_{\text{MAX}}$	Maximum Frequency of operation
$f_{\text{T}}$	Transition Frequency
FoM	Figure of Merit
GaAs	Gallium Arsenide
GaN	Gallium Nitride
HEMT	High Electron Mobility Transistor
HBT	Heterojunction Bipolar Transistor
III-V	(Ga, In-As, N, P) Compound Semiconductors
IC	Integrated Circuit
IF	Intermediate Frequency
IMD	Inter Modulation Distortion
InP	Indium Phosphide
IP3	Third Order Intercept Point
IIP3	Input Third Order Intercept Point
IR	Infra-Red
LNA	Low Noise Amplifier
LVS	Layout versus Schematic
MEMS	Micro-Electro-Mechanical-Systems
mHEMT	metamorphic High Electron Mobility Transistor
MIC	Microwave Integrated Circuit
MIM	Metal-Insulator-Metal
MMIC	Monolithic Microwave Integrated Circuit
MMW	Millimetre-Wave
NEP	Noise Equivalent Power

NETD	Noise Equivalent Temperature Difference
NF	Noise Figure
OIP3	Output Third Order Intercept Point
P1dB	1-dB Compression Point
pHEMT	pseudomorphic High Electron Mobility Transistor
PIN	P-type-Intrinsic-N-type
PMMW	Passive Millimetre Wave
RF	Radio Frequency
RFIC	Radio Frequency Integrated Circuit
SiGe	Silicon Germanium
S-Parameter	Scattering Parameter
SPDT	Single-Pole-Dual-Throw
SPST	Single-Pole-Single-Throw
SNR	Signal to Noise Ratio
SoC	System-on-Chip
TRL	Thru-Reflect-Line
W-Band	75-110 GHz waveguide frequency band

# 1. Introduction and Outline

This thesis begins with a short introduction to the subject of RF sensing and the motivation for the development of reconfigurable and wideband receiver components for radiometer front-ends operating in the 30-110 GHz range. The main objectives and the contents of this work are also summarised.

## 1.1 Motivation and Background

The frequency band between 30 to 300 GHz is denoted as the millimetre (mm) wave range since its free-space wavelength lies between 1 to 10 mm. Due to its inherent properties of large bandwidths and short wavelengths the mm-wave band has been proposed for high data rate transmission [1], high resolution radar systems [2], [3] and for small size on-chip antennas [4], [5]. In addition, single chip mm-wave receivers could enable more cost-efficient RF front-end solutions due to a smaller form factor at higher frequencies [6].

At mm-waves the propagation windows (frequency bands) that result in a relatively moderate atmospheric attenuation both in clear air and fog are centered around 35, 94, 140, and 220 GHz [7]. Within these windows the penetration properties of mm-waves through obstacles such as smoke, fog, dust and textiles (clothes etc.) are quite attractive for various “see-through” applications like remote sensing [8] and imaging [7] that are problematic for infra-red (IR) and visible imaging sensors. There are two approaches to perform mm-wave imaging using either an active or a passive system [9]. An active imaging system illuminates the target, and it receives the reflected signal. This can result in a higher signal-to-noise ratio (SNR) than passive imaging systems but at the expense of increased system complexity and the requirement for a uniformly illuminated target to mitigate shadow and glint problems [10]. A passive imager detects the naturally emitted thermal radiations from all objects in a scene and hence, no transmitter is needed but as a result of this the receiver sensitivity requirements are higher. A radiometer measures the average noise power (thermal radiations) over a specified frequency band. The simplest radiometer consists of a power detector, an integrator and a display. Radiometers are employed in space applications [11]–[13] and they have also been introduced in security applications [7]. For example; radiometers may be used at airports (portal passengers screening) to detect objects such as explosives and weapons hidden under clothes [14].

To improve the radiometer sensitivity, a high-gain low-noise amplifier (LNA) is often used in front of the power detector. The sensitivity or thermal resolution of the radiometer is highly dependent on the gain, bandwidth and noise figure (NF) of the receiver. A small gain variation in the receiver chain (e.g. due to temperature drift or DC bias point variations) will degrade the receiver sensitivity [15]. A solution to compensate for such gain variations by switching between the antenna port and a reference load ( $50\ \Omega$  resistor) at the receiver input was proposed by R.H. Dicke [16] (see Fig. 1.1).

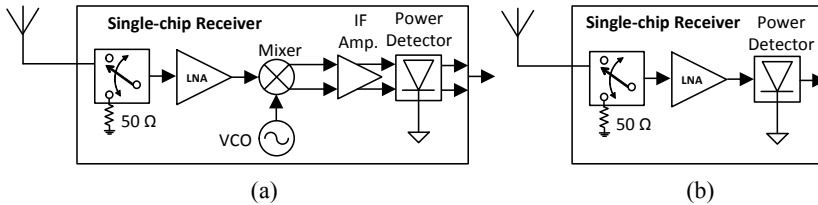


Figure 1.1. Two receiver architectures for possible use within a W-band Dicke switched radiometer front-end: (a) with and (b) without using a frequency down-conversion stage.

At mm-wave, the human body emits 90% of the electromagnetic (EM) energy across the spectrum, nearly as a black body [10]. The thermal radiations are indistinguishable from the Johnson (white) noise generated by the thermal agitation of the charge carriers [16]. Due to this similarity, a Dicke switch that switches between the antenna and a reference load can be used in the radiometer for calibration purposes [16]. Switching with a 50 % duty cycle will, however, degrade the receiver sensitivity by a factor of two. The radiometer sensitivity can be improved by reducing the noise figure and increasing the gain and bandwidth of the receiver as well as reducing the Noise Equivalent Power (NEP) level of the detector (see Chapter 2).

Figure 1.1(a-b) depict two receiver topologies with or without using down-conversion to a lower Intermediate Frequency (IF) that may be used in a Dicke switched radiometer for a passive imaging application at W-band (75-110 GHz), for example. Such imaging receivers have been realised using expensive III-V (e.g. InP) technologies with sensitivity values that are good enough for certain applications [17]–[19]. However, they provide multi-chip solutions. Also, to increase the field of view the antenna array size (number of receivers) will have to be increased and this can result in a high cost [10].

To increase the integration level and reduce the cost some silicon W-band Dicke switched receivers were reported [4], [6], [15]. The noise figure of those receivers is 10 dB or higher. To push the performance of Dicke switched radiometers beyond the current state-of-the-art low-loss RF Micro-Electro-Mechanical Systems (MEMS) switches could be considered (e.g. switches developed by IHP with below 0.5 dB of losses up to 140 GHz) [20]. Some SiGe W-band LNAs reported an NF of 3-4 dB [21], [22]. Thus, SiGe/GaAs MEMS LNAs with an NF of 4-5 dB may be feasible at W-band.

## 1.2 Aim and Contents of the Thesis

The aim of this thesis is to investigate and experimentally validate some novel reconfigurable and wideband circuit designs for mm-wave radiometer front-ends (incl. low-loss switch networks, switched LNAs, broadband IF amplifier and power detectors). Furthermore, the monolithic integration of RF-MEMS based Dicke switch networks with wideband LNAs using SiGe and GaAs foundry processes has been demonstrated for the first time within the 30-110 GHz range.

The remainder of this thesis is divided into ten chapters and is organised as follows.

**Chapter 2** gives a brief introduction to microwave and mm-wave active circuits as well as a short background on switches and RF fundamentals.

**Chapter 3** includes an analysis of key component requirements for a W-band passive imaging application using two receiver architecture solutions.

**Chapter 4 (Paper I)** presents W-band RF-MEMS Dicke switch networks implemented in a GaAs monolithic microwave integrated circuit (MMIC) foundry process.

**Chapter 5 (Paper II)** introduces a novel W-band switched LNA MMIC based on an RF-MEMS Dicke switch network and a wideband LNA design.

**Chapter 6 (Paper III)** covers the design and results of some mm-wave RF-MEMS based switch networks realised in a SiGe BiCMOS technology.

**Chapter 7 (Paper IV)** investigates the monolithic integration of a 30 GHz MEMS Dicke switch network and a wideband LNA in a SiGe process.

**Chapter 8 (Papers V-VI)** presents two novel W-band power detector circuits fabricated in a 0.13  $\mu\text{m}$  SiGe process. These detector designs obtain a higher sensitivity (lower NEP) than earlier reported silicon W-band power detectors and are also competitive with III-V based detectors at W-band. They may be used in system-on-chip (SoC) direct-detection radiometers as an alternative to more costly (multi-chip) receiver modules for mm-wave passive imaging applications, for example.

**Chapter 9 (Papers VII-VIII)** presents two differential SiGe RFICs (high-gain wideband IF amplifier and broadband IF section) which can improve the receiver sensitivity of SoC W-band direct-conversion radiometers.

**Chapter 10** summarises the conclusions of this thesis and also suggests possible future work with respect to the presented research topics.

## 2. Background to RF and Microwave Circuits

This chapter presents a short historical background and brief review on the basic concepts of RF/millimetre-wave and MMIC/RFIC technologies. A basic overview of solid-state and RF-MEMS based switches as well as the fundamental RF performance metrics used in this study are also included.

### 2.1 RF/Millimetre-Wave Technology and Applications

Radio frequency (RF) is the oscillation frequency of electromagnetic (EM) waves in the range of 3 kHz to 300 GHz. A segment of RF bounded by 300 MHz to 300 GHz is defined as microwaves. A sub-segment of microwaves that occurs at 30-300 GHz is termed as mm-wave. One of the earliest applications of mm-wave technology appeared in Radio Astronomy in the 1960's, which was followed by military applications in the 70's [23]. In the 80's, the use of mm-wave for commercial application was initiated due to the availability of MMIC technology for mass production. The first 77 GHz automotive collision avoidance radar came in the 90's. Later on, the development of broadband communication system was considered for the 60 GHz license free band [23]. Since then, mm-waves have been proposed for high data rate transmission, high-resolution radar sensors, and imaging systems for concealed weapon detection and all-weather vision [1], [7].

### 2.2 MMIC and RFIC Technologies

Microwave circuits in which the active and passive components are integrated on a common substrate using solder or conductive epoxy adhesive are known as Microwave Integrated Circuits (MICs) [24]. Multi-chip integration methods are still frequently used at mm-wave frequencies despite high losses due to the off-chip interconnects. With the availability of high resistivity GaAs substrates, MMICs were developed, where all active and passive RF components, and conducting paths are embedded in different metal layers on a single substrate [24]. Later on, when these devices were integrated on a silicon substrate, it came to known as a Radio Frequency Integrated Circuit (RFIC) and sometimes MMIC interchangeably. RFICs are usually known to operate at lower frequencies than MMICs [24].

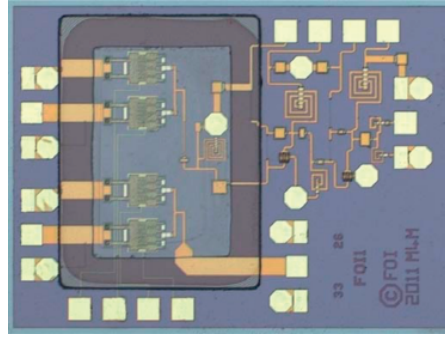


MMICs have been dominated by III-V technologies particularly in their early era. High electron mobility transistors (HEMTs) based on InP are well-known due to their superior high-frequency properties but a high fabrication cost of InP based MMICs makes them less suitable for mass production. GaAs metamorphic HEMT (mHEMT) process technologies have shown performances close to InP devices [25], [26]. Gallium nitride (GaN) HEMT technologies are mostly presented for high power applications below the mm-wave range although some designs exist also above 30 GHz [27], [28]. Silicon technologies have gained attraction due to a lower production cost in large volumes and the possibility of monolithic integration of analog and digital circuits on the same substrate. Both silicon-germanium (SiGe) based heterojunction bipolar transistors (HBTs) and complementary metal-oxide-semiconductor (CMOS) field-effect-transistors (FETs) have been used in mm-wave circuits and systems [15], [29]. The RF performance of advanced SiGe BiCMOS processes is approaching that of III-V technologies [21], [22]. Nowadays, SiGe processes with maximum oscillation frequencies ( $f_{\max}$ ) of 500 GHz are commercially available [30]. Thus, such silicon technologies could be appropriate candidates for low-cost mm-wave system-on-chip solutions. In this thesis novel MMIC/RFIC designs will be investigated.

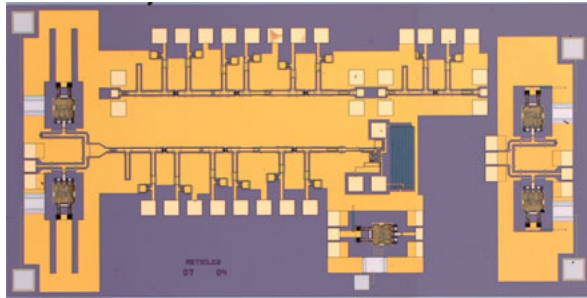
### *2.2.1 MMIC Technology*

Traditionally, GaAs based processes have been used to manufacture MMICs. GaAs has a high electron mobility and saturation velocity which results in a short transit time and high operating frequencies for the transistors ( $f_T$ ,  $f_{\max}$ ). Due to its wide band gap, GaAs can handle a relatively high output power. GaAs processes include high-performance active RF devices and low-loss passive components such as resistors, capacitors, inductors, and varactors. Transmission lines, bends, tee junctions, and air bridges are also available.

The high resistivity GaAs substrate results in relatively low losses for such on-chip interconnects which can be optimised by the designer using EM simulation tools. Figures 2.1(a-b) show the chip photographs of two different MMIC designs made in OMMIC's 0.13  $\mu\text{m}$  pHEMT and 70 nm mHEMT GaAs processes, respectively. The first one consists of some K-band (18-26 GHz) RF-MEMS Dicke switch and switched LNA micro-strip circuits made on 100  $\mu\text{m}$  thick GaAs wafers [31]. The use of via holes enables short connection paths to a well-defined (metallised) back-side ground plane. The second example contains W-band coplanar waveguide (CPW) based designs of RF-MEMS Dicke switch, LNA and power detector circuits designed within the FP7 Project NANOTEC [32]. Quarter wavelength ( $\lambda/4$ ) transmission lines are used here as RF chokes. In a CPW design the signal and ground planes are both on the front side of the wafer which typically results in a larger circuit area. The line impedance and phase velocity are on the other hand less dependent on the substrate height.



(a)



(b)

Figure 2.1. K-band RF-MEMS Dicke switch and switched LNA micro-strip MMICs [31] (a), and W-band MEMS Dicke switch, LNA and power detector CPW based MMICs (b). The chip areas are equal to  $2 \times 1.5 \text{ mm}^2$  and  $3.9 \times 1.9 \text{ mm}^2$ , respectively. Micrographs with courtesy of Andreas Gustafsson, and Carl Samuelsson, Swedish Defence Research Agency (FOI).

### 2.2.2 RFIC Technology

Figure 2.2 shows an initial design of a single-chip 94 GHz RF-MEMS switched antenna front-end with breakout circuits that was fabricated in a  $0.25 \mu\text{m}$  SiGe BiCMOS process from the foundry IHP. This W-band RFIC receiver was co-designed by Uppsala University, ULM University and FOI within the FP7 project NANOTEC [33]. This technology offers both SiGe based HBTs and CMOS based FETs as well as poly-silicon based resistors, MIM capacitors, inductors and varactors. In terms of active device performance at mm-wave frequencies the most advanced SiGe BiCMOS processes are moving closer to that of III-V technologies. SiGe processes offer 5-10 metal layers including thick top metal layers for designing low-loss passive components [20], [34]. Since the quality factors of the on-chip transmission lines and inductors are fairly low due to a low resistive silicon substrate, the use of on-chip passives should be minimised (e.g. an active balun may provide a better solution than a passive one). The layout design in silicon is not as straight-forward as with GaAs MMICs (e.g. circuit designers may choose to implement a well-defined ground plane using bottom metal layers) and individual metal density requirements must be fulfilled.

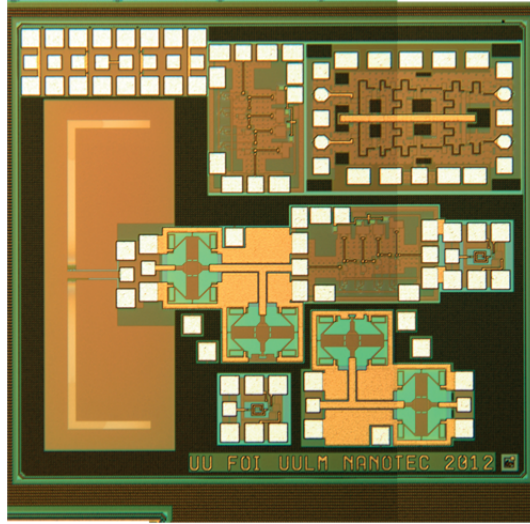


Figure 2.2. RFIC designs made in a 0.25  $\mu\text{m}$  SiGe technology for a 94 GHz receiver: on-chip antenna, MEMS Dicke switch, LNAs and power detector (the chip area is 5 mm<sup>2</sup>). RFIC photograph with courtesy of IHP, ULM University, Swedish Defence Research Agency (FOI), and Uppsala University.

## 2.3 RF Switches

A switch is defined as a device that makes or breaks the connection for the signal flow. Switches that operate in the radio frequency (RF) band are known as RF switches. RF switches are characterised in terms of their transmission/return losses, isolation, frequency coverage (bandwidth), linearity, switching time/reliability, and DC power consumption.

### 2.3.1 Diode and Transistor based RF Switches

Solid-state switches can be divided into diode and transistor based switches. Attractive features of P-type-Intrinsic-N-type (PIN) diode based switches are high power handling and fast switching speed. However, they consume relatively high levels of DC power, have complex biasing schemes and typically provide discrete component solutions [35]. The low frequency operation of the PIN diodes is limited by the DC current in the RF channel that is required to bias the diodes [35]. Transistor based switches offer an integrated solution, minimal DC power consumption, and switching time in the order of nanoseconds [35]. However, diode and transistor based RF switches can be rather narrow-band, non-linear, and have relatively high losses, particularly in the microwave and mm-wave frequency ranges.

### 2.3.2 RF-MEMS Switches

MEMS switches utilise miniaturised mechanical contacts to make or break the RF connections by applying an electrostatic force [35]. Such contacts are made between fixed and movable parts. The mechanical design provides good advantages over its electrical counterparts such as lower insertion loss, DC power consumption, wider bandwidth, higher isolation and linearity [36], [37]. Moreover, it offers a smaller form factor as compared to the traditional EM switches [38]. RF-MEMS switches have also been proposed in the designs of tunable phase shifters, tunable filters, tunable impedance matching networks, and reconfigurable antennas [39]–[47]. Nowadays, RF-MEMS switches have gained attraction also due to the possibility of monolithic integration with active circuits in the microwave and mm-wave ranges as some foundries have developed such switches in GaAs and SiGe BiCMOS process technologies [31], [48]–[50]. RF-MEMS switches can be classified on the basis of their actuation mechanism, contact type and design configuration [51] as follows.

- RF-MEMS switches may rely on electrostatic actuation due to its simplicity, switching speed and low power consumption [51] (other possible actuation mechanisms are e.g. piezoelectric, electro-thermal and electro-magnetic actuation).
- The contacts between the movable and fixed parts of the RF-MEMS switches can be a metal-to-metal (ohmic) contact or a capacitive contact with a dielectric between the two parts. The ohmic contact switches can work from DC to the mm-wave range. However, the RF-performance is restricted due to the contact resistance that becomes more pronounced at higher frequencies. The capacitive switches perform better at higher frequencies but are instead limited at lower frequencies due the requirement for a high capacitance value to provide a short circuit [20], [52], [53].
- RF-MEMS switches could be placed in series/shunt configuration with reference to the transmission line according to the design requirements.

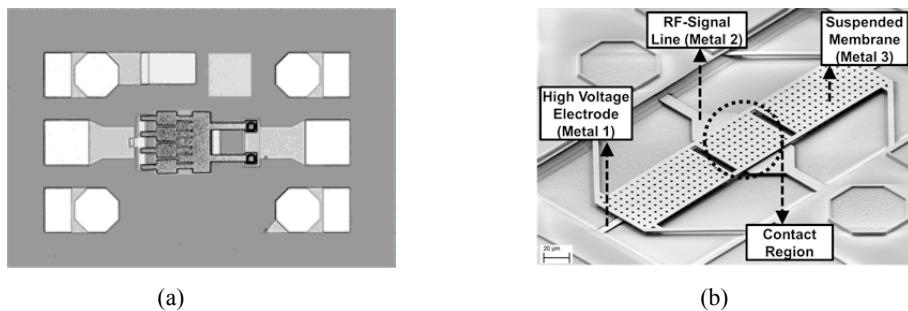


Figure 2.3. Micrographs of an ohmic contact series RF-MEMS switch (a) and a capacitive shunt RF-MEMS switch (b) fabricated in GaAs and SiGe BiCMOS processes, respectively. Micrographs with courtesy of OMMIC S.A.S., IHP GmbH, and Wiley Publisher, respectively.

RF-MEMS switches have quite unique properties, but there are also some limitations and challenges associated with them. Typically, such switches require a higher actuation voltage; longer switching time and they may also have a lower power handling as compared to their electrical counterparts. Long-term reliability issues are the primary concerns for applications that require repeated switching. RF-MEMS switches are mechanically sensitive devices which need to be protected (packaged) and this can increase the over-all cost. These issues are being addressed by RF-MEMS researchers and foundries [54], [55]. Despite of these challenges, RF-MEMS switches have been proposed as an enabling technology for adaptive front-end architecture solutions (e.g. MEMS switches used in handsets and radar sensors) [56], [57]. Commercially available MEMS switches are from vendors such as RadantMEMS and WiSpry among others [56], [57].

Figures 2.3(a) and (b) show micrographs of ohmic contact (series) and capacitive (shunt) MEMS switches, respectively. The ohmic contact MEMS switch shown here was developed in a GaAs MMIC process technology from the foundry OMMIC (it results in transmission losses of some tenths of a dB with 20-40 dB of isolation from DC up to the mm-wave range [52]). The on and off switching times are in the order of 1-10  $\mu$ s [52]. Benzo-Cyclo-Butene (BCB) protective caps with a marginal effect on the packaged switch performance have been reported in [58], [59]. The capacitive MEMS switch shown in Fig. 2.3(b) was developed in a SiGe BiCMOS process technology from the foundry IHP. Such switches have shown less than 0.25 dB of insertion loss and better than 20 dB of isolation at 30-100 GHz [53]. The on and off switching times are around 10  $\mu$ s [20]. The long-term switching reliability was demonstrated in life cycle tests showing up to 5-10 billion switch cycles [60]. A glass cap with a silicon frame was used to package the SiGe MEMS switches [53]. Series and shunt MEMS switches have been used in this research work for the design of mm-wave switch networks.

## 2.4 Low Noise Amplifiers and Performance Parameters

High-performance receivers are needed in RF systems for wireless communication, space, defense and security applications within the microwave and mm-wave range. The low noise amplifier (LNA) is an essential functional block in these receivers. The primary target of the LNA is to amplify the input signal without adding too much noise. The key performance parameters are bandwidth, gain, noise figure, linearity, and power consumption that need to be optimised by the circuit designer. The most essential small-signal and large-signal parameters for active and passive RF components are defined as follows.

**Scattering (S) parameters** are commonly used at RF and microwave frequencies for transmission lines, components modelling, specifications, and circuit designs. The relation based on the s-parameters of a two-port network as shown in Fig. 2.4, using matrix notation can be written as [61],

$$\begin{bmatrix} b_1 \\ b_2 \end{bmatrix} = \begin{bmatrix} s_{11} & s_{12} \\ s_{21} & s_{22} \end{bmatrix} \begin{bmatrix} a_1 \\ a_2 \end{bmatrix} \quad (2.1)$$

Where  $[s]$  is known as the scattering matrix.

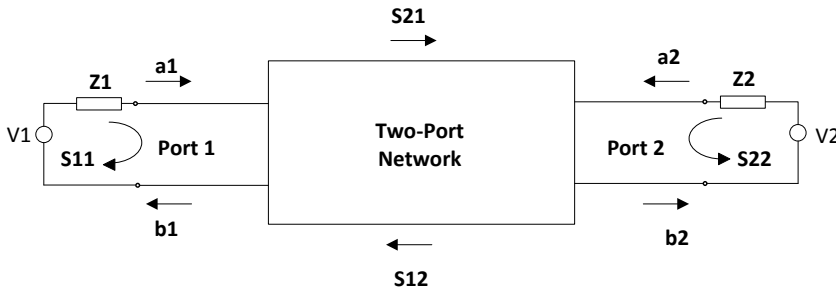


Figure 2.4. Two-port network and its s-parameters.

Where  $a_1$ ,  $a_2$  and  $b_1$ ,  $b_2$  are the incident and reflected waves voltages, respectively. The s-parameters are defined as follows:

$$s_{11} = \left. \frac{b_1}{a_1} \right|_{a_2=0} = \Gamma_1 = \text{reflection coefficient at port 1 with } a_2=0$$

$$s_{21} = \left. \frac{b_2}{a_1} \right|_{a_2=0} = T_{21} = \text{transmission coefficient from port 1 to 2 with } a_2=0$$

$$s_{22} = \left. \frac{b_2}{a_2} \right|_{a_1=0} = \Gamma_2 = \text{reflection coefficient at port 2 with } a_1=0$$

$$s_{12} = \left. \frac{b_1}{a_2} \right|_{a_1=0} = T_{12} = \text{transmission coefficient from port 2 to 1 with } a_1=0$$

By assuming  $a_1$  or  $a_2 = 0$ , port1/port2 should be perfectly matched to the  $Z1/Z2$  loads (i.e. no reflections occurring due to impedance mismatching). For maximum power transfer from the sources ( $V1/V2$ ) to the loads (port 1/port 2), the reflections ( $s_{11}$  and  $s_{22}$ ) are then needed to be minimised by impedance matching. For active circuits, the forward transmission coefficient ( $s_{21}$ ) should be high enough to provide the required gain and the reverse transmission coefficient ( $s_{12}$ ) should be minimised to avoid unwanted feedback (oscillations). Passive symmetrical (reciprocal) circuits have  $s_{12}=s_{21}$  and the losses should be kept as low as possible ( $|s_{21}|$  will be less than 1).

**Noise figure (NF)** is a figure of merit that indicates the signal deterioration due to noise added by devices while passing through a circuit or chain of circuits. It is the ratio of the signal-to-noise ratio (SNR) at the input to the signal-to-noise ratio at the output and it is often expressed in decibel [62]. The noise figure indicates the quality of the receiver and it is also a limiting factor for the receiver sensitivity. NF is related to the noise temperature as:

$$T = 290 * (10^{NF/10} - 1) \quad (2.2)$$

Where 290 K stands for the reference temperature.

The noise figure of a cascaded system (or a receiver) can be calculated from the individual noise factors (F); (see Eq. 2.3) using the well-known Friis equation (see Eq. 2.4) which indicates that the overall noise figure is dominated by the noise from the initial stages. Furthermore, increasing the gain of the initial stages helps in minimising the overall noise figure [62].

$$F_i = 10^{NF/10} \quad (2.3)$$

$$F_{total} = F_1 + \frac{F_2 - 1}{G_1} + \frac{F_3 - 1}{G_1 G_2} + \dots + \frac{F_n - 1}{G_1 G_2 \dots G_{n-1}} \quad (2.4)$$

Where  $F_i$  and  $G_i$  are the noise factor and available power gain of the  $i^{th}$  stage and  $n$  denotes the number of stages used in a receiver chain, for example.

**Linearity** is defined as the power range in which a circuit or particularly the amplifier output power remains strictly proportional to its input power. However, active components suffer from non-linearity with the rise in the input power level. At this point, the large signal performance of the tested device needs to be considered. Two important parameters that tell about the circuit linearity at high input power levels are the compression point and the third order intercept point (see Figs. 2.5 and 2.6).

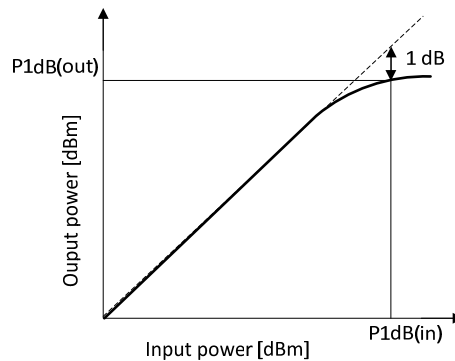


Figure 2.5. Illustration of the 1-dB compression point (P1dB).

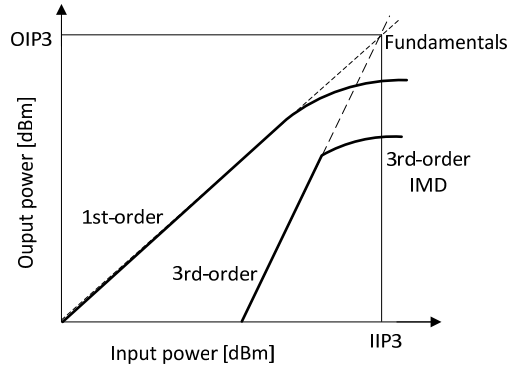
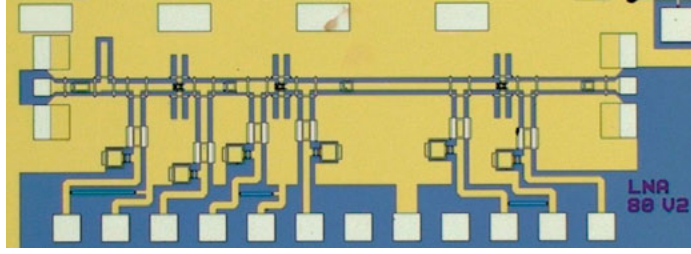


Figure 2.6. Illustration of the third order intercept point (IP<sub>3</sub>).

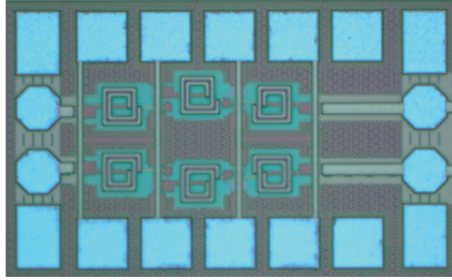
The first one is usually defined as 1-dB compression point (P1dB). That is, the input power level at which the output power of the device is 1 dB below its linear characteristics (see Fig. 2.5). The other parameter is defined by intermodulation distortions (IMDs) that occur when more than one signal is present at the input of a nonlinear device simultaneously. Consequently, the output signal will be composed of many spectral components at different combinations of their fundamental frequencies. Although, the power levels of the intermodulation terms are much smaller as compared to their origins they can even corrupt the desired signal. The most critical IMDs are usually evoked by the third order non-linearity of a device (e.g. LNA or a receiver). This effect is captured by the third order intercept point (IP<sub>3</sub>) as shown in Fig. 2.6. IP<sub>3</sub> is expressed in dBm and it refers to the linear (non-saturated) input/output power levels for which the third order IMDs would reach the level of the fundamental components (originators). In fact, these two power levels can only hypothetically be equal. Another specification related to P1dB is the dynamic range (DR) which is defined as the ratio of the maximum input power (P1dB) to the minimum input power that can be distinguishable from thermal noise floor.

Figure 2.7(a) shows a micrograph of a W-band LNA fabricated in a 70 nm mHEMT GaAs technology from OMMIC. This LNA made within the FP7 project NANOTEC is based on an earlier amplifier design [63], [64]. Three transistor stages are used in this LNA design together with capacitors and CPW lines working as a stub and RF chokes (the chip area is 1.22 mm<sup>2</sup>). Figure 2.7(b) shows a micrograph of a two-stage differential IF amplifier operating within the 1-40 GHz range (see **Paper VII**) [65]. The design was made in a 130 nm SiGe BiCMOS process (with 300/500 GHz  $f_T/f_{max}$ ) from the foundry IHP. The total chip area is 0.27 mm<sup>2</sup> including six on-chip inductors for input, output, and inter-stage matching. Compared with the coplanar GaAs three-stage LNA, the two-stage SiGe IF amplifier occupies a five times smaller area even though it operates at a much lower frequency.





(a)



(b)

Figure 2.7. Micrograph of a three-stage W-band LNA circuit (chip area is  $1780 \times 685 \mu\text{m}^2$ ) fabricated in a 70 nm GaAs mHEMT process. Micrograph with courtesy of OMMIC S.A.S. (a) and micrograph of a two-stage wideband IF amplifier ( $678 \times 405 \mu\text{m}^2$ ) fabricated in a 130 nm SiGe BiCMOS process technology (see **Paper VII**) [65] (b).

## 2.5 Power Detectors

A Power detector is a device that converts the RF input power to a constant output voltage which can be sampled by an A/D-converter. The detector output voltage is proportional to the square of the input voltage [15] when it operates in the square-law region. In order to minimise the noise generated by the detector, it operates with a low bias voltage just above the conduction point.

A key figure-of-merit for a power detector is the responsivity that measures the change in detector output voltage per unit input power represented by the term  $\beta$  [15].

$$\beta = \frac{V_{out}}{P_{in}} \quad (2.5)$$

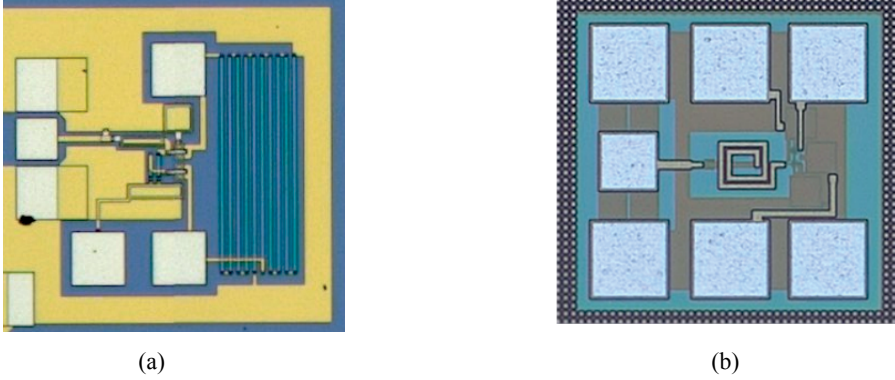


Figure 2.8. Micrographs of W-band power detectors fabricated in a 70 nm GaAs mHEMT process (a) and in a 0.25  $\mu\text{m}$  SiGe BiCMOS process [66] (b), respectively (the chip areas are both equal to 0.1  $\text{mm}^2$ ). Micrographs with courtesy of Carl Samuelsson, Swedish Defence Research Agency (FOI).

Another related term is the Noise Equivalent Power (NEP) level which measures the sensitivity of the detector. It is defined as the minimum input power that gives the unity signal-to-noise ratio at the output of the detector in a one hertz bandwidth. The NEP value is expressed in  $\text{W}/\text{Hz}^{1/2}$  as it is equal to the detector output noise voltage spectral density ( $v_n$ ) normalised with  $\sqrt{\Delta f} = 1 \text{ } \sqrt{\text{Hz}}$  divided by the responsivity [67].

$$NEP = \frac{v_n / \sqrt{\Delta f}}{\beta} \quad (2.6)$$

Figures 2.8(a) and (b) show two W-band power detector circuit designs made in OMMIC's 70 nm GaAs mHEMT and IHP's 0.25  $\mu\text{m}$  SiGe process technologies, respectively. The designs were made within the FP7 project NANOTEC [32]. The circuit areas of both designs are comparable to each other (0.1  $\text{mm}^2$ ). A high-value load resistor used in the GaAs detector circuit occupies roughly half of the total circuit area whereas such a high-value resistor consumes much less area in the SiGe detector design. For maximum power transfer to the detector input, an input matching network is required. A distributed matching network is used in the GaAs detector design which enables a broadband frequency response whereas a more narrow-band matching network (using a capacitor and an inductor) is employed in the SiGe detector design. Full custom design of such high quality on-chip inductors was possible due to the thick top metal layer available in this SiGe BiCMOS process.

### 3. Receiver Architectures and Requirements for a W-Band Passive Imaging System

This chapter gives an overview of different receiver architecture solutions and component requirements for a targeted W-band passive imaging system. For this purpose, some GaAs and SiGe RF-MEMS switch networks, switched LNAs, wideband IF amplifier and power detector IC designs were simulated and characterised (see Chapters 4-9). The NETD calculations were made by Tomas Boman, Swedish Defence Research Agency (FOI).

#### 3.1 Architectures and Requirements

A W-band passive imager works at stand-off distances (2-20 m) to detect objects hidden under clothing for security screening purposes (concealed weapons and explosives detection). Such a radiometric system is described by its thermal resolution or Noise Equivalent Temperature Difference (NETD) which is given by [4], [6], [15]:

$$NETD = T_S \sqrt{\frac{1}{BW \cdot \tau} + \left(\frac{\Delta G}{G}\right)^2 + \frac{1}{2\tau} \cdot \left(\frac{NEP}{k_B \cdot G \cdot BW \cdot T_S}\right)^2} \quad (3.1)$$

where  $T_S$  is the receiver noise temperature (proportional to the noise figure),  $BW$  is the bandwidth,  $\tau$  specifies the system integration time,  $G$  is the pre-detection gain,  $\Delta G/G$  is the gain variation,  $k_B$  is the Boltzmann constant and  $NEP$  is the noise-equivalent-power of the detector. By using a Dicke switch and a demodulator (synchronised with the switch) in the radiometer chain the receiver gain variations over time can be cancelled. In practice, however, some gain variations will always exist (i.e.  $\Delta G/G > 0$  between calibrations) due to the effects of temperature drift or DC bias point variations in the receiver components used. Within the targeted W-band passive imaging system a Dicke switch will be used for making a calibration of the receiver for the time it takes to capture an image (which in this case is equal to 62.5 ms) rather than performing a calibration after every pixel ( $\tau=0.3$  ms).

Between two calibrations, we may consider this as a total power radiometer front-end since the switch will not be activated during this time period (the receiver will then be measuring the noise temperature with respect to the antenna and only towards the 50  $\Omega$  reference load during calibration).

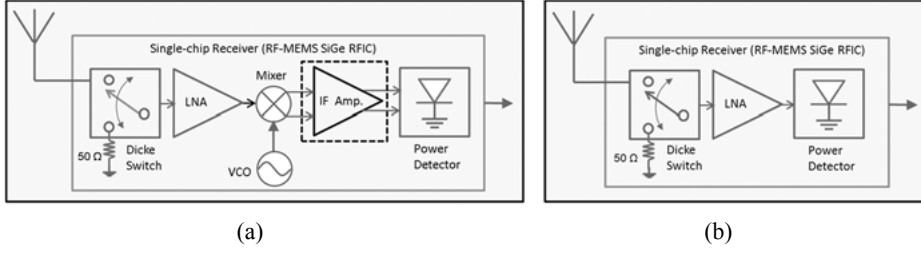


Figure 3.1. Two receiver architectures for possible use within a W-band Dicke switched (GaAs or SiGe) single-chip radiometer front-end: with (a), and without using a frequency down-converter (b).

From the above considerations, we may then use (Eq. 3.1) to arrive at the target receiver (amplifier) gain and NF values for a given set of system parameters. This will also depend on how large the receiver gain variations are during the time between two calibrations (62.5 ms). During such a relatively short time interval, thermal variations in the receiver components due to some temperature drift is expected to be small (0.001 dB or less) since the ambient temperature should be quite stable when the radiometer system is being used (typical amplifier gain variations are in the order of 0.01-0.02 dB/K [68] and simulations of an amplifier made in IHP's SG13G2 technology also confirm such temperature sensitivities). Assuming that protective measures are taken to prevent against the effects of unwanted Electro-Magnetic Interference (EMI), remaining gain variations may be due to some inevitable thermal/DC bias point variations in the receiver components used.

To assess the RF properties of a Dicke switched radiometer front-end for the studied W-band passive imaging application a possible use of the two receiver topologies shown in Fig. 3.1 will be considered (i.e. with or without using down-conversion from W-band to a lower Intermediate Frequency IF). We will use as an example here certain assumed target values for the key receiver components if realised in a 0.13  $\mu\text{m}$  SiGe BiCMOS technology from IHP (SG13G2). In a same way it would also be possible to make such an analysis based on the corresponding target values for W-band receiver components if made using a GaAs or InP based semiconductor technology.

A final goal of this study is to be able to achieve an NETD in a W-band receiver chain which may be considered low enough for the application-in-mind (e.g.  $\leq 0.3$  K) and that may be realised in the above mentioned SiGe technology. Below, some target values for the main functional blocks will be presented to fulfill the receiver requirements of a W-band passive imaging (radiometric) system. Figure 3.2 shows the calculated required receiver (Rx) gain as function of the detector NEP when the Rx noise figure is equal to 5.0-5.3 dB (NETD=0.3 K,  $\tau=0.3$  ms,  $\Delta G/G=0.001$  dB and BW=25 GHz).

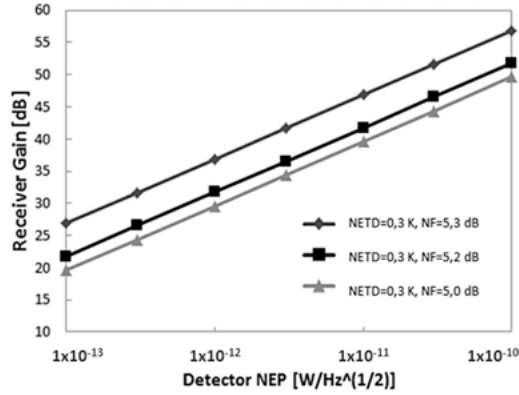


Figure 3.2. Calculated required receiver gain versus the detector NEP when the receiver NF=5.0-5.3 dB (NETD=0.3 K,  $\Delta\tau=0.3$  ms,  $\Delta G/G=0.001$  dB, BW=25 GHz). The graph is with courtesy of Tomas Boman, Swedish Defence Research Agency (FOI).

### 3.1.1 Direct-Detection Receivers (*W*-band power detector)

We will consider first a use of direct detection at *W*-band as depicted in Fig. 3.1(b). The main challenges with this receiver topology are that the Rx (LNA) noise figure needs to be as low as possible (to achieve a low NETD) and on the same time the Rx (LNA) gain should also be quite high unless the detector will have a sufficiently low NEP. With a receiver NF close to 5 dB (e.g. if we assume 1 dB of loss for a SiGe RF-MEMS based SPDT switch network and  $NF_{LNA}=3-4$  dB [20]–[22] and given that 20-30 dB is the highest stable receiver (LNA) gain in the specified frequency bandwidth then the detector should have a NEP in the range of 0.1-1 pW/Hz<sup>1/2</sup> (see Fig. 3.2).

Thus, in order to fulfill the low-noise receiver requirements set by the *W*-band passive imaging application under consideration here, a *wideband* power detector circuit with a high sensitivity should be used after the LNA when the direct-detection receiver architecture is being used (Fig. 3.1(b)). Two novel SiGe *W*-band power detector designs made in a 0.13  $\mu$ m BiC-MOS process are summarised in Chapter 8 (**Papers V-VI**). To the author's best knowledge, the latter one of those SiGe detector designs reports the widest  $|S_{11}|$  -10 dB bandwidth ( $|S_{11}|\leq -10$  dB at 79-102 GHz) among silicon based *W*-band power detectors and it is competitive with some InP based *W*-band detectors in terms of a higher responsivity and similar NEP [18], [19].

### 3.1.2 Direct-Conversion Receivers (IF amplifier and detector)

A main benefit of using the heterodyne architecture (see Fig. 3.1(a)) is that a higher receiver gain and sensitivity more easily could be obtained if a high-gain *wideband* IF amplifier is used after the mixer and the LNA/detector gain/sensitivity requirements could then be relaxed. It will be easier in this way to achieve a higher Rx gain and a less sensitive detector may suffice since amplification can be added after the mixer. As shown in Fig. 3.2, an Rx gain of 40-45 dB would be required if we assume a receiver noise figure of 5 dB and a detector NEP close to  $10 \text{ pW/Hz}^{1/2}$ .

Table 3.1. Target values of a W-band heterodyne receiver (NETD=0.3 K,  $\tau=0.3 \text{ ms}$ ,  $\Delta G/G=0.001 \text{ dB}$ , BW=25 GHz).

Device	Switch	LNA	Mixer	IF amplifier	Detector	Receiver
Gain (dB)	-1	20	5	15-20	N/A	40-45
NF (dB)	1	4	8	5-10	NEP=10 $\text{pW/Hz}^{1/2}$	5

A smaller receiver area would be possible without using down-conversion but the requirements of a wideband LNA and a detector at W-band will be more stringent to be able to reach the same NETD value. In the heterodyne receiver architecture a mixer is used to down-convert from W-band to a lower IF (e.g. at 3-28 GHz as we are targeting a 25 GHz bandwidth). Based on the specified receiver parameters an IF amplifier gain of 15-20 dB will be required to reach an NETD of 0.3 K (see Fig. 3.2 and Table 3.1). Owing to the LNA/mixer gain the IF amplifier noise figure will have less influence on the receiver sensitivity and using the well-known Friis formula (Eq. 2.4) the target NF values are 5-10 dB depending on the IF amplifier gain.

A SiGe BiCMOS differential wideband IF amplifier with a gain of 15-20 dB at 3-26 GHz and a combined single-chip IF section (consisting of this IF amplifier followed by a 5-40 GHz power detector) are presented in Chapter 9 (**Papers VII-VIII**). The broadband properties, high sensitivity and wide-band matching over a significantly wider bandwidth than recently reported IF amp/detector RFICs [29], [69] make the proposed circuits (IF amplifier and IF section) viable candidates for SoC W-band direct-conversion radiometer receivers with improved sensitivity figure-of-merits.

### *3.1.3 Millimetre-Wave Dicke Switch and Switched LNA*

In a radiometric system where the sensitivity (thermal resolution) is largely influenced by the receiver (LNA) noise figure, gain and bandwidth a high performance (low-loss, high isolation) Dicke switch network can be used for calibration purposes and to compensate for receiver gain variations [15]. Chapter 4 (**Paper I**) presents a GaAs MMIC RF-MEMS based Dicke switch network with a minimum loss of 1 dB and more than 20 dB of isolation at W-band. A W-band MEMS switched LNA GaAs MMIC with 16 dB gain (11 dB isolation) and minimum noise figure of 5 dB is covered in Chapter 5 (**Paper II**). Chapter 6 (**Paper III**) presents results of more than 300 tested SiGe RF-MEMS switch networks at 40-80 GHz and the results of a 30 GHz SiGe MEMS Dicke switched LNA are summarised in Chapter 7 (**Paper IV**).

## 4. W-Band RF-MEMS Switch Networks in a 0.13 $\mu\text{m}$ GaAs pHEMT Process Technology

This chapter presents two W-band RF-MEMS based Dicke switch networks designed in a 0.13  $\mu\text{m}$  GaAs pHEMT technology from the foundry OMMIC. One of the Dicke switch designs which was selected and fabricated using this GaAs MMIC process to validate its wideband RF properties includes also a BCB cap type of zero-level package. To the author's best knowledge, these are the first reported packaged/unpackaged RF-MEMS Dicke switch networks in a GaAs MMIC process technology at W-band. The best one among those MEMS Dicke switch networks has 1.1-1.6 dB of on-wafer measured transmission losses at 70-96 GHz with up to 19 dB of in-band isolation. The package-added losses were 0.1-0.5 dB at 70-95 GHz (<1 dB in the entire W-band). Such GaAs RF-MEMS Dicke switch networks could be used in single-chip mm-wave radiometer front-end MMICs for calibration purposes and compensation of receiver gain variations [4], [6], [15].

The EM simulations and optimisation of the W-band GaAs MEMS switch circuits were made by the author of this thesis. The layouts were done by co-author Carl Samuelsson. Further details are included in **Papers I-II**.

### 4.1 Motivation and Background

Low-loss, high isolation, highly linear and low DC power consumption RF switches and switching networks are necessary in wireless applications such as for example, telecommunications, space, automotive, defense and in RF sensing systems [51],[70]. Nowadays, solid-state based switches are often used in such systems. However, they can be rather narrow-band, non-linear and have relatively high losses, especially in the microwave and mm-wave ranges and diode based switched also consume DC power. RF-MEMS switches are attractive candidates for replacing them in switching circuits and in adaptive front-end architecture solutions due to their superior RF properties (e.g. MEMS switches used in handsets and radar sensors [56], [57]). The ohmic contact type of RF-MEMS switch utilised in this study was developed and fabricated by the GaAs MMIC foundry OMMIC. Such GaAs RF-MEMS switches could enable monolithically integrated (single-chip) high performance reconfigurable LNAs and front-end MMICs for a wide range of applications up to around 100 GHz.



## 4.2 GaAs RF-MEMS Switch Designs and Results

### 4.2.1 RF-MEMS SPST Switch Network

The RF-MEMS switches used here are of the ohmic contact (metal-metal) cantilever type and fabricated in OMMIC's 0.13  $\mu\text{m}$  GaAs pHEMT process (D01PH). The switch is closed when the cantilever is in down-state position (ON) and as a result a low contact resistance ( $R_{\text{ON}}$ ) is realised in the RF path (it provides a small series capacitance value  $C_{\text{OFF}} \approx 10$  fF in the up-state). The cantilever contains several so called flex slots to ensure a good contact is made between the four switch beams and the contact bumps beneath the switch when it is pulled down (the actuation voltage is typically 50-70 V). The DC power consumption is very low since only a small leakage current will flow ( $<10$   $\mu\text{A}$ ). The on and off switching times are close to 1-10  $\mu\text{s}$  [52]. Recent studies have focused on development of packaging solutions using Benzo-Cyclo-Butene (BCB) type of protective caps with marginal effect on the packaged switch performance up to the mm-wave range and to improve the reliability of MEMS switches fabricated in III-V processes [58], [59]. Figures 4.1(a-b) show two chip micrographs of such unpackaged and wafer-level packaged (BCB capped) SPST switch networks made on 100  $\mu\text{m}$  thick GaAs wafers. Series and shunt switches were made as micro-strip designs.

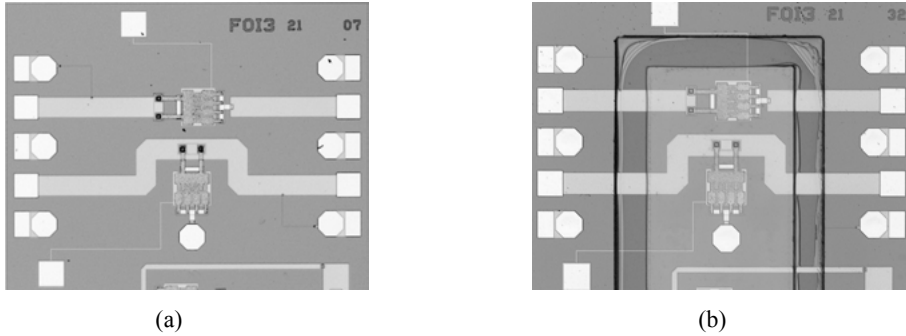


Figure 4.1. Micrographs of RF-MEMS SPST switch circuits made on 100  $\mu\text{m}$  thick GaAs wafers without a BCB cap (a) and wafer-level packaged (BCB capped) (b), respectively.

The SPST series switch network was simulated using a three dimensional MEMS switch model and the EM simulation tool Sonnet (the simulations were made in the same circuit environment as shown in Fig. 4.1(a)). The s-parameters were measured using a 2-port network analyser connected to a probe-station and on-wafer calibration standards. Figure 4.2 shows simulated and measured  $|S_{21}|$  of both packaged and unpackaged MEMS series switches. The uncapped and BCB capped MEMS series switches have close to 1 dB (down-state) and 7-8 dB (up-state) of transmission losses at 75-94 GHz, respectively. The package added losses are equal to 0.5 dB or less at those frequencies. The resonance occurring at 96 GHz is due to the proximity of

the nearby MEMS shunt switch circuit which is located close to the MEMS series switch network (see Fig. 4.1). The GaAs micro-strip MEMS switches show similar RF properties as some earlier co-planar MEMS switches made in the same process with transmission losses below 1 dB and more than 8 dB of isolation from 10 MHz up to 95 GHz, respectively [52].

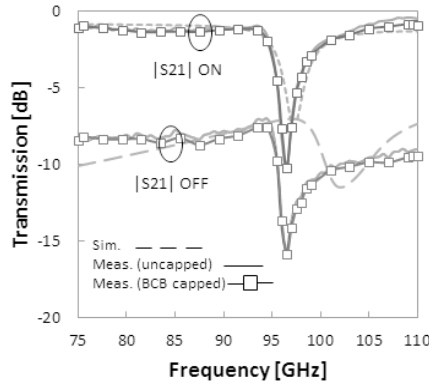
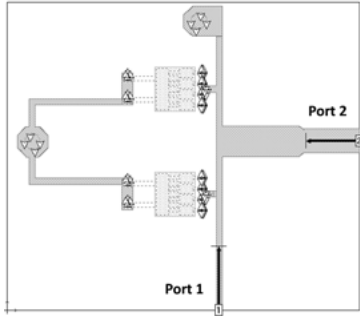


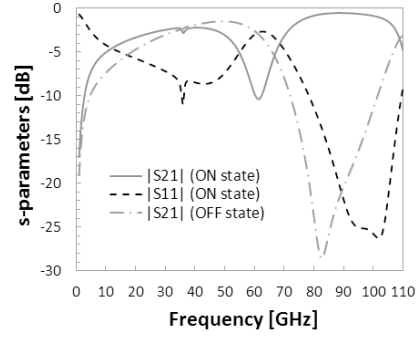
Figure 4.2. Measured and simulated transmission of GaAs RF-MEMS series switch networks.

#### 4.2.2 W-Band RF-MEMS Dicke Switch Networks

Figure 4.3(a) shows a W-band RF-MEMS Dicke switch network design made in the D01PH process. It consists of a micro-strip SPDT switch network with one input/output port (port 1 and port 2) and where the third port has been terminated to ground (via hole) using a 50 ohm on-chip resistor. Two series MEMS switches connected in a shunt configuration at a quarter wavelength distance to the tee junction set the resonance frequency of the Dicke switch along with the connecting transmission lines to ground. In the transmission (ON) state the lower MEMS switch will be in the up-state while the upper one is in the down-state thus resulting in a low impedance in the transmission branch (from port 1 to port 2) and a high impedance in the other branch, and vice versa for the isolation (OFF) state. The RF-MEMS Dicke switch network (complete structure) was simulated and optimised in Sonnet using a foundry-provided (3D) EM MEMS switch model. Figure 4.3(b) shows that the simulated ON state transmission loss is below 1 dB with better than 15 dB of isolation (OFF) at 76-96 GHz, respectively (whereas  $|s_{11}| \leq -10$  dB at 79-109 GHz in the ON state). Due to a limitation with the RF probe station used for W-band measurements (which restricted the possibilities of using a 90° angle connection between the RF ports), a modified Dicke switch design with opposite RF ports was selected for the experimental validation (see Fig. 4.4). Longer transmission lines were used in this case to allow the RF and DC pads to be placed outside the BCB cap that surrounds the RF-MEMS switches. The circuit area is 1285 x 780  $\mu\text{m}^2$ .

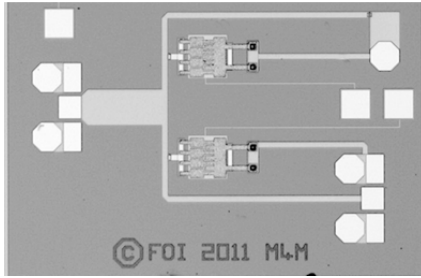


(a)

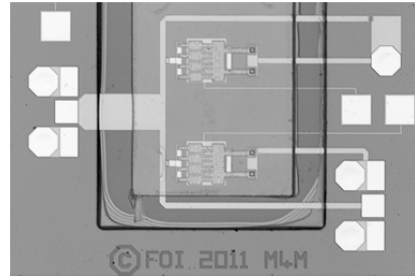


(b)

Figure 4.3. A W-band GaAs MMIC based Dicke switch network (micro-strip design): EM circuit model simulated in Sonnet (a), and simulated s-parameter data (b).



(a)



(b)

Figure 4.4. Micrographs of W-band RF-MEMS Dicke switch circuits made on 100  $\mu\text{m}$  thick GaAs wafers without a BCB cap (a) and wafer-level packaged (b), respectively.

The s-parameters of the fabricated W-band GaAs RF-MEMS Dicke switch networks were measured using a 2-port network analyser connected to a probe station. Some of the MEMS Dicke switches (without a BCB cap) were tested on-wafer at 70-110 GHz using calibration standards included on the same wafer. The diced uncapped and 0-level packaged GaAs MEMS Dicke switch circuits were measured on-chip at 2-110 GHz using a standard calibration substrate and the effects of the RF pads were removed by using an open-short de-embedding technique. Figures 4.5(a-c) show measured and simulated  $|s_{21}|$  (ON/OFF) and  $|s_{11}|$  (ON) of some on-wafer (uncapped) and on-chip (uncapped/BCB capped) tested RF-MEMS Dicke switch networks.

The fabricated Dicke switches have higher transmission and return losses as compared to the more compact Dicke switch design shown in Fig. 4.3(a-b). These somewhat inferior switch results are due to the longer transmission lines which couple to the nearby RF-MEMS switch structure (see Fig. 4.4). The losses due to the BCB-package are equal to 0.1-0.5 dB at 70-95 GHz. Figure 4.5(d) shows another measured results of a GaAs MEMS Dicke switch network (without a BCB cap) which were overlooked in **Paper I**. The W-band GaAs RF-MEMS Dicke switch results are summarised in Table 4.1.

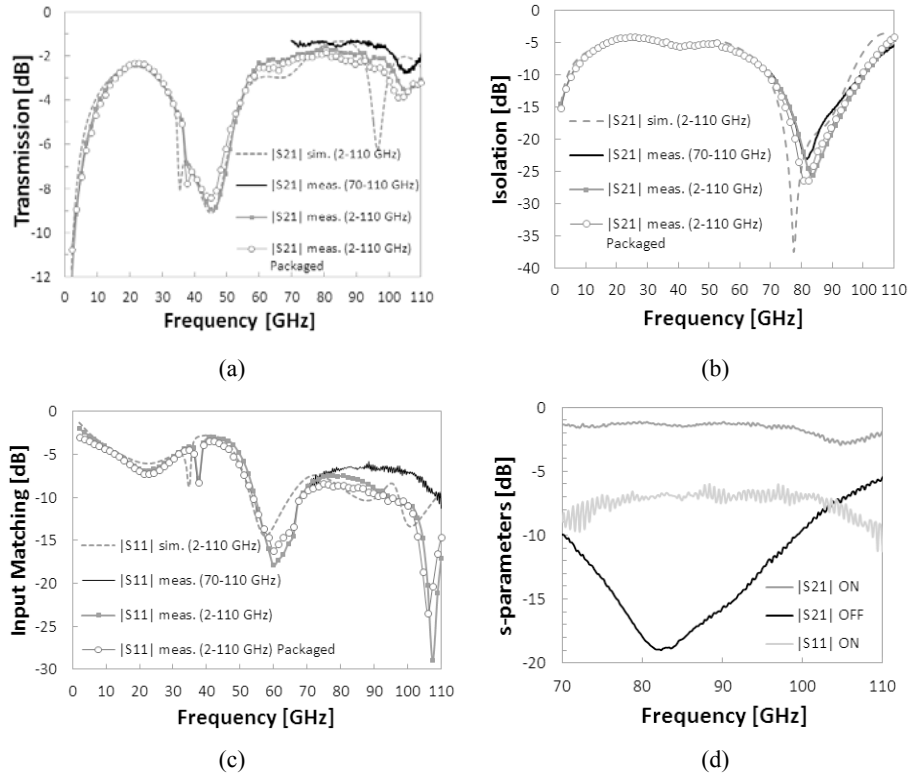


Figure 4.5. Measured and simulated s-parameters of uncapped and BCB capped W-band GaAs MMIC based RF-MEMS Dicke switch networks: ON state  $|S_{21}|$  (a), OFF state  $|S_{21}|$  (b), ON state  $|S_{11}|$  (c), and on-wafer s-parameters of an uncapped GaAs MEMS Dicke switch (d).

Table 4.1. Measurement results of tested W-band GaAs RF-MEMS Dicke switch networks.

Dicke Switch	Loss (dB) (70-96 GHz)	Input Matching (dB) (70-100 GHz)	Isolation (dB) (70-100 GHz)
On-wafer (uncapped)	1.1-1.6*	$\geq -6^*$	10-19*
On-wafer (uncapped)	1.3-1.7	$\geq -6$	10-23
On-chip (uncapped)	1.6-2.0	$\geq -7$	10-26
On-chip (packaged)	1.8-2.7	$\geq -8$	10-27

\* The best case results which were overlooked at the time of the publication (see **Paper I**).

### 4.3 Summary and Discussion

Table 4.2 compares the results of the evaluated GaAs RF-MEMS Dicke switch circuits with other reported SPDT switch designs at W-band. Dicke switches are absorptive type of switch networks because the third RF port is terminated via a 50 ohm resistor whereas SPDT switches are reflective type

of switches which may result in lower losses as compared to Dicke switches [35]. Some silicon based transistor switches presented in [6], [4] and [67] have 2-5 dB of losses (the receiver noise figure values are around 10 dB) which can be considered too high for W-band passive imaging applications. A recently reported SPDT switch demonstrated better switch performances (1.4-1.7 dB of insertion loss together with 19 dB of isolation at 94 GHz) using a 180/90 nm SiGe BiCMOS process by selective emitter shrink [71]. A W-band SPDT switch implemented using PIN diodes in IBM's 90 nm SiGe BiCMOS technology has shown 1.4/22 dB of min/max  $|S_{21}|$  (ON/OFF) [34]. Compared with such PIN diodes based switch networks, MEMS switches are also known to have a higher linearity and consume less DC power that are quite attractive features for high dynamic range and low-power applications.

A SiGe RF-MEMS based SPDT switch circuit with below 1 dB of losses at 70-90 GHz and 15-25 dB of isolation at 70-110 GHz was presented in [53]. The results show possibilities for achieving both low losses and high isolation at W-band using RF-MEMS switches. However, the combined SiGe RF-MEMS switched LNA design reported in [53] had a measured NF of 8 dB at 77 GHz which is too high to be useful for many demanding low-noise/high-sensitivity (e.g. radiometer) receiver applications.

A GaAs transistor based SPDT switch circuit achieved a loss of 1.8 dB at 94 GHz (below 2 dB at W-band) with around 20 dB of isolation [72] whereas a GaAs PIN diode based SPDT switch network reported 1-2 dB of losses and 25-37 dB of isolation at 90-95 GHz, respectively [73]. The best results from the on-wafer measurements of the fabricated GaAs RF-MEMS Dicke switch networks show 1.1-1.6 dB of transmission losses together with 10-19 dB isolation at 70-96 GHz, respectively (see Table 4.2). The measured in-band losses are similar to the performance of a GaAs PIN diode based SPDT switch design with 1.1-1.6 dB of losses and 21-23 dB of isolation at W-band [74]. Furthermore, this resonated vertical PIN diode based SPDT was fabricated using an in-house developed technology that are not commonly available in many GaAs MMIC foundry processes such as the OMMIC process.

As a possible next step, the low loss and high isolation RF-MEMS Dicke switch circuits could be combined with W-band LNA and detector circuitry on the same GaAs chip to enable a switched high performance/sensitivity single-chip receiver front-end. OMMIC has developed GaAs LNAs with a noise figure of 2-4 dB at W-band which is comparable to the noise properties of commercially available InP LNAs in this frequency range [25]. The in-band noise figure of a GaAs MMIC based RF-MEMS Dicke switched LNA may then potentially reach 3-5 dB if we assume roughly 1 dB of losses for an optimised Dicke switch network as shown in Fig. 4.3(b), (close to 0.5 dB of higher switch losses is expected when a BCB cap is used).

Table 4.2. Performance comparison between the presented GaAs RF-MEMS Dicke switch and other reported W-band SPDT switch networks realised in different technologies.

Ref.	Technology	Frequency (GHz)	$ s_{21} $ ON (dB)	$ s_{21} $ OFF (dB)	Switch type
[6]	120 nm BiCMOS	94-100	2.3	21	SPDT*
[4]	180 nm CMOS	75-100	2.8–3.5	21	SPDT
[67]	65 nm CMOS	94-110	4	25-27	SPDT
[72]	GaAs HEMT	75-110	1.8–2	20-22	SPDT
[73]	GaAs PIN diode	90-95	1-2	25-37	SPDT
[74]	GaAs PIN diode	75-110	1.1–1.6	21-23	SPDT*
[71]	90 nm SiGe BiCMOS	94-110	1.4-1.7 <sup>†</sup>	19	SPDT
[34]	SiGe PIN diode	75-110	1.4-2	20-22	SPDT
<b>This Work (meas.)</b>	<b>GaAs MEMS</b>	<b>70-96</b> <b>70-96</b>	<b>1.3-1.7</b> <b>1.1-1.6<sup>#</sup></b>	<b>10-23</b> <b>10-19<sup>#</sup></b>	<b>Dicke</b>
<b>Compact design (sim.)</b>	<b>GaAs MEMS</b>	<b>76-96</b>	<b>0.5-1.3</b>	<b>15-29</b>	<b>Dicke</b>

\*During measurements the passive port was terminated with a 50 ohms resistor, <sup>†</sup> including pad losses i.e. 0.17-0.34 dB, <sup>#</sup> new measured results.

## 5. W-Band RF-MEMS Switched LNA MMIC in a 70 nm GaAs mHEMT Process

This chapter starts with a short background on the monolithic integration of MEMS switches and active RF circuits in the microwave and mm-wave range. It is followed by the target requirements and estimated RF properties of a W-band GaAs switched LNA design based on a micro-strip RF-MEMS Dicke switch and a commercially available LNA. Finally, the chapter covers the monolithic integration of a CPW RF-MEMS Dicke switch and a W-band LNA in a 70 nm mHEMT technology. Such MEMS switched LNA MMICs with a high gain, and low noise figure may be used in mm-wave radiometers for calibration purposes and compensation of receiver gain variations [4], [6], [15].

The simulations of the MEMS based Dicke switch network and the fixed/switched LNA MMICs were made by the author of this thesis. The layouts were made by the co-author Carl Samuelsson. Further details of these works are covered in **Paper II**.

### 5.1 Motivation and Background

Wireless communication, space, defense and security applications operating in the microwave and millimeter-wave range require high performance wideband and reconfigurable integrated circuits. RF-MEMS switches due to their attractive properties such as low losses/DC power, high isolation and linearity have been proposed as an enabling technology for adaptive front-end architecture solutions [56], [57]. The receiver sensitivity could be improved by the monolithic integration of RF-MEMS switches with LNAs, as the losses in front of the first amplifier stage will have an impact on the receiver noise figure. MEMS together with active RF circuitry have been mostly realised so far as hybrid circuits and mainly below 30 GHz [75]–[81] with a few notable exceptions [31], [48]–[50], [82], [83] which still leaves room for significant improvements to be made in terms of RF performance, frequency range, functionality and higher integration. The first MEMS based switched active GaAs MMICs were demonstrated up to 30 GHz [82], [83]. More recently, some GaAs and silicon MEMS LNA ICs reported an NF of 2-4 dB and 7-8 dB up to 26.5 GHz and 77 GHz, respectively [31], [48]–[50].

### 5.1.1 Target Specifications for a W-Band MEMS Switched LNA

In a radiometer, where the sensitivity (or thermal resolution) is largely influenced by the receiver (LNA) NF, gain and bandwidth a low-loss Dicke switch network may be used for calibration purposes and compensation of receiver gain variations [4], [6], [15], [84]–[87]. A 140 GHz passive imaging Dicke switched receiver composed of a high-gain LNA and a Dicke switch with a loss of 1 dB (on/off ratio of 8 dB) was realised in a 0.1  $\mu\text{m}$  GaAs HEMT technology [85]. A W-band GaAs switched LNA MMIC with a gain of 7 dB, 20 dB of isolation and 6 dB of noise figure was demonstrated using a 0.1  $\mu\text{m}$  pHEMT technology [88].

The main objective of this study was to monolithically integrate a low-loss RF-MEMS Dicke switch network and a W-band LNA in 70 nm GaAs mHEMT process for the first time. Recently reported ohmic contact based MEMS Dicke switch networks made on a 100  $\mu\text{m}$  thick GaAs substrate achieved a minimum loss of 1 dB and more than 20 dB of isolation at W-band [89] (**Paper I**). Some earlier W-band LNA designs made in OMMIC's 70 nm mHEMT technology (D007IH) reported a noise figure of 2-4 dB [63], [64] and one can thus expect that a corresponding GaAs based MEMS switched LNA potentially could reach an NF of 3-5 dB if realised in the same process and assuming 1 dB of switch losses.

To improve the receiver sensitivity of a radiometer the switched LNA should provide a low NF together with a high gain, switched isolation and large bandwidth [15]. Table 5.1 shows the target characteristics for an RF-MEMS based switched LNA MMIC design at W-band.

Table 5.1. Target values of a W-band RF-MEMS switched LNA MMIC in a 70 nm GaAs mHEMT process.

Gain (dB)	Isolation (dB)	Noise Figure (dB)	Bandwidth (GHz)
10-20	10-20	3-5	15-20

## 5.2 W-Band RF-MEMS LNA Designs and Results

### 5.2.1 RF-MEMS Dicke Switched LNA (Micro-strip designs)

This section presents the estimated RF performance of a micro-strip W-band RF-MEMS Dicke switched LNA made on a 100  $\mu\text{m}$  thick GaAs substrate. The predicted results of such a MEMS switched LNA have been derived by simulating the s-parameters of the W-band Dicke switch and LNA designs in ADS. The s-parameters used are the simulated data of the micro-strip MEMS Dicke switch (see Fig. 4.3(b)) and the measured results of a micro-strip LNA in OMMIC's 70 nm mHEMT technology [25]. The MEMS Dicke switch circuit has a simulated transmission/isolation loss of 0.5-1.3/15-29 dB



at 76-96 GHz. Figure 5.1(a) shows the measured s-parameters of the COTS W-band LNA [25] and simulated data of the Dicke switched LNA design. The micro-strip RF-MEMS switched LNA has 20-24 dB and 14-27 dB of simulated gain and switched isolation at 70-110 GHz and 76-96 GHz, respectively. Figure 5.1(b) compares the simulated noise figure of the MEMS switched LNA design and the COTS LNA, respectively. The MEMS LNA noise figure is between 3-5 dB at 75-106 GHz, and it is up to 1 dB higher than that of the fixed LNA at 79-104 GHz. These results show the potential in fulfilling the target values of a W-band switched LNA with high gain, isolation and low NF over a relatively wide bandwidth (20 GHz or wider).

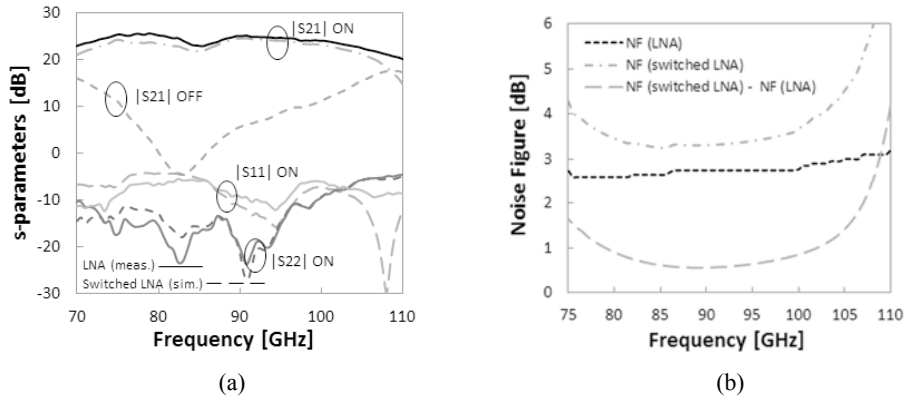


Figure 5.1. Comparison between the measured s-parameters of a W-band LNA MMIC and the simulated s-parameters of a W-band RF MEMS Dicke switched LNA (a), and simulated noise figure of the W-band LNA and MEMS switched LNA designs, respectively (b).

### 5.2.2 RF-MEMS Dicke Switched LNA (CPW designs)

The RF-MEMS micro-strip W-band Dicke switch circuit (see Section 4.2.2) was fabricated in OMMIC's 0.13  $\mu\text{m}$  GaAs pHEMT process (D01PH) with 100 GHz/180 GHz  $f_T/f_{\text{max}}$ . The 70 nm mHEMT technology (D007IH) has  $f_T/f_{\text{max}}$  of 300 GHz/460 GHz making it more suitable for low-noise mm-wave applications. Compared with the micro-strip W-band LNA design [25] made on a 100  $\mu\text{m}$  thick GaAs substrate, a CPW W-band LNA also made in the same process shows somewhat lower measured gain/noise figure (15-22 dB/2-4dB) at 80-110 GHz, respectively [64]. It was decided to monolithically integrate a co-planar W-band MEMS switched LNA since the somewhat risky back-side processing step could then be avoided at this stage of process development (as the fabrication of unprotected MEMS was considered here). A substrate thickness of 200  $\mu\text{m}$  was used for the MEMS and LNA MMIC designs. Figures 5.2 show a block schematic and photograph of a W-band MEMS switched LNA GaAs MMIC. The chip area is 4 x 2 mm<sup>2</sup> (breakouts of the CPW W-band LNA and Dicke switch network were also included).

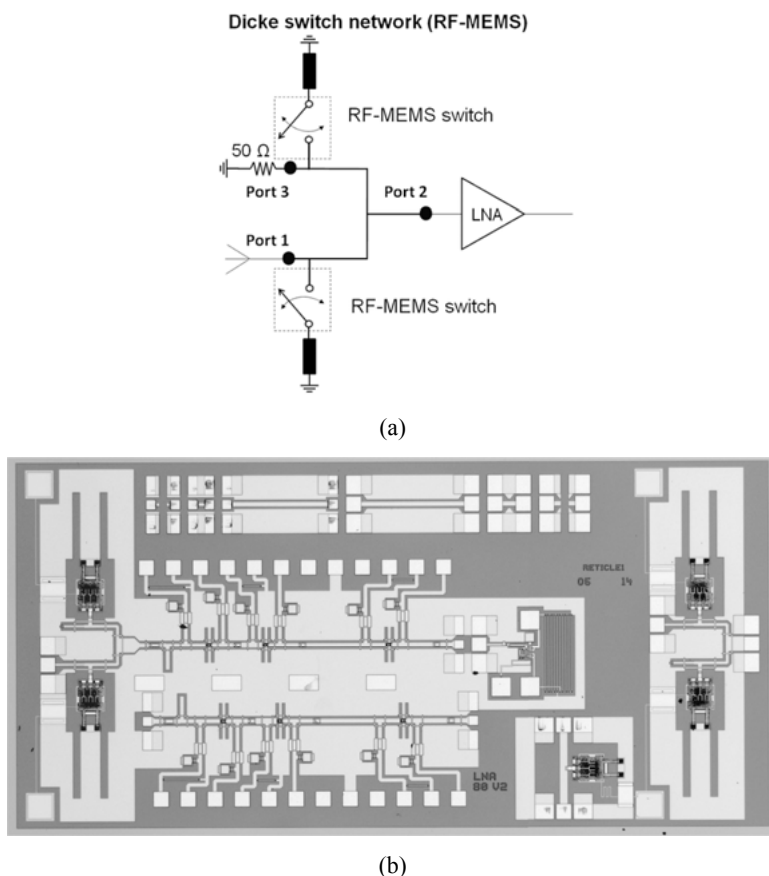


Figure 5.2. Block schematic (a), and micrograph (b) of a W-band RF-MEMS switched LNA (receiver) GaAs MMIC (the switched LNA and breakouts circuits of the LNA and MEMS Dicke switch network are shown to the left and right, respectively).

### 5.2.2.1 RF MEMS Dicke Switch Network

The MEMS Dicke switch network was made to obtain as low in-band losses and high isolation as possible within the 70-90 GHz range. The MEMS based Dicke switch was realised as an SPDT switch network with one input/output port. The third port is terminated to ground via an on-chip 50  $\Omega$  resistor (see Fig. 5.2(a)). Two MEMS switches shunt connected to the tee-junction at a quarter wavelength ( $\lambda_g/4$ ) distance set the resonance frequency of the Dicke switch along with the connecting transmission lines to ground. In the transmission (ON) state the MEMS switch at port 1 is in the up-state while the other one is in the down-state and this results in a low impedance in the transmission branch (from port 1 to port 2) and a high impedance in the other branch, and vice versa for the isolation (OFF) state. The RF-MEMS Dicke switch network (complete structure) was simulated and optimised in Sonnet using a foundry-provided (3D) EM MEMS switch model.

The s-parameters of the fabricated Dicke switch were measured using a two-port network analyser connected to a probe station. The effects of the RF pads were removed by using thru-reflect-line (TRL) on-wafer calibration standards. Figure 5.3 shows the measured and simulated s-parameters of the Dicke switch network that are in a relatively close over-all agreement. The measured Dicke switch transmission losses are equal to 2-3 dB and 10-16 dB at 70-87 GHz and 70-84 GHz, when switched ON/OFF respectively.

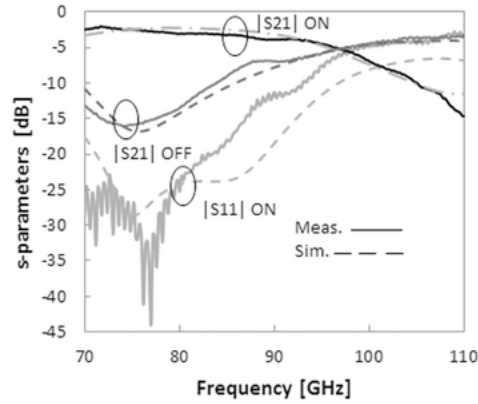


Figure 5.3. Measured and simulated s-parameters of a W-band RF-MEMS Dicke switch network realised in a 70 nm mHEMT GaAs process.

### 5.2.2.2 W-Band LNA

Figure 5.4 shows the schematic of the three-stage LNA. The LNA circuit is based on a previous three-stage amplifier design [63], [64]. The LNA design was simulated in ADS using the EM-simulated results of the passive structures and the foundry provided transistor model (with a gate width  $W_g$  of  $2 \times 15 \mu\text{m}$  in all three stages). The total drain DC bias current ( $I_{DD}$ ) and voltage ( $V_{DD}$ ) was 15 mA and 1 V during simulations and testing (see **Paper II**). The on-wafer s-parameter measurements were done using a two-port network analyser connected to a probe station. The effects of the RF pads were removed by using TRL on-wafer calibration standards.

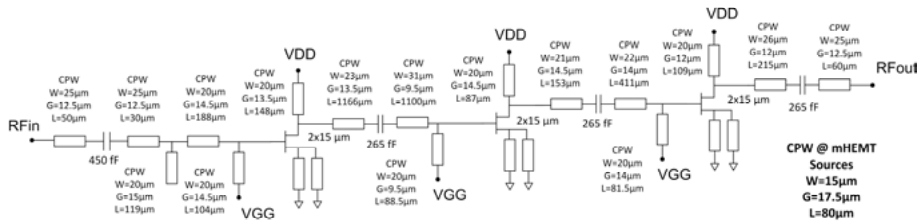


Figure 5.4. Simplified circuit schematic of a W-band three-stage LNA.

Figure 5.5 shows the measured and simulated s-parameters of the W-band GaAs LNA. The maximum measured LNA gain is 10-18 dB at 78-110 GHz which is close to the original LNA design presented in [64] with a peak gain around 20 dB at W-band. Compared with simulations, the measured LNA gain peak shifted from 80 GHz to 84 GHz and  $|S_{21}|$  is 1-5 dB higher than simulated above 83 GHz. The measured transistor gain is up to 1-2 dB higher than simulated based on the foundry mHEMT model and this may explain why the measured LNA gain is some dBs higher than simulated at 83-110 GHz (see Fig. 5.6). Furthermore, the discrepancies could be due to the 80  $\mu\text{m}$  long CPW lines that were used to minimise the noise figure using source peaking (see Fig. 5.4), whereas the sources of some mHEMT transistors (included on the same wafer) were connected to ground using significantly shorter lines. For a closer agreement between the measured and simulated results LNA, mHEMT test structures with longer CPW line source connections could be realised to update and improve the models for future designs as shown in [63].

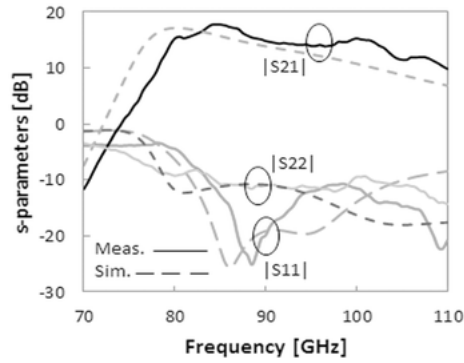
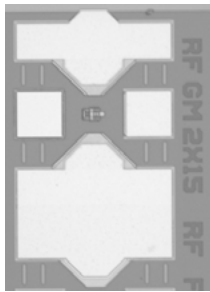
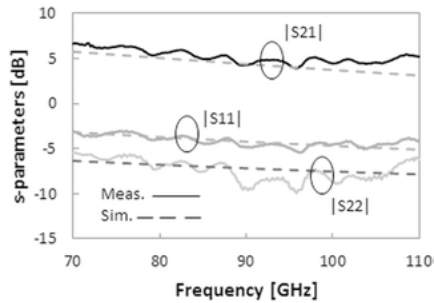


Figure 5.5. Measured and simulated s-parameters of a three stage W-band LNA.



(a)



(b)

Figure 5.6. Micrograph of a 70 nm GaAs mHEMT test device (2 x 15  $\mu\text{m}$  gate width) (a), and on-wafer measured and simulated mHEMT s-parameters (b).

### 5.2.2.3 RF-MEMS Dicke Switched LNA

The main purpose of the MEMS based MMIC designs was to validate the RF performance when combining on the same wafer for the first time high-frequency low-noise 70 nm mHEMTs with low-loss MEMS switches. The switched LNA design was simulated in ADS using the measured s-parameters of the Dicke switch and LNA breakout circuits. The s-parameters of the Dicke switched LNA was measured using the same measurement set-up which was used to measure the previous LNA and Dicke switch circuits. Figures 5.7(a-b) show measured and simulated s-parameters of the W-band MEMS LNA when switched ON/OFF, respectively ( $V_{DD}=1$  V,  $I_{DD}=15$  mA).

The MEMS switched LNA has a measured maximum gain of 15.6 dB (ON) at 81.4 GHz and the gain is 15.3 dB (ON) and 4.4 dB (OFF) at 80.4 GHz, respectively (corresponding to 11 dB of switched LNA isolation). The measured ON/OFF state switched LNA gain values are equal to 10.2-15.6 dB and 1.3-8.2 at 79-96 GHz, respectively. The discrepancies between the measured and simulated  $|S_{21}|$  and  $|S_{11}|$  results may be due to a tapered CPW line which was used to connect the Dicke switch and the LNA in the same circuit (see Fig. 5.2(b)). This may cause some mismatching when the Dicke switch and LNA circuits are connected. The higher measured  $|S_{11}|$  than simulated could be explained by the higher measured input reflections of the Dicke switch and LNA designs, respectively (see Fig. 5.3 and 5.5).

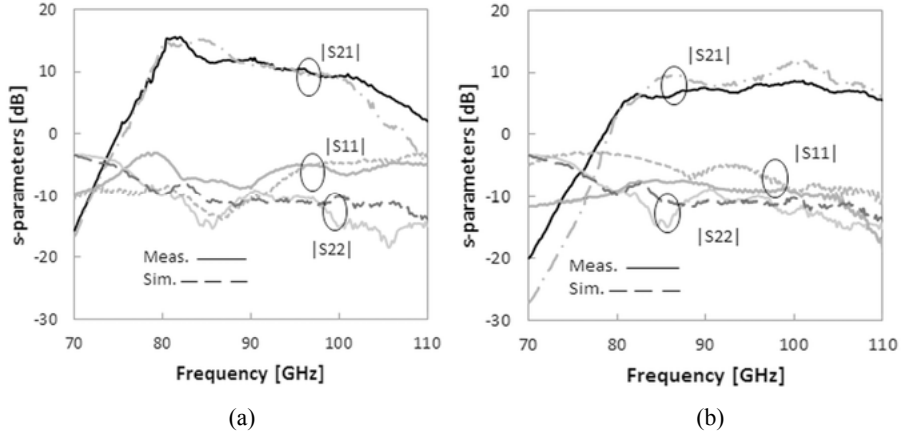


Figure 5.7. Measured and simulated s-parameters of a W-band RF-MEMS switched LNA GaAs MMIC. ON state (a), and OFF state (b).

The W-band noise figure measurements were carried out using a noise figure analyser and a noise source connected to the input of the device under test (the noise figure characterisations were done at VTT Technical Research Center of Finland).

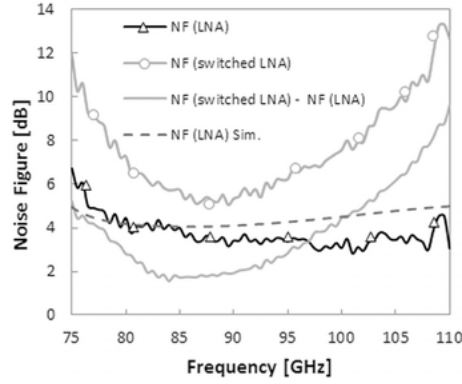


Figure 5.8. Comparison between the noise figure results of a W-band LNA (break-out circuit) and a W-band RF-MEMS switched LNA GaAs MMIC, respectively.

Figure 5.8 shows measured and simulated noise figure of the W-band LNA and measured noise figure of the RF-MEMS switched LNA. The measured LNA noise figure is equal to 2.8-4.6 dB at 79-110 GHz. The NF for the LNA itself is expected to be 0.3 dB below those values as the effects of the RF pads were not de-embedded in these measurements. The measured NF of the MEMS switched LNA is equal to 5.1-6.2 dB at 82-95 GHz ( $V_{DD}=1$  V,  $I_{DD}=14$  mA). These results are 1.6-2.8 dB higher than that of the W-band LNA and this is also in line with the 2-3 dB of measured in-band losses for the MEMS Dicke switch used in this design (see Fig. 5.3).

### 5.3 Summary and Discussion

Only a few RF-MEMS LNAs have been demonstrated at frequencies above 30 GHz. Two silicon based 60-77 GHz and 24-79 GHz LNAs are the first known examples of mm-wave MEMS switched active IC designs [49], [50]. Some 10-30 GHz GaAs MEMS switched low-noise and power amplifier MMICs were presented in [31], [48], [82], [83] and it remains to this date as the highest reported frequency range for active RF-MEMS based MMICs. The proposed MEMS Dicke switched LNA MMIC is believed to be a first time realisation of an RF-MEMS Dicke switch network and a W-band LNA fabricated in a 70 nm mHEMT technology.

Table 5.2 shows a summary of results in comparison with some earlier reported W-band switched LNA designs realised in different technologies. Two Silicon based Dicke switched LNAs reported high values of gain but also a high noise figure (10 dB or higher) [6], [15]. The characterised RF-MEMS Dicke switched LNA obtained a gain of 10-16 dB at 79-96 GHz together with up to 11 dB of switched isolation. The measured noise figure is 5.1-6.2 dB at 82-95 GHz (i.e. 1.6-2.8 dB higher than that of the LNA itself).

Compared with an earlier presented W-band GaAs switched LNA MMIC the W-band MEMS Dicke switched LNA design results in an improvement in terms of 9 dB higher in-band gain and 1 dB lower noise figure [88]. Furthermore, the simulated results of a micro-strip MEMS Dicke switched LNA show the possibilities of achieving more than 20 dB of gain, 14-27 dB of switched isolation and 3-4 dB of noise figure in a 20 GHz bandwidth, respectively. Thus, such an RF-MEMS based switched LNA MMIC could fulfill the specified target requirements of a high-performance single-chip reconfigurable W-band radiometer receiver front-end.

Table 5.2. W-band switched low-noise amplifiers realised in different technologies.

Reference	[88]	[6]	[15]	<b>This work</b>	<b>This work (sim.)</b>	<b>Target values</b>
Frequency (GHz)	80-100	80-110	70-110	79-96	76-96	76-96
Gain (dB)	7	N/A	30	16	24	10-20
Isolation (dB)	20	20	27	11	27	10-20
Noise Figure (dB)	6	10	10	5	3	3-5
Technology	GaAs pHEMT	SiGe HBT	SiGe HBT	GaAs mHEMT (CPW)	GaAs mHEMT ( $\mu$ -strip)	

## 6. Millimetre-Wave RF-MEMS SPDT Switch Networks in a SiGe BiCMOS Process

This chapter covers the design and results of some mm-wave RF-MEMS based switch networks that were fabricated in IHP's 0.25  $\mu\text{m}$  SiGe BiCMOS process technology. Three different SiGe RF-MEMS SPDT switch networks were designed at 40 GHz, 60 GHz and 80 GHz, respectively. The circuit simulations of the SiGe MEMS switch networks were made by the author of this thesis and the layouts were implemented by co-author Carl Samuelsson. The experimental results obtained from on-wafer testing of more than 300 of such SiGe MEMS SPDT switches demonstrate a high fabrication yield and good process repeatability. Further details are included in **Paper III**.

### 6.1 Motivation and Background

Many wireless applications require RF switches and switching networks to fulfill the ever increasing demands on enhanced system functionalities (such as higher performance, lower power consumption and smaller form factors). Such switches can be used to provide redundancy in satellite payloads, re-configurability in wireless communication, band selection in multi-band systems, transmit/receive switching or Dicke switching in radiometers [51], [70], [6]. Solid-state switches using diodes or transistors are commonly used in such systems. However, they can be narrow band, non-linear and have relatively high losses, particularly at mm-wave frequencies [35].

RF-MEMS switches have the potential to become a better option than such switches for certain applications due to their attractive RF properties such as low losses/DC power and high isolation/linearity [36], [37]. Also, compared with ohmic contact MEMS switches, capacitive MEMS switches can reach low losses and high isolation at higher frequencies and could then be a more preferable choice in the mm-wave range. The SiGe foundry IHP developed capacitive MEMS switches which are realised using the Back-End-Of-Line (BEOL) metallisation of a BiCMOS process [90]. Instead of using bond-wires, a monolithic integration will result in shorter connections between MEMS switches and active circuits that are made on the same chip. This will then provide lower losses for such interconnects, especially at mm-wave frequencies and potentially also lower manufacturing/assembly cost.



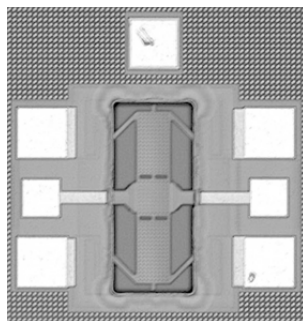
Such high-performance SiGe MEMS switches may be used then to realise single-chip reconfigurable (wideband/multi-band) mm-wave active circuits for wireless and RF-sensing systems up to 100 GHz and beyond.

## 6.2 SiGe RF-MEMS Switch Circuits and Results

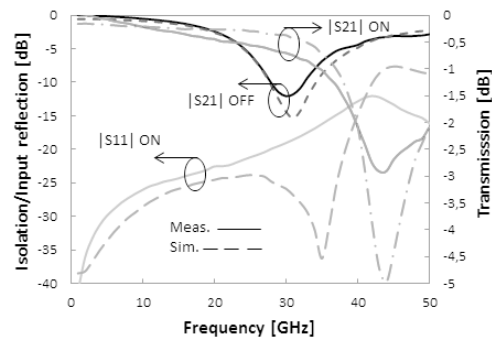
### 6.2.1 RF-MEMS SPST Switch Network

The capacitive MEMS switches were developed by IHP in a 0.25  $\mu\text{m}$  SiGe BiCMOS process (SG25H1). This technology includes five metal layers (M1, M2, M3, TM1 and TM2) and the MEMS switches are realised using the bottom metals M1-M3 [90]. Figure 6.1(a) shows a chip photograph of such a MEMS SPST switch network that were included in a SiGe process run (the circuit area is  $540 \times 410 \mu\text{m}^2$  with the RF and DC pads). The MEMS shunt switch is in the up-state position when it is not biased (ON state). The low switch capacitance to ground (25-30 fF) provides a low-loss transmission path between the RF input and output ports [90]. A higher switch capacitance to ground (210-250 fF) exists when the MEMS switch is in the down-state position (OFF state) which results in a higher attenuation between the ports. An actuation voltage of 30-50 V is needed for switching.

The SPST circuit was simulated using the EM simulation tool Sonnet and the foundry-provided s-parameters of the capacitive MEMS switch used here. The size of this switch corresponds to a centre frequency of 30 GHz (i.e. the frequency where the maximum isolation is expected to occur). All substrate, metal and dielectric layer definitions were defined in Sonnet for the EM simulations according to the SG25H1 process flow. RF testing of the fabricated SiGe MEMS switch circuits was performed at the foundry using a probe station, a network analyser and on-wafer calibration standards.



(a)



(b)

Figure 6.1. A SiGe RF-MEMS SPST switch network: chip photograph (a) and measured and simulated s-parameters in up-state (ON) and down-state (OFF), respectively (b).

Figure 6.1(b) shows the measured and simulated s-parameters of a 30 GHz SiGe MEMS switch (the effects of the RF pads were removed using an open-short de-embedding technique). The SPST MEMS switch has 0.7 dB and 12 dB of measured transmission losses (ON and OFF state) at 30 GHz, respectively (0.4 dB and 15 dB simulated). Compared with the modelled switch data, there is a slight shift in frequency in the measured  $|s_{21}|$  due to a variation in the MEMS switch capacitance [90].

The on and off switching times of such fabricated SiGe MEMS switches are close to 10  $\mu$ s [20]. The long-term switching reliability of the IHP SiGe MEMS switches was demonstrated in life cycle tests showing up to 5-10 billion switch cycles [60]. Furthermore, a glass cap with a silicon frame is used to package the RF-MEMS switches [53]. Such optimised low-loss SiGe MEMS switches achieved less than 0.25 dB of insertion loss and better than 20 dB of isolation in the 30-100 GHz range in 2012 [53].

### 6.2.2 RF-MEMS SPDT Switch Networks

For bench-marking purposes, some 40/60/80 GHz MEMS SPDT switch networks were sent to be fabricated at IHP in April 2011. The capacitive MEMS switches from IHP were still in their development phase at that time. Figure 6.2 shows a chip photo of a 40 GHz SiGe MEMS based SPDT switch network (circuit area is 1 mm<sup>2</sup> incl. RF and DC pads). Co-planar waveguides are used in the SPDT designs as the SiGe BiCMOS technology uses a low-resistive substrate and due to the absence of a well-defined ground plane.

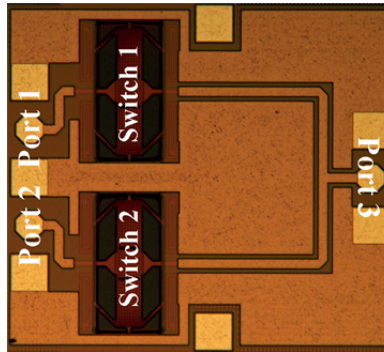


Figure 6.2. A chip photograph of a 40 GHz SiGe RF-MEMS SPDT switch network made in a 0.25  $\mu$ m SiGe BiCMOS process technology.

The SPDT switches were designed with a tee junction using quarter wavelength CPW transmission lines and where two shunt MEMS switches connected in parallel direct the RF signal to one of the two other RF ports (see Fig. 6.2). The tee junction was optimised with respect to input matching at the target frequency using the EM simulation tool Sonnet.

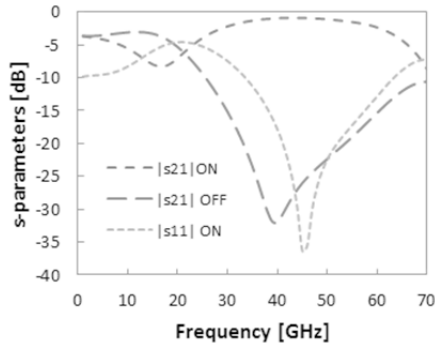


Figure 6.3. Simulated s-parameter results of a 40 GHz capacitive RF-MEMS SPDT switch network in a SiGe BiCMOS process.

Based on the RF-MEMS switch s-parameter data (provided by IHP) and the EM simulated tee junction, the complete SPDT structure was simulated in ADS. Figure 6.3 shows the simulated results of a 40 GHz RF-MEMS SPDT switch circuit with 1 dB/32 dB of transmission losses/isolation at 40 GHz, respectively.

The RF testing of each SPDT design was done at IHP on more than 100 MEMS switch circuits across a fabricated SiGe eight inch wafer. Figure 6.4 shows measured s-parameters of the tested 40 GHz MEMS SPDT switches. The experimental results show quite uniform and repeatable RF properties, thus indicating a relatively high process yield for the fabricated switches. The measured minimum SPDT switch loss is 3 dB at 37 GHz with 10-20 dB of isolation at 30-40 GHz (the impedance matching is below -10 dB at 34-46 GHz). As shown in Fig. 6.4, a frequency shift occurred in the measured  $|s_{21}|$  responses which may be related to variations in MEMS switch capacitance [90]. Compared with simulations, the lowest measured SPDT switch loss is 2 dB higher than anticipated. Since the RF pads were not deembedded in this case the measured SPDT data include about 1 dB of pad losses (based on a measured on-chip through standard with similar RF pad dimensions that was included in another process run). The remaining difference between the measured and simulated SPDT switch losses (roughly 1 dB) may be explained by a limited accuracy in the EM simulations and a higher measured MEMS switch loss (as indicated by the SPST data shown in Fig. 6.1(b)).

The losses of the IHP MEMS switches were later improved by using M2 and M3 metal layers in the RF signal line (whereas only M2 was used in the initial version of the IHP MEMS switches) as well as optimising the width of the signal line as reported in 2012 [53]. The corresponding experimental results of more than 200 tested 60 GHz and 80 GHz SiGe MEMS SPDT switch networks can be found in **Paper III**.

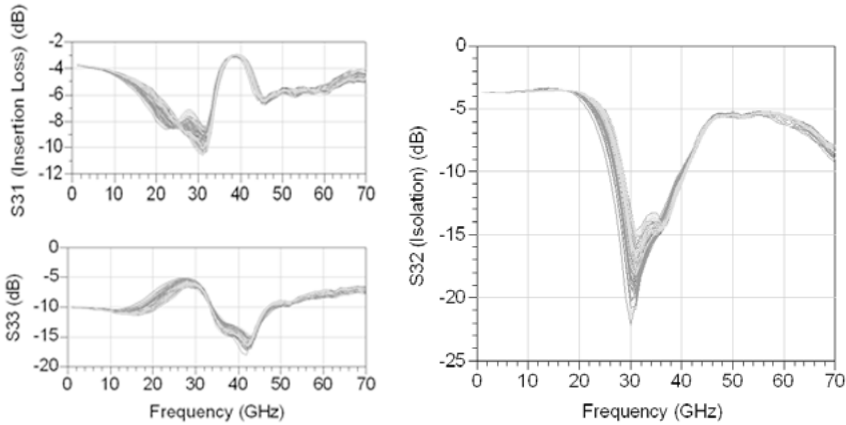


Figure 6.4. 40 GHz RF-MEMS SPDT switch circuits fabricated in a SiGe RFIC foundry process: measured s-parameter data (insertion loss  $s_{31}$ , input return loss  $s_{33}$  and isolation  $s_{32}$ ) of more than 100 of such tested MEMS switch circuits across a fabricated eight inch wafer.

### 6.3 Summary and Discussion

This chapter presented the results of a 40 GHz RF-MEMS SPDT switch network made in a 0.25  $\mu\text{m}$  SiGe BiCMOS process from the foundry IHP. The simulated minimum/maximum MEMS SPDT switch loss and isolation are equal to 1 dB and 32 dB at 40 GHz, respectively. The corresponding measured SPDT switch loss was found to be 1 dB higher after subtraction of the expected RF pad losses. This difference may be due to higher MEMS switch losses on this initial process run and limited accuracy in the SPDT EM simulations (an s-parameter based foundry switch model was used here). A closer agreement between the measured and simulated results is expected if the SPDT switch network could be co-simulated using a more accurate (EM) model of the MEMS switches used in this circuit design.

The experimental data that was obtained from on-wafer testing of more than 300 SPDT switches further implies a high fabrication yield and process repeatability of the manufactured mm-wave SiGe MEMS switch circuits.

The measured SPDT switch results compare favorably with a 60-70 GHz SiGe MEMS SPDT switch [91]. More recently, IHP presented SiGe MEMS switches optimised for specific frequency bands by using of an inductive loading technique [53]. Such micro-strip SiGe MEMS SPDT switches showed less than 1 dB of losses and more than 20 dB of isolation at 30/50/80 and 100 GHz, respectively [53]. This could then open up possibilities for realising mm-wave high performance reconfigurable SiGe MEMS switched RF front-ends with a high process yield and high switching reliability.

## 7. Monolithic Integration of a SiGe RF-MEMS Dicke Switch Network and a Wideband LNA

This chapter starts with a background on different integration possibilities of MEMS switches and active RF devices in both GaAs and silicon based IC processes. Afterwards, it presents a novel monolithic integration of a 30 GHz RF-MEMS Dicke switch and a wideband LNA in a 0.25  $\mu\text{m}$  SiGe BiCMOS process. Such a switched LNA RFIC design with a high gain and isolation is considered for a possible use in mm-wave SoC radiometers (e.g. at Ka-band) for calibration purposes and compensation of receiver gain variations.

The circuit simulations for the presented SiGe RF-MEMS and LNA RFIC designs were made by the author of this thesis. The layouts were done by Carl Samuelsson. Further details of these works are covered in **Paper IV**.

### 7.1 Motivation and Background

Reconfigurable and broadband ICs are essential elements in many of today's RF system solutions for wireless communication, space, defense and security applications within the microwave and millimeter-wave range. RF-MEMS devices (high-performance switches) can offer enhanced re-configurability to the transmitter/receiver front-ends due to their attractive RF properties (low loss/DC power and high isolation/linearity in a wide frequency range). This is especially important in low-noise receivers where the losses before the first amplification stage (i.e. the LNA) have an impact on the over-all noise figure and receiver sensitivity. The integration of MEMS with active circuits have so far mostly been realised as hybrid circuits and mainly at frequencies below 30 GHz [75]–[81] which still leaves room for significant improvements to be made in terms of RF performance, frequency range, functionality as well as to achieve reduced complexity (higher integration) and lower costs. Especially at mm-waves, a monolithic integration of MEMS and active devices could improve the over-all performance of the receiver.

The first MEMS switched active GaAs MMICs were demonstrated up to 30 GHz in 2001 and 2004, respectively [82], [83]. More recently, some GaAs and silicon MEMS LNA ICs reported an NF of 2-4 dB and 7-8 dB up to 26.5 GHz and 77 GHz, respectively [31], [48]–[50].

The SiGe foundry IHP has developed RF-MEMS switches with less than 1 dB of losses and more than 20 dB of isolation in different frequency bands from 30 GHz up to 100 GHz [53].

### *7.1.1 Target Specifications for a 30 GHz MEMS Switched LNA*

In a radiometer chain where the sensitivity (or thermal resolution) is largely influenced by the receiver (LNA) NF, gain and bandwidth a low-loss Dicke switch network may be used for calibration purposes and compensation of receiver gain variations [4], [6], [15], [84]–[87]. SiGe W-band passive imaging receivers (Dicke switched radiometers) with an NF close to 10 dB (incl. 3-5 dB of transistor based switch losses) can be found in [4], [6], [15]. A SiGe D-band (130 GHz) LNA and a Dicke switch with 3 dB/12 dB of losses/isolation are reported in [84]. A 140 GHz high-gain LNA and a Dicke switch with a loss of 1 dB (8 dB on-off ratio) were demonstrated using an advanced and more costly GaAs technology while consuming 0.39 W of DC power [85]. The references [92]–[94] provide some additional examples of transistor, diode and RF-MEMS switched LNAs and receiver modules for space (satellite communication payloads) and passive mm-wave imaging at Ka-band.

The primary objective in this study was to monolithically integrate for the first time a 30 GHz MEMS Dicke switch and a wideband LNA in a 0.25  $\mu\text{m}$  SiGe BiCMOS process from the foundry IHP ( $f_T/f_{\text{max}} = 190 \text{ GHz}/220 \text{ GHz}$ ). This technology was selected based on its suitability for implementing some Ka-band radiometer receivers [95]. High frequency active devices available in this process (SG25H1) are based on SiGe:C HBTs which are size scalable with an emitter area  $A_E = n \times 0.176 \mu\text{m}^2$  where  $n$  is the number of emitter fingers. The back-end includes a stack of five metal layers (aluminium) which can be used for realising high quality on-chip inductors and MIM capacitors. Poly silicon based resistors are available in this process and used in the design of the MEMS Dicke switch and wideband LNA circuits.

Some wideband LNA designs made in 0.18  $\mu\text{m}/0.25 \mu\text{m}$  SiGe processes reported a noise figure of 4-6 dB at 15-35 GHz [96], [97] and one can thus expect that a single-chip MEMS switched LNA could reach an NF of 5-8 dB (if realised in a similar technology and assuming 1-2 dB of switch losses). Other key features for such a MEMS LNA to be useful in a Dicke switched radiometer front-end are a high gain, isolation ( $\geq 10$ -20 dB) over a broad frequency range. Here, we will target a close to 30% wide instantaneous bandwidth (10 GHz for such a circuit design if made at 30 GHz). Some SiGe W-band LNAs with NF=3-4 dB were recently presented which suggests that the RF properties of a Dicke switched LNA could be further improved and also scaled to higher frequencies using 90/130 nm SiGe processes [21], [22]. Table 7.1 shows the target values of a 30 GHz Dicke switch network and a wideband LNA circuit made in a 0.25  $\mu\text{m}$  SiGe BiCMOS technology.

Table 7.1. Targets of a 30 GHz Dicke switch and wideband LNA in a 0.25  $\mu\text{m}$  SiGe process.

Component	Gain/Loss	Isolation	Noise Figure	Return Loss	Bandwidth
Switch	L= 1-2 dB	10-20 dB	1-2 dB	-10 dB	10 GHz
LNA	G= 10-20 dB	N/A	4-6 dB	-10 dB	10 GHz

## 7.2 SiGe RF-MEMS and LNA Designs and Results

### 7.2.1 RF-MEMS Dicke Switch Network

Figures 7.1(a-b) show the schematic and photograph of a 30 GHz SiGe MEMS switched LNA RFIC (the area is  $1.6 \times 1.6 \text{ mm}^2$ ). Breakouts of the Dicke switch and wideband LNA were included as separate test structures (shown to the right). The Dicke switch was made as a CPW based SPDT switch network where the third port is terminated to ground via an on-chip  $50 \Omega$  resistor. Two MEMS switches are connected to a tee-junction at a quarter wavelength distance to set the input matching of the Dicke switch.

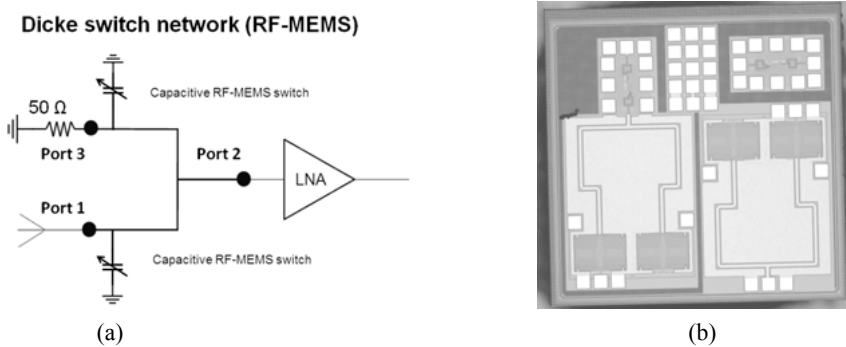


Figure 7.1. Schematic (a) and chip photograph (b) of a 30 GHz SiGe MEMS switched LNA (breakouts circuits of the wideband LNA and Dicke switch network are shown to right).

In the transmission (ON) state the MEMS switch at port 1 is in up-state while the other switch is in down-state and this results in a low impedance in the transmission branch (from port 1 to 2) and a high impedance in the other branch, and vice versa for the isolation (OFF) state. The Dicke switch was simulated in ADS using the EM simulated s-parameters of the CPW transmission line structure together with the measured SPST switch data and a foundry model of the on-chip  $50 \Omega$  resistance. Figure 7.2(b) shows the MEMS Dicke switch s-parameters (de-embedding was made at 2-50 GHz). The Dicke switch has 3 dB/22 dB of measured min/max transmission losses at 25 GHz (simulated 2.5 dB and 18 dB at 30 GHz). The measured ON state  $|s_{11}|$  is below -10 dB at 17-50 GHz.

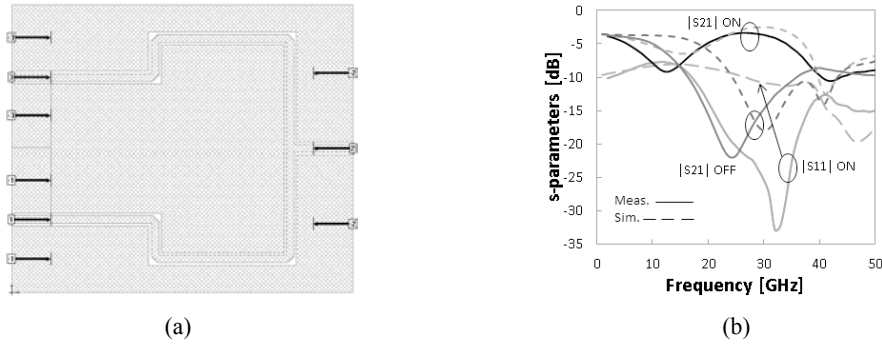


Figure 7.2. A 30 GHz SiGe MEMS Dicke switch: EM model of the CPW structure used in this design (a), measured and simulated s-parameters in ON and OFF state, respectively (b).

The slight frequency shift between the measured and simulated  $|S_{21}|$  data may be due to a variation in MEMS switch capacitance [90]. Furthermore, the discrepancies may be explained by the large center ground area of the CPW structure which is only connected to the two outer ground planes via the RF probes (air bridges were not available in this process). A foundry EM model of the SiGe MEMS switch that could be co-simulated with the co-planar structure is expected to result in a closer agreement between the MEMS switch test results and simulations. Finally, a more compact MEMS Dicke switch network with improved RF properties may be realised based on a micro-strip design where the ground plane is made in metal 1. Such low-loss micro-strip SiGe MEMS SPDT switches are reported in [53] (with less than 1 dB of losses and around 20 dB of isolation at 30 GHz).

### 7.2.2 Wideband LNA

Figure 7.3 shows a circuit schematic of a SiGe wideband LNA design which also was combined with a 30 GHz MEMS Dicke switch network as shown in Fig. 7.1(b) (a breakout circuit is shown in the upper right corner). The LNA circuit area is  $510 \times 300 \mu\text{m}^2$  incl. RF and DC pads. The cascade three-stage LNA design was optimized for high gain, low NF and wide bandwidth by selecting the appropriate DC bias points and the suitable number of emitter fingers ( $n=8$  was used in the three transistor stages as it resulted in the best possible trade-off between providing both circuit stability with a reasonably high gain, low NF and a wideband matching). The peak values of  $f_T$  and minimum noise figure ( $\text{NF}_{\min}$ ) are specified in the process design manual to occur at a collector current ( $I_C$ ) of 16 mA and 5 mA when  $n=8$ . The on-chip inductors ( $L_{\text{in}}=L_{\text{out}}=300 \text{ pH}$ ) were EM simulated and optimized in Sonnet. Resistive feedback was used in the third stage to ensure that the LNA is unconditionally stable ( $K\text{-factor} > 1$  and stability measure  $\mu > 0$ ). The circuit simulations and layout of the SiGe LNA design were performed in Cadence.



The RF tests of the fabricated wideband LNA was made on-wafer at the foundry, using a network analyser connected to a probe station, GSG probes (pitch of 100  $\mu\text{m}$ ), and a multi-contact wedge for applying the DC bias.

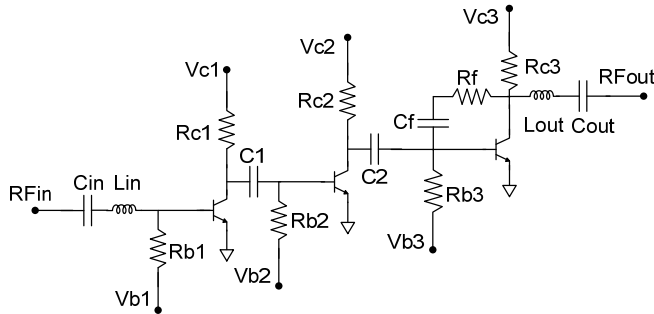


Figure 7.3. Schematic of a SiGe wideband LNA made in a 0.25  $\mu\text{m}$  SiGe BiCMOS process.

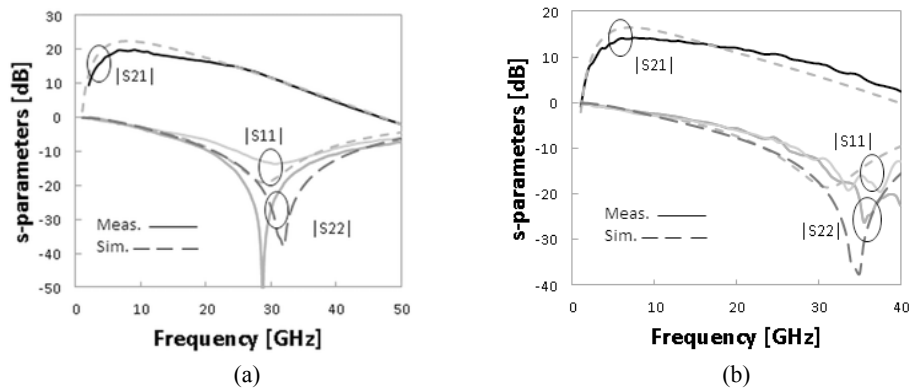


Figure 7.4. Measured and simulated s-parameters of a wideband LNA in a 0.25 $\mu\text{m}$  SiGe process:  $V_{C1}=V_{C2}=V_{C3}=2.5$  V,  $I_C=14$  mA (a) and  $V_{C1}=V_{C2}=V_{C3}=1.25$  V,  $I_C=6$  mA (b).

Figure 7.4(a) shows the on-wafer measured and simulated s-parameters of the three-stage LNA when  $V_{C1}=V_{C2}=V_{C3}=2.5$  V and  $I_C=14$  mA. The small signal gain  $|s_{21}|$  is then 19.9 dB at 9 GHz ( $|s_{21}| \geq 10$  dB at 2-33 GHz). The measured input and output matching ( $|s_{11}|$  and  $|s_{22}|$ )  $\leq -10$  dB from 24 to 39 GHz and 20 to 42 GHz, respectively (the effects of RF the pads were removed by open-short de-embedding at 2-50 GHz). The discrepancies found between the measurements and simulations may be due to process variations.

For the noise figure and linearity measurements a diced chip with the wideband LNA design (shown in Fig. 7.1(b)) was mounted inside a DC test fixture (0.5-1.5 mm long bond-wires were used to connect to the DC pads). The LNA s-parameters, noise figure and linearity were measured using a network analyser connected to a probe station, a calibration module, a noise

source (defined up to 26.5 GHz), a power sensor and a power meter. The LNA s-parameters were in this case measured using a standard impedance calibration substrate (the effects of the RF pads were not de-embedded).

Despite the fact that the wideband LNA circuit was designed to be unconditionally stable, when the same DC bias values were applied to the LNA mounted in a test DC fixture (as were in the previous on-wafer LNA tests) oscillations occurred that may be due the off-chip interconnects used (bond-wires etc) between the power supplies and the DC pads. The measurements were instead performed with a somewhat reduced DC bias at which the LNA was found stable ( $V_{C1}=V_{C2}=V_{C3}=1.25$  V and  $I_C=6$ mA). The LNA gain is equal to 14.2 dB at 7.5 GHz with this bias ( $|s_{21}| \geq 10$  dB at 3-26 GHz) whereas the return losses are better than -10 dB at 27-40 GHz (see Fig. 7.4(b)).

Figure 7.5 shows the measured and simulated noise figure of the SiGe wideband LNA at the same DC bias point. The measured LNA noise figure is equal to 5.9 dB at 26.5 GHz and it is below 7 dB at 13-26.5 GHz.

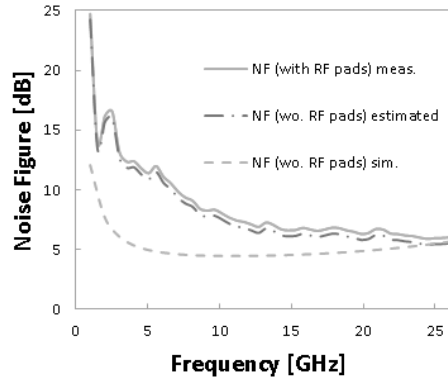


Figure 7.5. Measured and simulated noise figure of a wideband LNA in a 0.25  $\mu$ m SiGe BiCMOS process ( $V_{C1}=V_{C2}=V_{C3}=1.25$  V and  $I_C=6$  mA).

Furthermore, the noise figure of the wideband LNA itself is estimated to be 0.5 dB less than those values after subtraction of the expected RF input pad losses (an on-chip thru standard showed 1 dB of measured losses). The measured and simulated LNA noise figure results are in a relatively close agreement at higher frequencies (the difference is less than 0.5 dB of 24-26.5 GHz). The difference in NF is several dBs higher at lower frequencies where the measured LNA gain is typically also some dBs lower than simulated. The discrepancies between the experimental and theoretical results may be related to a limited accuracy of the passive and active (noise) models used in this amplifier circuit design (e.g. due to process variation and higher passive components loss than predicted). The measured LNA OIP3 values are in the range of -6 dBm to -3 dBm at 10-26.5 GHz when consuming 7.5 mW from a DC power supply (further details are provided in **Paper IV**).

### 7.2.3 RF-MEMS Dicke Switched LNA

Figures 7.6(a-b) show a close-up chip photo and theoretical results of the fabricated SiGe MEMS LNA circuit, respectively ( $V_C=2.5$  V,  $I_C=19$  mA). The Dicke switch was simulated in ADS (based on the EM simulated CPW transmission line structures and the foundry-provided SPST switch model) and the wideband LNA was simulated using Cadence and Sonnet. The MEMS LNA has an expected gain of 10-18 dB and -5 dB to 10 dB at 25-35 GHz when the Dicke switch is switched on and off, respectively (which then corresponds to 8-19 dB of switched isolation). The simulated noise figure of the switched LNA is 6.2-7.9 dB at 25-35 GHz which is close to 2 dB higher than the noise figure of the wideband LNA.

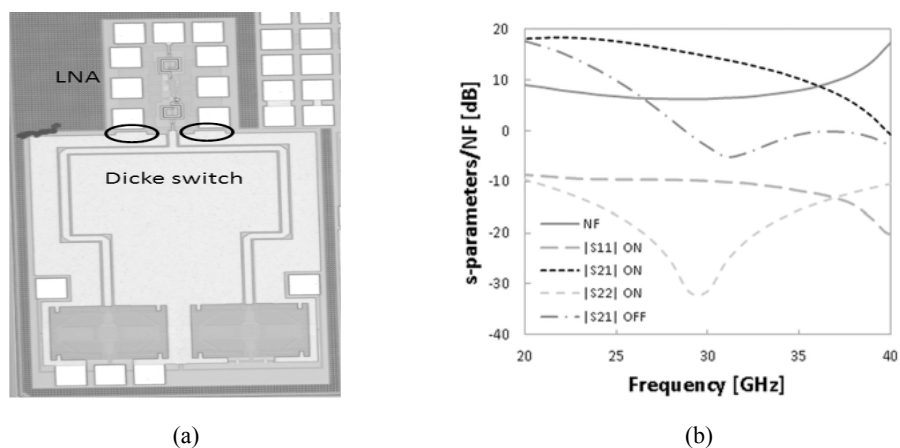


Figure 7.6. An RF-MEMS Dicke switched LNA design made in a 0.25  $\mu\text{m}$  SiGe process: chip photo (a), and simulated s-parameters/noise figure (b). The ellipses indicate regions where some metal via contacts are missing due to a layout mistake.

Figure 7.7 shows measured and simulated ON and OFF state  $|s_{21}|$  of the fabricated SiGe MEMS Dicke switched LNA circuit ( $V_C=2.5$  V,  $I_C=19$  mA). The measured  $|s_{21}|$  is maximum 2 dB when the Dicke switch is in the ON state and this is 16 dB lower than the simulated peak gain values shown in Fig. 7.6(b). An unexpected design mistake that can explain this anomaly was identified as the metal via contacts between the Dicke switch and LNA ground planes were unintentionally missing in the manufactured layout of the MEMS switched LNA (see Fig. 7.6(a)). As a result of this design error the Dicke switch and LNA ground planes were not connected on-chip and although ground connections were provided via the RF probes during the testing, a floating ground occurred as the Dicke switch ground plane to the right was separated and isolated from the other ground planes.

To verify the measured small signal characteristics of the implemented MEMS switched LNA design, this circuit was re-simulated in Sonnet (using the previously derived s-parameters for the passive and active parts) but in

this case without the via contacts supposed to connect the Dicke switch and LNA ground planes together. A closer agreement between the simulated and experimental switched LNA results is anticipated using an EM based MEMS switch model that could be co-simulated with the CPW lines in the Dicke switch network. Compared with the simulated MEMS switched LNA results, there is a some shift in frequency for the measured  $|s_{21}|$  which partly also could be explained by an expected variation in MEMS switch capacitance [90]. To conclude, the measured MEMS LNA has 9-13.5 dB of switched isolation at 24-31 GHz which validates the designed switching function of the Dicke MEMS switch network used in the switched LNA design.

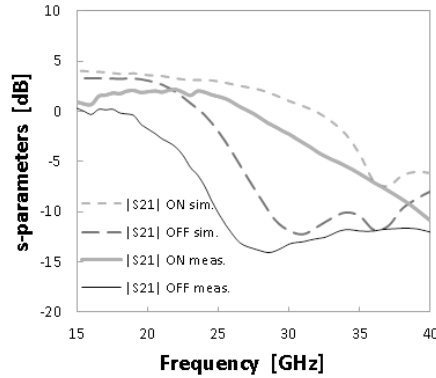


Figure 7.7. Measured and simulated s-parameters of an RF-MEMS Dicke LNA in a 0.25  $\mu\text{m}$  SiGe process ( $V_{C1}=V_{C2}=V_{C3}=2.5$  V,  $I_C=19$  mA) when switched ON and OFF, respectively.

### 7.3 Summary and Discussion

Table 7.2 compares the results of the proposed wideband high-gain LNA RFIC with some previously published state-of-the-art SiGe BiCMOS LNAs. This work achieved both a high gain (10-20 dB) over a much wider bandwidth (2-33 GHz) and broadband input and output matching which are better than -10 dB from 24 to 39 GHz and 20 to 42 GHz, respectively. The measured noise figure results of the proposed LNA are also relatively close to the reported values of some wideband LNAs realised in higher process nodes (see Table 7.2).

Table 7.3 shows a performance summary of III-V and silicon based RF-MEMS switched LNA IC designs within the 10-30 GHz range and beyond. A wideband GaAs RF-MEMS Dicke switched LNA design with 3 dB noise figure at 16-26 GHz was presented in [31]. To this date, the only silicon MEMS LNAs that have been reported for frequencies above 10 GHz are some narrow-band (dual-band) and frequency-agile designs made at 60/77 GHz and 24/74 GHz, respectively [49], [50].

Due to an unexpected layout mistake (missing via contacts between the switch and LNA ground planes) the gain of the fabricated SiGe MEMS LNA design was lower than expected in the ON state. In spite of this design error, the MEMS LNA resulted in 9-14 dB of measured isolation at 24-31 GHz when the Dicke switch was switched on and off, respectively. These MEMS LNA results are also somewhat close to the anticipated 8-19 dB of isolation at 25-36 GHz which thereby validate the switching function of the Dicke switch used in this design. The presented reconfigurable LNA RFIC design is believed to demonstrate a first-time single-chip realisation of a 30 GHz MEMS Dicke switch network and a wideband LNA in a 0.25  $\mu\text{m}$  SiGe BiCMOS process.

The unexpected floating ground issue that occurred in this design may easily be solved in a future updated version of such a MEMS switched LNA. Furthermore, since some low-loss/high-isolation MEMS switches were made in IHP's SG25H1 process [53], an optimised MEMS switched wideband LNA design should reach an NF of 5-6 dB with close to 20 dB of in-band gain and isolation if made in the same SiGe process. Further improvements such as better noise properties (lower NF) and scaling to higher frequencies for a Dicke switched LNA may potentially be realised in more advanced (90/130 nm) SiGe process nodes.

Table 7.2. Performance comparison of SiGe BiCMOS wideband LNA circuit designs.

Ref.	[98]	[99]	[100]	[96]	[97]	<b>This Work</b>
Frequency (GHz)	26-40	3-26	8-18	21-40	10-30	<b>2-33</b>
Gain (dB)	15-23	9	13-16	10-19	10-22	<b>10-20</b>
$ S_{11} $ (dB)	$\leq -10$	$\leq -10$	$\leq -8.5$	$\leq -10$ 21-23 GHz	$\leq -10$ 15-19 GHz	$\leq -10$ <b>24-39 GHz</b>
NF (dB)	3	4-6 2-22 GHz	5-6	5.6 35 GHz	4-5 15-28	<b>5-6<sup>†</sup></b> <b>14-26 GHz</b>
Power (mW)	11	33	38	26	28	<b>8-35</b>
OIP3 (dBm)	4	15*	2*	9	13*	$\leq -3$
Technology	120 nm	130 nm	130 nm	180 nm	250 nm	<b>250 nm</b>

\*estimated based on the given IIP3 data <sup>†</sup>estimated values based on the measured noise figure data (excl. the effects of the RF input pad).

Table 7.3. Performance comparison of RF-MEMS switched LNA RFIC/MMIC designs made in different technologies.

Ref.	[83]	[48]	[31]	[49]	[50]	<b>This work</b>	
						Measured	Simulated
Freq. (GHz)	26-30	18-26	16-34	60/77	24/79	24-31	25-36
Gain (dB)	20-22	≥15	10-17	19-21/ 21-23	25/18	-4 to 2	9-18
Isolation (dB)	N/A	16-20	20-25	N/A	N/A	9-14	8-19
NF (dB)	N/A	2-5	3 16-26 GHz	7/8	4/8	N/A	6-8 25-35 GHz
Tech.	GaAs	GaAs	GaAs	250 nm SiGe	250 nm SiGe	250 nm SiGe	250 nm SiGe

## 8. Wideband SiGe Power Detectors for SoC W-Band Direct-Detection Radiometers

This chapter introduces two novel wideband power detector RFIC designs for a W-band system-on-chip (SoC) direct-detection radiometer front-end. The two power detectors made in IHP's 0.13  $\mu\text{m}$  SiGe BiCMOS process SG13G2 obtain a higher sensitivity (lower NEP) in comparison with earlier reported silicon based W-band detectors and are competitive with InP based W-band power detectors in terms of a higher responsivity and similar NEP. These detectors show better RF properties (higher sensitivity or responsivity) and a more wideband input matching was obtained with an optimised design.

The EM simulations and optimisation of the input matching networks for the two SiGe power detector RFICs were made by the author of this thesis. The active parts of the detector circuitry were designed by Rolf Jonsson. Further details of these works are covered in **Paper V** and **Paper VI**.

### 8.1 Motivation and Background

W-band passive imaging receivers, LNA and power detector circuits have been realised in costly III-V technologies with sensitivity values that are useful for certain radiometer applications [17]–[19]. To increase the integration level and also reduce the cost some highly integrated silicon based W-band Dicke switched receiver RFICs were presented [4], [6], [15]. The overall noise figure of those radiometer front-ends is, however, around 10 dB or higher. To push the performance of such Dicke switched radiometers further beyond the current state-of-the-art, a use of low-loss MEMS switches developed by the foundry IHP may be considered (with 0.5 dB of losses up to 140 GHz) [20]. Two W-band LNA designs made in 90 nm and 130 nm SiGe BiCMOS technologies have 20–34 dB of gain with 3–4 dB noise figure [21], [22] thus approaching the performance of III-V based W-band LNAs. Silicon based switched receivers with 5–6 dB improvement in noise figure may then be feasible at W-band. However, to fulfill the low-noise receiver requirements for W-band passive imaging, a wideband power detector with a high sensitivity should be used after the LNA. Given that the switched LNA has 20–30 dB of gain and 5 dB of noise figure in a 25 GHz bandwidth then the detector should have a NEP in the range of 0.1–1  $\text{pW/Hz}^{1/2}$  (see Fig. 3.2). The results of two SiGe W-band detectors are summarised below.

## 8.2 SiGe Power Detector Designs and Results

### 8.2.1 Detector design based on a narrow-band matching network

Figure 8.1(a-b) show a simplified circuit schematic and a chip photograph of the initial version of a proposed W-band power detector SiGe RFIC design, respectively (circuit area is  $0.2 \text{ mm}^2$  incl. the RF and DC pads). The detector was fabricated in IHP's  $0.13 \text{ }\mu\text{m}$  technology with  $300 \text{ GHz}/500 \text{ GHz}$   $f_T/f_{\text{max}}$ . This circuit is a novel implementation based on some earlier reported power detector designs made in  $0.18 \text{ }\mu\text{m}$  and  $0.25 \text{ }\mu\text{m}$  SiGe processes [15], [66]. In this design, two HBTs ( $Q1$ ,  $Q2$ ) are used for temperature compensation [15]. The two transistors have identical size, biasing resistors ( $R_b$ ,  $R_c$ ) and DC biasing values ( $V_c$ ,  $V_b$ ). In this way, the voltage drift on  $V_{\text{out}}$  and  $V_{\text{ref}}$  due to temperature changes will be identical. The DC voltages ( $V_c$ ,  $V_b$ ) are used to forward bias the base-emitter junction of each bipolar transistor.

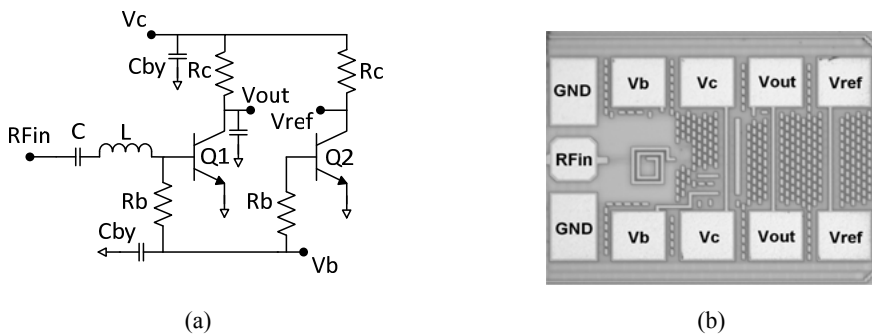


Figure 8.1. Circuit schematic (a) and photograph (b) of a W-band power detector made in a  $130 \text{ nm}$  SiGe technology. A series inductor and a cap are used in the input matching network.

The power level  $P_{\text{in}}$  at the detector input ( $R_{\text{Fin}}$ ) is assumed to be in the range of  $-40 \text{ dBm}$  to  $-30 \text{ dBm}$  if used in a W-band radiometer front-end with  $20\text{-}30 \text{ dB}$  of receiver (LNA) gain (see Chapter 3). A low-loss wideband input matching network will be required in order to maximise the amount of RF power transferred to the detector and optimise the sensitivity of the detector. The input matching network used here consists of a series inductor ( $L$ ) and a capacitor ( $C$ ). The on-chip inductor which is made as a full-custom design uses a  $3 \text{ }\mu\text{m}$  thick top metal layer (the SG13G2 technology provides 7 metal layers and more details are described in the foundry process design manual). The input capacitor is made between top metal 1 and metal 5. EM simulation tool Sonnet was used to optimise the input matching network (incl. all via contacts and interconnecting metal lines) in order to achieve the required input reflection, sensitivity and bandwidth ( $|S_{11}| \leq -10 \text{ dB}$  and  $\text{BW} = 25 \text{ GHz}$ ). All circuit simulations were done in ADS using EM simulated data of the input matching network, and the layout work was carried out in Cadence.



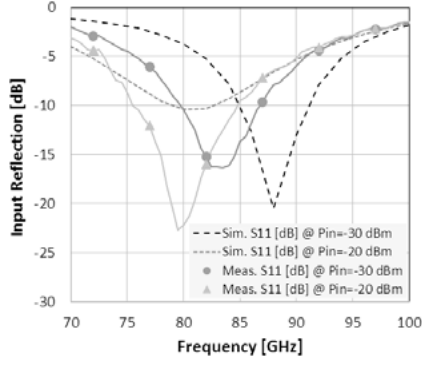


Figure 8.2. Measured and simulated  $|s_{11}|$  of a power detector made in a 130 nm SiGe BiCMOS technology. A first order LC based input matching network is used in this design.

The responsivity (computed as the slope of  $V_{out} - V_{ref}$  divided with  $P_{in}$  [15]), the input reflection  $|s_{11}|$  and  $P_{in}$  were measured using a Voltmeter, a network analyser connected to a probe station, a power meter, a power sensor and an impedance calibration substrate (the network analyser was used to generate the RF signal). The measurement set-up related losses due to the connecting cable and RF probe are estimated at 2 dB. Figure 8.2 shows measured and simulated input reflection of the detector when  $P_{in}$  is -30 dBm and -20 dBm, respectively. Measured  $|s_{11}|$  is below -10 dB at 80-86 GHz when  $P_{in} = -30$  dBm. A frequency shift in the measured  $|s_{11}|$  occurred when  $P_{in}$  was increased up to -20 dBm ( $|s_{11}| \leq -10$  dB at 76-84 GHz). Simulations reveal that the RF signal is high enough to modulate the transistor's bias point (DC current) which will influence the input impedance matching of the detector. This effect is visible in the detector  $|s_{11}|$  simulations (see Fig. 8.2). For a somewhat closer prediction of the input matching in-depth simulations based on a more accurate large-signal transistor model may be required.

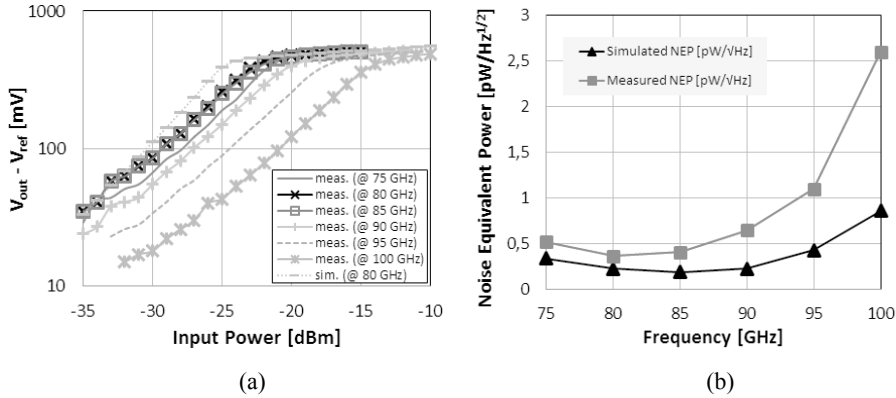


Figure 8.3. Measured and simulated output voltage vs input power (a) and NEP (b) of a power detector made in a 130 nm SiGe technology, respectively. An LC matching network is used.

Figure 8.3(a) shows the measured and simulated detector output voltages ( $V_{out} - V_{ref}$ ) versus input power (the simulated data is only shown at 80 GHz). The detector responsivity (which is computed based on the measured output voltages for a certain change in  $P_{in}$ ) is equal to 10-80 kV/W at 75-100 GHz. From these results, the detector NEP is estimated at 0.4-2.6 pW/Hz<sup>1/2</sup> at 75-100 GHz given a DC current of 20  $\mu$ A, a load resistance of 10 k $\Omega$  and using analytical expressions in [15] (see Fig. 8.3(b)). Compared with simulations, these NEP values are higher than anticipated, especially above 85 GHz. This difference may be explained by a lower responsivity than simulated, and the input impedance mismatch that occurs at higher frequencies in this design (see. Fig. 8.2). Thus, it should be possible to improve the detector sensitivity (NEP) over a wider frequency range by using a more wideband matching network. Such a wideband power detector design is shown in section 8.2.2.

### 8.2.2 Detector design based on a wideband matching network

Figure 8.4 shows a simplified circuit schematic and a chip photograph of a more wideband design of a W-band power detector SiGe RFIC, respectively (the circuit area is 570 x 320  $\mu$ m<sup>2</sup> incl. the RF and DC pads). This circuit was realised using the SG13G2 technology and the same circuit topology as in the previous power detector design except for the input matching network. To improve the bandwidth and increase the sensitivity of the detector, a higher order (T-type) matching network is used as shown in Fig. 8.4(a-b). The input matching network which consists of a series capacitor ( $C_s$ ), two on-chip series inductors ( $L_1$ ,  $L_2$ ) and a shunt capacitor ( $C_p$ ), was simulated and optimised in Sonnet (considering the via contacts, connecting lines and mutual coupling effects). The circuit simulations of the power detector were done in ADS based on the foundry process design-kit (and the EM simulated parts) and the layout was done in Cadence. Further design details incl. DC biasing component values used in this design can be found in **Paper VI**.

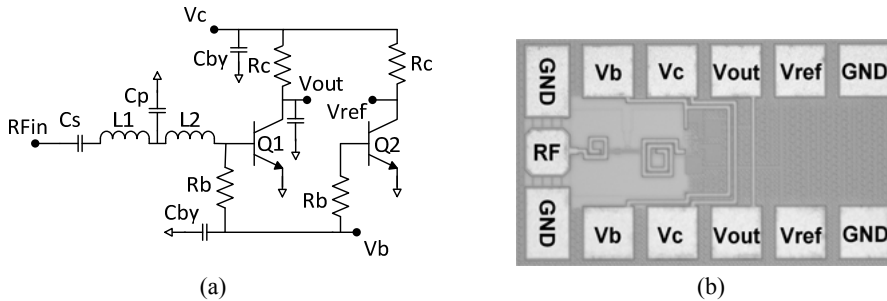


Figure 8.4. Circuit schematic (a), and photograph (b) of a W-band detector made in a 130 nm SiGe technology. Two inductors and two series/shunt caps are used in the matching network.

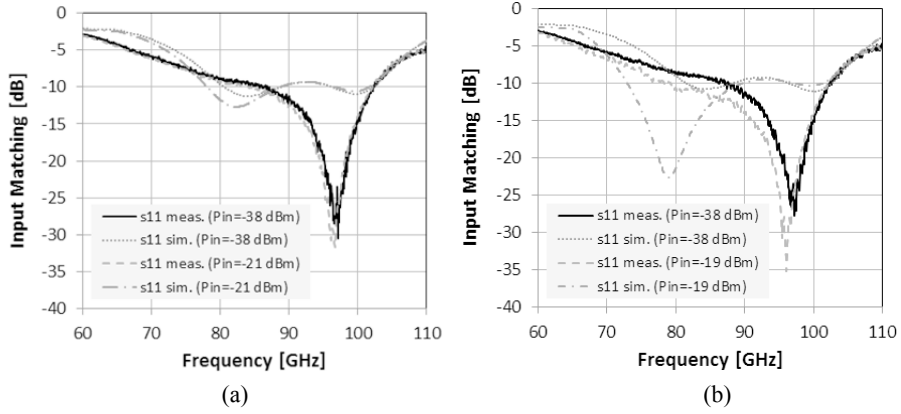


Figure 8.5. Measured and simulated  $|s_{11}|$  of a power detector made in a 130 nm SiGe process: (a)  $V_c=1.3$  V,  $I_c=123$   $\mu$ A ( $P_{in} = -38$  dBm and  $-21$  dBm, respectively), (b)  $V_c=0.8$  V,  $I_c=70$   $\mu$ A ( $P_{in} = -38$  dBm and  $-19$  dBm, respectively). A T-type matching network is used in this design.

The detector responsivity (computed as the ratio of  $V_{out}-V_{ref}$  and a certain change in  $P_{in}$ ), the input reflection and  $P_{in}$  were measured using the same measurement set-up which was used to measure the previous detector circuit. Figure 8.5(a) shows the measured and simulated  $|s_{11}|$  of the fabricated power detector circuit when  $V_c=1.3$  V,  $I_c=123$   $\mu$ A ( $P_{in}=-38$  dBm and  $-21$  dBm). The measurement results show that when the RF signal is high enough to modulate the Q1 transistor's bias point (DC current) it will influence the input impedance matching of the detector (the measured  $|s_{11}|$  -10 dB bandwidth changes from 87-102 GHz to 84-102 GHz when  $P_{in}$  is increased from -38 dBm to -21 dBm). Figure 8.5(b) shows that the measured  $|s_{11}|$  is below -10 dB at 79-102 GHz (in a 23 GHz frequency band) when  $V_c=0.8$  V,  $I_c=70$   $\mu$ A ( $P_{in}=-19$  dBm). The discrepancies between the measurements and simulations could be due to a limited EM modelling accuracy of the passive parts and the calibration used during the measurements.

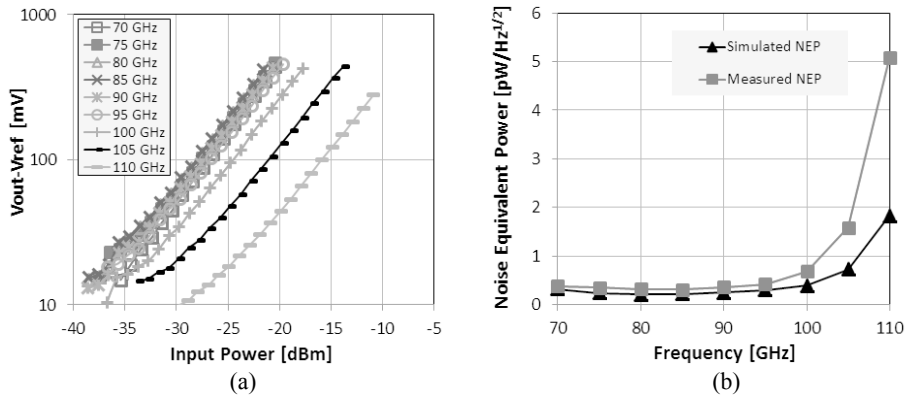


Figure 8.6. Measured output voltage vs input power (a) and measured and simulated NEP (b) of a detector made in a 130 nm SiGe process. A T-type match network is used in this design.

Figure 8.6(a) shows the measured output voltage ( $V_{\text{out}} - V_{\text{ref}}$ ) as function of swept input power level ( $P_{\text{in}}$ ) at 70-110 GHz ( $V_c = 1.3$  V,  $I_c = 123$   $\mu$ A). The simulated output voltage (not shown here) increases until saturation occurs when  $P_{\text{in}}$  is in the range of -20 dBm to -10 dBm. For a given  $P_{\text{in}}$  and frequency the measured  $V_{\text{out}} - V_{\text{ref}}$  is lower than simulated and a certain output voltage occurred for some dBs higher input power level. This saturating effect is not noticeable in the measured data and a reason that somewhat higher input power levels were not used in the measurements was since it would be beyond the interesting (useful) operating power range and also to reduce the risk of damaging the detector.

The detector responsivity was derived from the measured  $V_{\text{out}} - V_{\text{ref}}$  for a certain change in  $P_{\text{in}}$  and it is equal to 10-60 kV/W at 70-105 GHz. Based on these measured data and using analytical expressions in [15] the detector NEP is estimated at 0.3-0.7 pW/Hz<sup>1/2</sup> at 70-100 GHz given a DC current of 60  $\mu$ A and a load resistance of 4 k $\Omega$  (see Fig. 8.6(b)). The discrepancy found between measured and simulated NEP above 100 GHz may be explained by the lower responsivity than simulated, i.e. lower output voltage level for a given input power level (further details can be found in **Paper VI**).

### 8.3 Summary and Discussion

Table 8.1 compares the results of the two SiGe W-band power detector RFICs with some state-of-the-art detector circuits made in III-V and silicon based technologies. Compared with two power detectors realised in more costly InP based technologies [18], [19] the SiGe detectors presented in this thesis achieve peak responsivity values which are 3-20 times higher and a similar NEP. Furthermore, the input matching was not specified for the unmatched and matched power detectors in [18], [19]. The more wideband SiGe detector design shown in section 8.2.2 (**Paper VI**) reports the widest input matching bandwidth ( $|S_{11}| < -10$  dB at 79-102 GHz) among silicon W-band detectors and similar or improved sensitivity figure-of-merits (lower NEP).

The SiGe detector design in [101] reported higher peak responsivity and NEP values and the measured  $|S_{11}|$  varied between -6 dB to -14 dB at 75-110 GHz (the simulated  $|S_{11}|$  was below -10 dB at 89-102 GHz). For the SiGe detector in [15] the input matching was better than -10 dB at 88-100 GHz (the highest/lowest responsivity/NEP values were 11 kV/W and 5 pW/Hz<sup>1/2</sup>). The SiGe detector in [66] reported  $|S_{11}| \leq -10$  dB in a 20 GHz frequency band (at 84-104 GHz) together with inferior sensitivity results in terms of a lower responsivity and a higher NEP.

The presented results are in line with the target requirements in terms of a low detector NEP (0.3-0.4 pW/Hz<sup>1/2</sup> at 70-95 GHz). Such performances demonstrate extended possibilities of using SiGe detectors in single-chip

receivers as lower cost alternatives to more costly III-V based multi-chip radiometer modules for RF sensing applications such as passive imaging.

Table 8.1. Performance comparison of W-band power detector circuit designs realised in different technologies.

Reference	Technology	BW <sub>-10 dB</sub> (GHz)	Responsivity (kV/W)	NEP (pW/Hz <sup>1/2</sup> )
[18]	InP	N/A	22	0.4
[19]	InP	N/A	4	0.24
[15]	180 nm SiGe	88-100	11	5
[101]	180 nm SiGe	89-102 (sim.)	91	0.5
[66]	250 nm SiGe	84-104	5	1
<b>This work</b> (narrow-band)	<b>130 nm SiGe</b>	<b>76-84</b>	<b>80</b>	<b>0.4</b>
<b>This work</b> (wideband)	<b>130 nm SiGe</b>	<b>79-102</b>	<b>60</b>	<b>0.3</b>

## 9. Wideband SiGe IF Amplifier and IF Section for W-Band Direct-Conversion Radiometers

This chapter presents two novel differential wideband RFIC designs (a high-gain IF amplifier and a broadband single-chip IF-section) for a W-band SoC direct-conversion radiometer front-end. The designs were made in IHP's 0.13  $\mu\text{m}$  SiGe BiCMOs process (SG13G2) technology. The measured differential SiGe IF amplifier results have shown state-of-the-art performances in terms of achieving a high gain and low return losses over a wide bandwidth. Furthermore, the experimental results of a SiGe wideband IF section show the feasibility of using this IF amplifier, followed by a broadband power detector, in high-performance SoC W-band heterodyne radiometers.

The design, simulation and the layout work of the SiGe IF amplifier were made by the author of this thesis. The differential IF detector circuit design was made by the co-author Rolf Jonsson. Further details of these works are presented in **Papers VII-VIII**.

### 9.1 Differential IF Amplifier and IF Section

#### *9.1.1 Motivation and Background*

The millimetre-wave frequency range is attracting considerable interest for developing high resolution radar and imaging systems based on low-cost silicon technologies. W-band radiometers have been realised using III-V based multi-chip receiver modules with high sensitivities for such applications [17]. To increase the integration level and reduce the cost some RFIC W-band receivers made in 65 nm CMOS and 0.18  $\mu\text{m}$  SiGe BiCMOS technologies were recently presented [4], [15], [29]. Some W-band LNAs made in 90/130 nm SiGe processes reported both a high gain and also lower noise figure (NF) in the range of 3-4 dB, thus approaching the RF performances of some III-V W-band LNAs [21], [22]. For video rate real-time imaging an integration time up to a few milliseconds is typically required together with an NETD  $< 0.5$  K [17]. Such characteristics impose stringent requirements on the radiometer front-ends in terms of low noise, high pre-detection gain and wide bandwidth.

Some silicon W-band direct-detection and direct-conversion receivers reported an NETD of 0.5-1 K with a 30 ms integration time and NF close to 10 dB [4], [15], [29]. A main benefit by using a heterodyne architecture instead of a direct-detection receiver is that a higher receiver gain and sensitivity more easily can be obtained if a high-gain IF amplifier is used after the mixer and the LNA/detector gain/sensitivity requirements can be then relaxed. Relatively few results have been presented with respect to silicon based wideband IF amplifier and power detector circuits for System-on-Chip (SoC) W-band direct-conversion radiometers [4], [29].

## 9.2 Differential Wideband IF Amplifier

### 9.2.1 Circuit Design and Results

Figures 9.1 and 9.2 show the circuit schematic and a chip photograph of the proposed wideband differential IF amplifier SiGe RFIC design, respectively (the circuit area is  $678 \times 405 \mu\text{m}^2$  incl. the RF and DC pads). The differential two-stage IF amplifier was fabricated in IHP's  $0.13 \mu\text{m}$  BiCMOS process SG13G2 and the design is partly based on the single-ended  $0.25 \mu\text{m}$  SiGe three-stage wideband LNA circuit presented in **Paper IV** (see Chapter 7). The common emitter topology was used in each amplifier stage due to its design simplicity and expected broadband RF properties. In order to fulfill the target requirements, the two-stage amplifier was optimised to achieve a high gain (15-20 dB), linearity (input P1dB > -30 dBm), wideband matching and low noise figure (5-10 dB) over the specified bandwidth (25 GHz) by selecting the appropriate DC bias points and suitable number of emitter fingers in each stage. The base DC bias voltages ( $V_{b1}$ ,  $V_{b2}$ ) are set by using voltage dividers ( $R_1$ ,  $R_2$ ,  $R_3$ ,  $R_4$ ) and current mirrors while the collector DC voltages ( $V_{c1}$ ,  $V_{c2}$ ) are applied via the bias resistors ( $R_{c1}$ ,  $R_{c2}$ ).

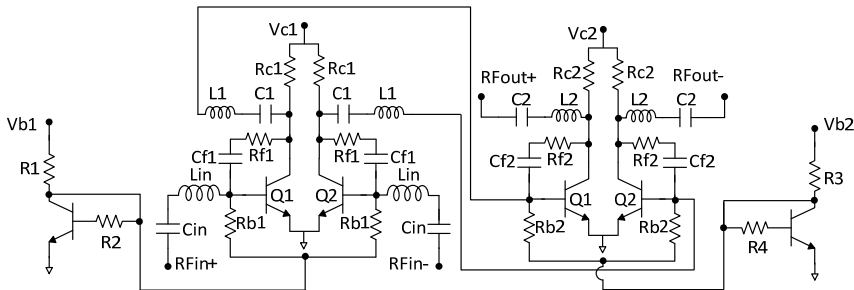


Figure 9.1. Schematic of a high-gain wideband differential IF amplifier circuit design made in a 130 nm SiGe BiCMOS process technology.

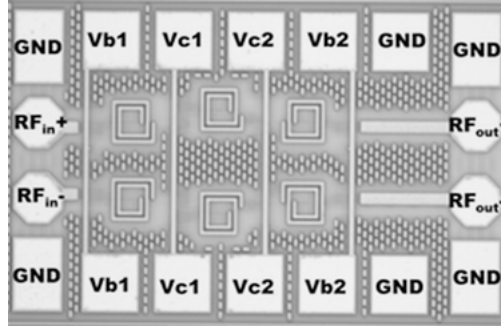


Figure 9.2. Micrograph of a high-gain wideband differential IF amplifier RFIC made in a 130 nm SiGe BiCMOS process technology.

Figure 9.3 shows the simulated small-signal gain ( $|s_{21}|$ ) and noise figure for a SiGe HBT with a different number of emitter fingers ( $n$ ) and emitter area  $A_E = n \times 0.063 \mu\text{m}^2$ . Furthermore, the peak values of  $f_T$  are specified in the foundry process design manual to occur at a collector current ( $I_C$ ) of 7–8 mA and 15 mA when  $n=4$  and  $n=8$ , respectively. Compared with a transistor having  $n=4$ ,  $n=8$  resulted in 1–6 dB higher simulated gain and 1 dB lower simulated noise figure up to 35 GHz, respectively. A differential two-stage amplifier with  $n=8$  in each stage showed the highest simulated gain (20–25 dB at 5–32 GHz) and lowest simulated noise figure (3–5 dB at 2–38 GHz). However, this design obtained a somewhat less wide matching (with input and output return losses below  $-10$  dB at 8–26 GHz) and was also closer to instability. Selecting  $n=4$  in the first stage and  $n=8$  in the second stage resulted, on the other hand, in the best possible trade-off between providing both circuit stability with a reasonably high gain (20–23 dB at 5–31 GHz), low noise figure (5–6 dB at 2–40 GHz) and a wideband matching ( $\leq -10$  dB at 6–32 GHz) for the designed IF amplifier.

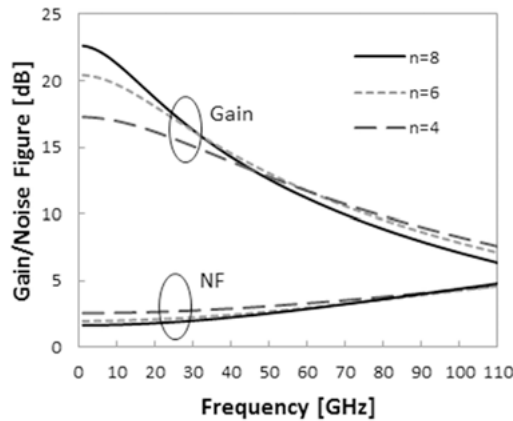


Figure 9.3. Simulated gain and noise figure for a SiGe HBT transistor with a different number of emitter fingers.



Feedback resistors ( $R_{f1}$ ,  $R_{f2}$ ) and DC blocking capacitors ( $C_{f1}$ ,  $C_{f2}$ ) are used between the collector and base terminals in each stage to ensure that the amplifier is unconditionally stable. The input and output matching networks are realised using some on-chip inductors ( $L_{in}$ ,  $L_{out}$ ) and capacitors ( $C_{in}$ ,  $C_{out}$ ). The on-chip inductors are made of a 3  $\mu\text{m}$  thick (top) metal layer and were simulated using the EM simulation tool Sonnet. To enhance the peak gain and bandwidth of the SiGe IF amplifier circuit the inter-stage matching network was designed using a series capacitor ( $C_I$ ) and an inductor ( $L_I$ ). The component values used in this design can be found in **Paper VII**.

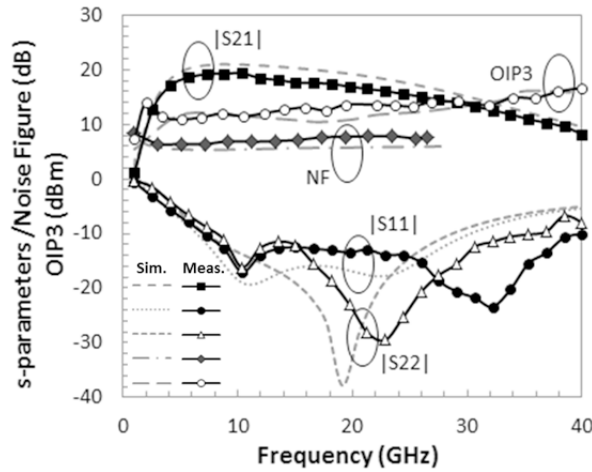


Figure 9.4. Measured and simulated results of a 130 nm SiGe BiCMOS high-gain wideband differential IF amplifier.

The circuit layout and simulations of the IF amplifier were done using Cadence (incl. post-layout parasitic extraction of resistance, capacitance, inductance and mutual inductance due to the on-chip interconnecting lines). The layout versus schematic (LVS) based parasitic extraction was made separately for each amplifier stage since all the on-chip inductors were made as full-custom designs. Finally, the active and passive parts were combined in Cadence incl. the EM simulated s-parameter files of the on-chip inductors.

Five chips with the fabricated IF amplifier were characterised using a network analyser connected to probe station and a differential impedance standard calibration substrate. Furthermore, the use of on-wafer calibration standards made it possible to also exclude the effects of the RF pads in the s-parameter measurements by using an open-short deembedding technique. The tested circuits showed quite similar results, thus indicating relatively small process variations. The differential IF amplifier was measured at the two DC bias points that resulted in the highest gain ( $|s_{21}|$ ) and lowest noise figure, respectively (see Table 9.1). Figure 9.4 shows measured and simulated IF amplifier results without any deembedding and for the bias point that

resulted in the highest gain ( $V_{c1,2}=3.7$  V,  $V_{b1,2}=3.5$  V,  $I_1=20$  mA and  $I_2=24$  mA where  $I_1$  and  $I_2$  are the DC currents in each stage). The IF amplifier has a measured gain of 10-19.5 dB at 2-37 GHz ( $\geq 15$  dB at 3-26 GHz) with input/output matching better than -10 dB at 7-40 GHz and 8-35 GHz, respectively. The measured NF and OIP3 are equal to 6-8 dB and 7-17 dBm at 1-26.5 GHz and 1-40 GHz, respectively. Figure 9.5 shows the measured IF-amplifier s-parameters after deembedding of the RF pads. The measured IF amplifier gain is in this case equal to 15-19.6 dB at 3-28 GHz which fulfills the target gain requirement over a 25 GHz bandwidth ( $|s_{11}| \leq -10$  dB at 6-37 GHz).

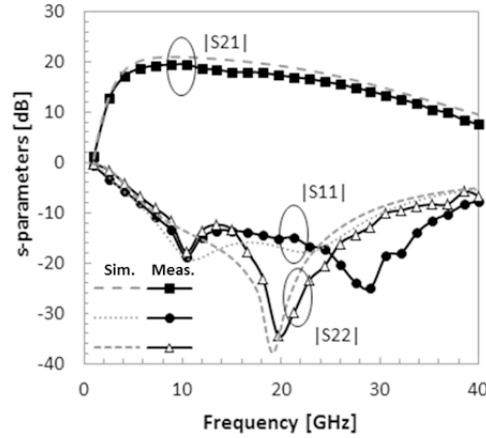


Figure 9.5. Measured and simulated s-parameters of a 130 nm SiGe BiCMOS high-gain wideband differential IF amplifier (after the RF pads losses have been de-embedded).

### 9.2.2 Summary and Discussion

Table 9.1 compares the results of the presented SiGe BiCMOS differential IF amplifier with some state-of-the-art amplifier designs made in different technologies. To evaluate the performance of the SiGe wideband amplifier, a Figure of Merit (FOM) is used for comparison purposes:

$$FOM = \frac{Gain(max) \times Freq(GHz)}{NF(min) \times Pdc(mW)} \quad (9.1)$$

The SiGe IF amplifier shows better or similar performance as compared to other published wideband amplifier circuits. This work results in a higher peak gain (with a reasonably low NF), more wideband input/output matching and dissipates less DC power than a differential amplifier made in a more expensive GaAs HBT technology [102]. Relatively few results have been reported on SiGe BiCMOS high-gain (low noise) amplifiers with a wideband matching within the DC-40 GHz range. The SiGe differential amplifier in [103] has a more wideband gain but higher NF (20 dB sim.) and consumes more DC power. The results of the proposed SiGe differential IF amplifier

compares favorably also with some previously reported single-ended silicon based amplifier [99], [104]–[108] in terms of achieving a higher/similar peak gain or more wideband input/output matching. The noise figure is 1-2 dB higher than for those designs but this is less critical for the targeted application as the IF amplifier will be preceded by a high-gain LNA and active mixer in the direct-conversion receiver chain. As shown in Table 9.1, the de-embedded results of the SiGe differential IF amplifier design fulfill the specified target requirements of 15-20 dB of gain over a 25 GHz bandwidth.

Table 9.1. Performance comparison of wideband amplifiers realised in different technologies.

Ref. / Topology	Tech. $f_i/f_{\max}$ (GHz)	Freq. (GHz)	Gain (dB)	$ S_{11} $ (dB)	NF (dB)	OIP3 (dBm)	$P_{dc}$ (mW)	FoM (GHz/ mW)
[102] Diff.	GaAs 175/370	0-48	10-15	$\leq -10$ 0-26 GHz	N/A	N/A	250	N/A
[103] Diff.	180 nm SiGe HBT 200/275	1-84	20	$\leq -10$ 1-69 GHz	$\geq 20$ sim.	N/A	990	0.11
[104] SE	180nm SiGe HBT 120/-	3-20	14-21	$\leq -10$ 5-20 GHz	4.2-5.2 8-18 GHz	9.2	116	7.5
[105] SE	180nm SiGe HBT 120/100	0.5-22	14-15	$\leq -9$ 1-50 GHz	4.5-5.5 1-18 GHz	16.5*	72	3.4
[99] SE	130 nm SiGe HBT 200/-	3-26	9	$\leq -10$ 3-30 GHz	3.9-6.4 2-24 GHz	14.8*	33	2.3
[106] SE	120 nm SOI CMOS 196/230	5-90	9-12	$\leq -7$ 5-90 GHz	4.8-6.2 10-18 GHz	15.5	210	2.1
[107] SE	65nm SOI CMOS 300/-	2-27	10-18	$\leq -10$ 3-27 GHz	4.8-8.0 2-26 GHz	19.4*	55	9.5
[108] SE	65nm CMOS 200/-	2-39	10-11.5	$\leq -8$	4.5-7.0 2-47 GHz	5.8*	26	7.1
<b>This work Diff.</b>	<b>130 nm SiGe HBT 300/500</b>	<b>2-37</b>	<b>10-19.5</b>	<b><math>\leq -10</math> 7-40 GHz</b>	<b>6.3-8.0 2-26 GHz</b>	<b>7-17</b>	<b>122</b>	<b>6.0</b>
		<b>2-36</b>	<b>10-18.7</b>	<b><math>\leq -10</math> 7-40 GHz</b>	<b>5.8-7.8 2-26 GHz</b>	<b>8-13</b>	<b>70</b>	<b>9.5</b>

Diff. (differential), SE (Single-ended), \*estimated based on the given IIP3 data

De-embedded results of the fabricated differential IF amplifier for (a) high-gain case:  $|S_{21}|=10$ -19.6 dB and  $|S_{11}|\leq -10$  dB at 2-36 GHz and 6-37 GHz, respectively and (b) low-NF case:  $|S_{21}|=10$ -18.9 dB and  $|S_{11}|\leq -10$  dB at 2-35 GHz and 7-37 GHz, respectively.

## 9.3 Differential Broadband IF Section

### 9.3.1 Circuit Design and Results

The SiGe high-gain wideband differential amplifier presented in section 9.2 (**Paper VII**) was integrated on the same chip as a broadband power detector (designed by co-author Rolf Jonsson). On-chip interconnecting lines used between the two circuits made it possible to measure the combined single-chip IF section as a part of a W-band SoC radiometer down-converter chain. Each circuit was also tested individually after dicing chips in separate parts. Figures 9.6(a-b) depict simplified circuit schematics of the two designs (only the first amplifier stage is shown here and the active biasing circuitry is omitted). Fig. 9.7 shows a chip photo of the broadband IF section made in IHP's 0.13  $\mu\text{m}$  BiCMOS process SG13G2 (the chip area is  $500 \times 1200 \mu\text{m}^2$  with the RF and DC pads). Two pairs of transistors Q1, Q2 and Q3, Q4 are used in the power detector design to achieve temperature compensation [15]. The RF input signals  $\text{RF}_{\text{in}+}$  and  $\text{RF}_{\text{in}-}$  are applied to the transistors Q1 and Q2, resulting in the output voltages  $V_{\text{out}}$  and  $V_{\text{ref}}$ . To obtain the required wideband response, resistive input matching is employed here at the expense of a reduced detector sensitivity, responsivity and higher NEP. The DC voltages ( $V_c$ ,  $V_b$ ) are applied to forward bias the base-emitter junction of each bipolar transistor via the bias resistors ( $R_b$ ,  $R_c$ ).

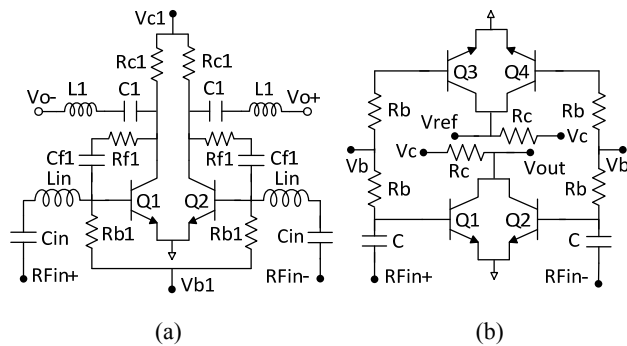


Figure 9.6. Simplified circuit schematics of differential broadband IF amplifier and power detector designs (a-b) made in a 130 nm SiGe BiCMOS process.

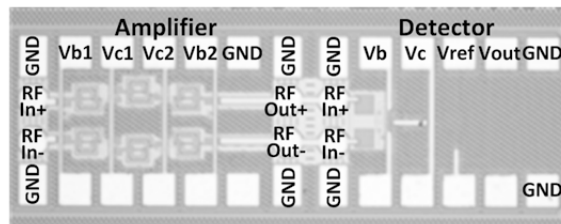


Figure 9.7. Photograph of a broadband IF section made in a 130 nm SiGe BiCMOS process.

The combined broadband IF section (amplifier and power detector) was simulated in ADS using the developed circuit models of each functional block. The detector voltages  $V_{out}$ ,  $V_{ref}$ , s-parameters, and RF input power  $P_{in}$  were measured using a Volt meter, a four-port network analyser connected to a probe station, a calibration module, a power sensor and a power meter. The network analyser was used to generate the RF input signal, and the s-parameters were measured differentially using GSSG probes with a 100  $\mu\text{m}$  pitch and an impedance standard calibration substrate.

As shown in Fig. 9.8(a), the measured input reflection of the detector is below -9 dB at 3-36 GHz while for the IF section  $|s_{11}| \leq -10$  dB at 7-40 GHz (the amplifier and detector DC bias voltages and currents are:  $V_{c1,2}=3.7$  V,  $I_1=18$  mA,  $I_2=23$  mA and  $V_c=V_b=0.8$  V,  $I_c=45$   $\mu\text{A}$ ). Hence, the IF section  $|s_{11}|$  is largely determined by the IF amplifier input matching (see Fig. 9.4). Figure 9.8(b) shows measured and simulated responsivity of the detector and IF section, respectively (computed from the ratio of  $V_{out} - V_{ref}$  and a change in  $P_{in}$ ). The somewhat lower measured responsivity of the IF section than simulated is largely due to a lower measured amplifier gain (see Fig. 9.4). The IF section and detector achieve responsivity values of 10-82 kV/W and 1 kV/W at 5-35 GHz, respectively (the difference is in line with the 10-19 dB of measured amplifier gain). Further details can be found in **Paper VIII**.

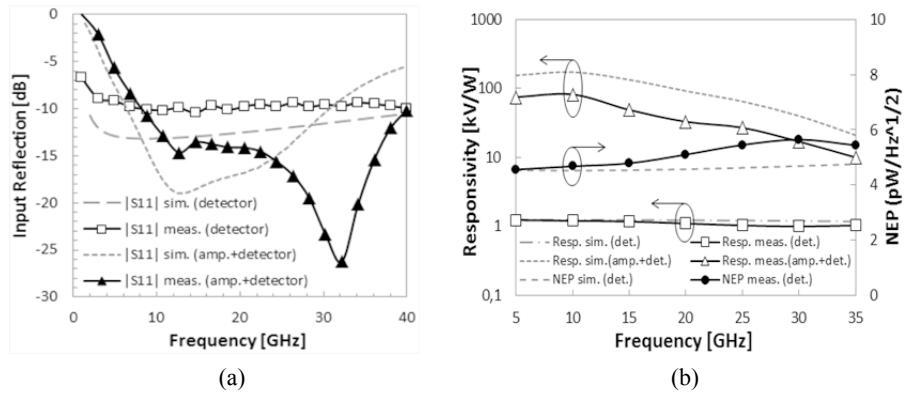


Figure 9.8. Measured and simulated input reflection and responsivity (a-b) of the broadband power detector and IF section circuit designs, respectively. The measured and simulated detector NEP results are also represented in Fig. 9.8(b).

### 9.3.2 Summary and Discussion

Tables 9.2-9.3 compare the results of the presented differential IF amplifier and power detector SiGe RFIC designs with some state-of-the-art wideband amplifiers and detectors made in different silicon technologies, respectively. Here, the amplifier FoM is calculated as follows [109]:

$$FoM = \frac{Gain(max) \times IIP3(mW) \times Freq.(GHz)}{(NF-1) \times Pdc(mW)} \quad (9.2)$$

Relatively few results have been presented with respect to silicon based wideband IF amplifier and power detector circuits for SoC W-band direct-conversion radiometers [4], [29]. The SiGe differential IF amplifier shown in this thesis results in an improved (more wideband) matching and a 10 dB higher OIP3 when compared with a recent single-ended SiGe LNA [110]. The 5-35 GHz IF section with its sub parts compare favourably with some 1-20 GHz/1-10 GHz IF amplifier and power detector RFIC designs [4], [29] in terms of improved sensitivity (lower NEP) over an extended frequency range and also a much wider IF amplifier bandwidth. Their broadband properties over significantly wider bandwidths than those circuits make them viable candidates for SoC W-band down-conversion receivers with a larger pre-detection bandwidth and improved sensitivity. The experimental results successfully demonstrate the feasibility of the SiGe 5-35 GHz IF section for high-performance SoC W-band radiometers using a more wideband heterodyne receiver architecture.

Table 9.2. Performance comparison of silicon based wideband amplifiers.

Ref. (Topology)	[103] (Differential)	[110] (Single-ended)	<b>This Work Differential</b>
Technology	180 nm SiGe	180 nm SiGe	<b>130 nm SiGe</b>
Freq. (GHz)	1-84	1-40	<b>2-37</b>
S <sub>11</sub>   (dB)	≤ -10 (1-69 GHz)	≤ -7 (9-40 GHz)	<b>≤ -10 (7-40 GHz)</b>
Gain (dB)	20	10-27	<b>10-19.5</b>
NF (dB)	20 (sim.)	5.2	<b>6.3</b>
OIP3 (dBm)	7	-3 to 6 (est.)	<b>7-17</b>
FoM	0.004	3.2	<b>1.4</b>

Table 9.3. Performance comparison of silicon based wideband power detectors.

Ref. (Topology)	[29] (Differential)	[15] (Single-ended)	<b>This Work (Differential)</b>
Technology	65 nm CMOS	180 nm SiGe	<b>130 nm SiGe</b>
Freq. (GHz)	1-10	75-110	<b>5-35</b>
S <sub>11</sub>   (dB)	-	≤ -10 (88-99)	<b>≤ -9 (3-36 GHz)</b>
Respons. (kV/W)	2-6	4-11	<b>1</b>
NEP (pW/Hz <sup>1/2</sup> )	8-31	5-13	<b>4.5-5.8</b>

## 10. Conclusions and Future Work

### 10.1 Conclusions

This thesis has presented studies and solutions to improve the sensitivity of mm-wave system-on-chip (SoC) radiometer front-ends. More specifically, some novel reconfigurable and wideband MMIC/RFIC designs have been realised in the 30-110 GHz range using GaAs and SiGe BiCMOS foundry processes, respectively. Furthermore, the monolithic integration of low loss and high isolation mm-wave RF-MEMS Dicke switches and wideband LNAs in such IC technologies has been demonstrated for the first time. GaAs and SiGe MEMS (Dicke/SPDT) switch networks were designed and measured up to W-band (the best one of those switches reached 1 dB and 19 dB of minimum losses and maximum isolation at 70-96 GHz, respectively).

In this thesis, two different receiver topologies were investigated based on direct-detection and direct-conversion architectures for W-band (passive imaging) radiometer front-ends. Some novel wideband IF amplifier and power detector RFIC designs have been realised in a 0.13  $\mu\text{m}$  SiGe process. An optimised SiGe W-band power detector design achieved the widest input matching bandwidth ( $|S_{11}| \leq -10$  dB at 79-102 GHz) among silicon based W-band detector circuits with similar or improved sensitivity figure-of-merits. The results of a SiGe differential wideband high-gain IF amplifier design and its on-chip combination with a power detector (broadband IF section) compare favourably with earlier reported silicon wideband amplifiers and power detectors in terms of improved linearity, sensitivity and wideband matching.

A W-band MEMS Dicke switch network fabricated in a GaAs MMIC process (**Paper I**), has a measured minimum loss of 1.1-1.6 dB and 10-19 dB of isolation at 70-96 GHz. The in-band losses are similar to the results of a W-band SPDT switch design fabricated using an in-house developed PIN diode technology [74] which is not commonly available in many GaAs foundry processes such as the OMMIC process. MEMS switches obtain a higher linearity and consume virtually no DC power which makes them attractive candidates for high dynamic range and low-power applications.

A novel W-band MEMS Dicke switched LNA MMIC design (**Paper II**) achieved a gain of 16 dB with 11 dB of isolation and 5 dB of noise figure. This switched LNA design is believed to be a first-time realisation of a

MEMS Dicke switch and a W-band LNA made in a 70 nm mHEMT process. Compared with an earlier W-band switched LNA MMIC [88], this work results in 9 dB higher gain and 1 dB lower noise figure. Furthermore, the simulated results of an optimised MEMS GaAs LNA design fulfill the target requirements of a W-band receiver front-end.

For bench-marking purposes, some 40/60/80 GHz MEMS SPDT switches were fabricated in a 0.25  $\mu\text{m}$  SiGe BiCMOS process from IHP (**Paper III**). This SiGe MEMS switch technology was still in its early development phase at that time which partly may explain why the measured switch losses were some dBs higher than anticipated (incl. roughly 1 dB of RF pad losses). On-wafer measured results of more than 300 of such SPDT switches further indicate a high fabrication yield and process repeatability of the SiGe MEMS RFICs.

A wideband LNA design fabricated in a 0.25  $\mu\text{m}$  SiGe BiCMOS process reached a gain of 10-20 dB at 2-33 GHz together with input return losses better than -10 dB at 24-39 GHz (**Paper IV**). Compared with some earlier reported SiGe LNAs this work achieved both a high gain over a much wider bandwidth and a broadband input matching. The simulated results of a 30 GHz SiGe RF-MEMS switched LNA RFIC design is close to the target specification. Due to missing via contacts between the Dicke switch and LNA ground planes, the measured gain of the fabricated switched LNA was much lower than anticipated in the ON state. Despite of this, the switching function of the MEMS Dicke switch in the switched LNA was validated.

Two 0.13  $\mu\text{m}$  SiGe BiCMOS power detector designs for a W-band direct-detection radiometer front-end obtained a lower NEP in comparison with earlier reported silicon based W-band detectors and are competitive with InP W-band power detectors in terms of a higher responsivity and similar NEP (**Papers V-VI**). The presented results are in line with the target requirements of a W-band receiver with a detector  $\text{NEP}=0.3\text{-}0.4\text{ pW/Hz}^{1/2}$  at 70-95 GHz. Such performances demonstrate extended possibilities of using SiGe detectors in SoC receivers as lower cost alternatives to more costly III-V based multi-chip radiometers for RF sensing applications such as passive imaging.

The 0.13  $\mu\text{m}$  SiGe high-gain differential IF amplifier design presented in this thesis (**Paper VII**) results in an improved (more wideband) matching and a 10 dB higher OIP3 when compared with a recent single-ended SiGe LNA [110]. This IF amplifier has reached a gain of 15-20 dB over a 25 GHz bandwidth which then fulfills the target requirements when used in a W-band SoC down-conversion (heterodyne) receiver architecture.

A SiGe 5-35 GHz IF section with its sub parts compare favourably with some earlier reported IF amplifier/power detector RFIC designs [4], [29] in terms of an improved sensitivity (lower NEP) over an extended frequency range and also a much wider IF amplifier bandwidth (**Paper VIII**). Their broadband RF properties over significantly wider bandwidths than those



circuits make them suitable for SoC W-band down-conversion receivers with a larger pre-detection bandwidth and improved sensitivity. The experimental results successfully demonstrate the feasibility of the SiGe 5-35 GHz IF section for high-performance SoC W-band radiometers using a more wide-band heterodyne receiver architecture.

To conclude, the results of the reconfigurable and wideband MMIC and RFIC designs presented in this thesis are expected to pave the way for more highly integrated (single-chip) mm-wave switched radiometer front-ends with enhanced functionalities (wider bandwidths and higher sensitivities) and improved cost-effectiveness (system-on-chip solutions). Furthermore, these attractive features are perceived as key factors for a wider deployment of such mm-wave receiver modules for emerging applications including wireless communication and short range (passive imaging) security sensors.

## 10.2 Future Work

Some possibilities for future improvements related to the reconfigurable and wideband MMIC/RFIC designs presented in this thesis are given below.

The more compact micro-strip design of a W-band GaAs RF-MEMS Dicke switch network shown in Fig. 4.3(a-b) (**Paper I**) could be fabricated in a future MMIC run. This design has a simulated transmission loss of 0.5-1.3 dB and 15-29 dB of isolation at 76-96 GHz, respectively. The losses can be even further reduced if mitered bends are used in the micro-strip lines that connect the two MEMS switches and the via-hole. A W-band switched LNA design based on this micro-strip MEMS Dicke switch and a COTS GaAs LNA MMIC (**Paper II**) may also be considered for fabrication. Furthermore, it could be combined with a power detector on the same GaAs chip to enable a high performance/sensitivity W-band switched single-chip receiver.

The RF properties of the characterised mm-wave SiGe MEMS switches (**Paper III**) should be possible to improve in future re-designs using highly accurate foundry (EM) MEMS switch models and micro-strip designs [53]. The layout mistake (missing metal via contacts) in the fabricated 30 GHz SiGe MEMS LNA (**Paper IV**) can be easily rectified in a future re-design. Such an RF-MEMS LNA design may also be scaled to higher frequencies (e.g. at W-band or beyond) in IHP's 0.13  $\mu\text{m}$  SiGe BiCMOS technology.

The presented SiGe W-band power detectors and IF amplifier/detector designs (**Papers V-VIII**) have been used in some fabricated direct-detection and direct-conversion single-chip receivers. Those SiGe W-band front-ends have not yet been characterised and consequently the experimental results will be reported at a later stage.

## 11. Summary in Swedish

Denna avhandling behandlar monolitiska kretskonstruktioner av rekonfigurerbara och bredbandiga mottagarkomponenter för högintegrerade radiometrar inom mm-vågsområdet. Mer högintegrerade mm-vågsmoduler skulle kunna användas för traditionella radiometerapplikationer (t.ex. rymd) samt inom trådlös kommunikation och aktiva/passiva bildalstrande RF sensorer för korthållssäkerhetstillämpningar om sådana moduler kan uppnå önskad prestanda och även tillverkas billigare i större volymer. I denna avhandling berörs tre olika delområden inom mm-vågs högintegrerade (system-på-chip) radiometer front-ends.

RF-MEMS switchar tillverkade i två kommersiella halvledarprocesser har designats och karaktäriserats för 30-110 GHz bandet. En GaAs MEMS Dicke switch visar lovande prestanda inom bandet 70-96 GHz vilket gör den potentiellt lämplig för Dicke switchade radiometer front-ends. Två en-chips MEMS Dicke switchade lågbrusförstärkare har för första gången realiserats i SiGe och GaAs processer vid 30 GHz samt inom W-bandet (75-110 GHz).

I denna avhandling studeras två olika mottagararkitekturer med och utan nedblandning för en 94 GHz (passivt bildalstrande) radiometertillämpning. En optimerad effektdetektor tillverkad i en 0.13  $\mu\text{m}$  SiGe process uppvisar en bredare ingångsanpassning jämfört med andra kiselbaserade W-bands detektorer samt uppnår även en högre responsivitet (liknande NEP) än W-bands detektorer framtagna i mer avancerade och kostsamma InP processer.

En SiGe differentiell (IF) förstärkarkonstruktion med en uppmätt småsignalförstärkning på 10-20 dB inom frekvensbandet 2-37 GHz åstadkommer mer bredbandig impedansanpassning samt en tio gånger högre linearitet än en nyligen framtagen (single-ended) SiGe lågbrusförstärkare. IF förstärkaren integrerades på samma SiGe chip som en resistivt anpassad effektdetektor för att realisera en 5-35 GHz IF sektion. Den bredbandiga RF prestanda som dessa komponenter uppvisar gör dem speciellt lämpade för mottagare med nedblandning från W-band (till denna mellanfrekvens) vilket möjliggör en motsvarande systembandbredd med en högre mottagarförstärkning och därmed förbättrad känslighet för mottagarna. De experimentella resultaten demonstrerar framgångsrikt möjligheterna med en SiGe 5-35 GHz IF sektion för högintegrerade (system-på-chip) W-bands radiometrar med förbättrad RF prestanda baserat på en mer bredbandig heterodyn mottagararkitektur.

# Acknowledgements

**I would like to very humbly thank Allah Almighty, the most Compassionate and the most Merciful for giving me physical as well as mental strength, opportunity and resources to accomplish this research work.**

A long list of people to whom I wish to say thank you! Those are my family members, teachers, colleagues and friends. Here I would like to thank all those who are directly or indirectly related to this work:

- My Supervisor Dr. Robert Malmqvist, for his valuable guidance and support related to the circuit design, RF testing, collaborator contacts, scientific writing, and giving me the opportunity to perform measurements at Swedish Defence Research Agency (FOI).
- My co-supervisor Prof. Anders Rydberg at Uppsala University for giving me the opportunity to do research in European projects, his appreciated support, and providing me the additional fund during four years of my Ph.D. studies.
- Co-authors of the research papers Mr. Carl Samuelsson, Mr. Rolf Jons-son, and Mr. Andreas Gustafsson at FOI, Mr. Andreas Strodl, Dr. Vaclav Valenta and Prof. Hermann Schumacher at University of ULM, Dr. Mehmet Kaynak at IHP, Mr. Brice Grandchamp at OMMIC, Mr. Pekka Rantakari and Dr. Tauno Vähä-Hekkilä at VTT Technical Research Centre of Finland for their kind help, support and valuable discussions. Mr. Tomas Boman at FOI for the calculations of NETD and Mr. Stig Leijon for his help with the chip wire bonding and making the test fixtures.
- European Union for the funding and support of the FP7 ICT project NANOTEC.
- Prof. Jörgen Olsson at Uppsala University for providing the design kits.
- Ms. Marianne Asplund and Ms. Camilla Sandgren at Uppsala University for resolving the administrative issues.
- Prof. Göran Hansson and Ms. Kerstin Vestin for making my sitting arrangement possible at (IFM) Linköping University to carry out research work and especially Mr. Ulf Frykman for his technical support.

- Associate Prof. Jerzy Dabrowski at (ISY) Linköping University for his precious time and academic discussions. Research engineer Mr. Arta Alvandpour and Mr. Thomas Johansson for their computer and networking support.
- Special thanks to Dr. Qamar-ul-Wahab, Dr. Zakaullah Sheikh, Dr. Ahsan Ullah Kashif, Dr. Fahad Qazi, Dr. Hafiz Muhammad Sohail, Dr. Nadeem Afzal, Doctorand Muhammad Irfan Kazim, Doctorand Touqeer Pasha, Doctorand Asad Alam, Doctorand Syed Bilal, and Doctorand Fahim-ul-Haque for their intellectual support.
- Mamoon (late), Mami, Syed Hafeez Alam Naqvi, Dr. Ghazala Masooma Anjum, Waseem Akhter, Rakhshinda Jabeen, Muhammad Rafique-ur-Rahman, and Aqsa Bhabi for their encouragement and motivation.
- All my Abbas, Phuppies, Chachees, Khalas, cousins, nieces, and nephews for their sincere prayers.
- Thanks to the government of Pakistan, Higher Education Commission (HEC), and NED University of Engineering and Technology, Karachi for sending me to Sweden to carry out Ph.D. studies at Uppsala University, Sweden.
- Finally, my husband Muhammad Abul Hasan and my son Ammar Hasan for their love, affection, and compromising over their time.

*Shakila Bint Reyaz*  
*January 2015*

# Bibliography

- [1] A. Tomkins, R. A. Aroca, T. Yamamoto, S. T. Nicolson, Y. Doi, and S. P. Voinigescu, "A Zero-IF 60 GHz 65 nm CMOS Transceiver With Direct BPSK Modulation Demonstrating up to 6 Gb/s Data Rates Over a 2 m Wireless Link," *IEEE Electron Device Lett.*, vol. 44, no. 8, pp. 2085–2099, 2009.
- [2] S. T. Nicolson, P. Chevalier, B. Sautreuil, and S. P. Voinigescu, "Single-Chip W-band SiGe HBT Transceivers and Receivers for Doppler Radar and Millimeter-Wave Imaging," *IEEE J. Solid-State Circuits*, vol. 43, no. 10, pp. 2206–2217, 2008.
- [3] V. Jain, F. Tzeng, L. Zhou, and P. Heydari, "A Single-Chip Dual-Band 22-29-GHz/77-81-GHz BiCMOS Transceiver for Automotive Radars," *IEEE J. Solid-State Circuits*, vol. 44, no. 12, pp. 3469–3485, 2009.
- [4] Z. Chen, C. Wang, H. Yao, and P. Heydari, "A BiCMOS W-Band 2×2 Focal-Plane Array With On-Chip Antenna," *IEEE J. Solid-State Circuits*, vol. 47, no. 10, pp. 1–17, 2012.
- [5] D. Dancila, R. Malmqvist, S. B. Reyaz, R. Augustine, C. Samuelsson, M. Kaynak, and A. Rydberg, "Wide Band On-Chip Slot Antenna with Back-Side Etched Trench for W-band Sensing Applications," in *Antennas and Propagation (EuCAP)*, 2013, pp. 1576–1579.
- [6] J. W. May and G. M. Rebeiz, "Design and Characterization of W-Band SiGe RFICs for Passive Millimeter-Wave Imaging," *IEEE Trans. Microw. Theory Tech*, vol. 58, no. 5, pp. 1420–1430, 2010.
- [7] L. Yujiri, S. Merit, and P. Moffa, "Passive Millimeter-Wave Imaging," *IEEE Microwave Magazine*, no. September, pp. 39–50, Sep-2003.
- [8] M. R. Fetterman, J. Grata, G. Jubic, W. L. Kiser, Jr., and A. Visnansky, "Simulation, acquisition and analysis of passive millimeter-wave images in remote sensing applications," *Opt. Express*, vol. 16, no. 25, pp. 20503–20515, Nov. 2008.
- [9] H. Essen, H. Fuchs, H. Manfred, S. Stanko, N. Denis, S. Erukulla, J. Huck, M. Schlechtweg, and A. Tessmann, "Concealed Weapon Detection with Active and Passive Millimeterwave Sensors , Two Approaches," in *German Microwave Conference (GeMiC)*, 2006, pp. 1–4.

- [10] H. Kim, S. Duffy, J. Herd, and C. Sodini, "SiGe IC- based mm-wave imager," in *IEEE International Symposium on Circuits and Systems*, 2007, pp. 1975–1978.
- [11] R. Zimmermann, T. Rose, T. W. Crowe, and T. W. Grein, "AN ALL-SOLID-STATE -1 THz- RADIOMETER FOR SPACE APPLICATIONS," in *6th Int. symposium on Space Terahertz Technology*, 1995, pp. 13–27.
- [12] G. Calder-Potts and M. Ingg, "A SPACE-BORNE PASSIVE MICROWAVE RADIOMETER FOR THE SPACE PROGRAMME OF A DEVELOPING NATION," in *Geoscience and Remote Sensing Symposium (IGARSS), 2012 IEEE International*, 2012, pp. 4691–4694.
- [13] F. Alimenti, V. Palazzari, A. Battistini, L. Roselli, S. M. White, M. Velli, A. Bigazzi, and F. Berrilli, "A space-based 90 GHz radiometer for the observation of solar flares: Feasibility study," in *Conference Proceedings - 39th European Microwave Conference, EuMC 2009*, 2009, pp. 982–985.
- [14] D. M. Sheen, D. L. McMakin, T. E. Hall, and R. H. Severtsen, "Active millimeter-wave standoff and portal imaging techniques for personnel screening," in *2009 IEEE Conference on Technologies for Homeland Security*, 2009, pp. 440–447.
- [15] L. Gilreath, V. Jain, and P. Heydari, "Design and Analysis of a W-Band SiGe Direct-Detection-Based Passive Imaging Receiver," *IEEE J. Solid-State Circuits*, vol. 46, no. 10, pp. 2240–2252, 2011.
- [16] R. H. Dicke, "The measurement of thermal radiation at microwave frequencies," *Rev. Sci. Instrum.*, vol. 17, pp. 268–275, 1946.
- [17] J. J. Lynch, H. P. Moyer, J. H. Schaffner, Y. Royter, M. Sokolich, B. Hughes, Y. J. Yoon, and J. N. Schulman, "Passive Millimeter-Wave Imaging Module With Preamplified Zero-Bias Detection," *Microw. Theory Tech. IEEE Trans.*, vol. 56, no. 7, pp. 1592–1600, 2008.
- [18] H. Kazemi, G. Nagy, L. Tran, E. Grossman, E. R. Brown, A. C. Gossard, G. D. Boreman, B. Lail, A. C. Young, and J. D. Zimmerman, "Ultra sensitive ErAs/InAlGaAs direct detectors for millimeter wave and THz imaging applications," in *IEEE /MTT-S International Microwave Symposium*, 2007, pp. 1367–1370.
- [19] N. Su, R. Rajavel, P. Deelman, J. N. Schulman, and P. Fay, "Sb-Heterostructure Millimeter-Wave Detectors With Reduced Capacitance and Noise Equivalent Power," *IEEE Electron Device Lett.*, vol. 29, no. 6, pp. 536–539, 2008.
- [20] M. Kaynak, M. Wietstruck, R. Scholz, J. Drews, R. Barth, K. E. Ehwald, A. Fox, U. Haak, D. Knoll, F. Korndörfer, S. Marschmeyer, K. Schulz, C. Wipf, D. Wolansky, B. Tillack, K. Zoschke, T. Fischer, Y. S. Kim, J. S. Kim, W. Lee, and J. W. Kim, "BiCMOS Embedded RF-MEMS Switch for above 90 GHz Applications using Backside

- Integration Technique,” in *IEEE Electron Devices Meeting (IEDM)*, 2010, pp. 832–835.
- [21] P. Song, A. C. Ulusoy, R. L. Schmid, and J. D. Cressler, “A high gain, W-band SiGe LNA with sub-4.0 dB noise figure,” in *IEEE MTT-S International Microwave Symposium (IMS2014)*, 2014, pp. 1–3.
  - [22] A. C. Ulusoy, M. Kaynak, V. Valenta, B. Tillack, and H. Schumacher, “A 110 GHz LNA with 20 dB Gain and 4 dB Noise Figure in an 0.13  $\mu\text{m}$  SiGe BiCMOS Technology,” *IEEE MTT-S International Microwave Symposium Digest (IMS)*, pp. 1–3, 2013.
  - [23] P. Adhikari, “<http://www.loecom.com/pdf>.”
  - [24] I. D. Robertson and S. Lucyszyn, *RFIC and MMIC design and technology*, 2nd ed. The Institution of Engineering and Technology, 2001.
  - [25] “<http://www.ommic.fr/produits/w2190c2-15>.”
  - [26] “<https://www.hrl.com/capabilities/mmics/products/pdf/LN4-110.pdf>.”
  - [27] M. Micovic, A. Kurdoghlian, H. P. Moyer, P. Hashimoto, A. Schmitz, I. Milosavljevic, P. J. Willadsen, W.-S. Wong, J. Duvall, M. Hu, M. Wetzel, and D. H. Chow, “GaN MMIC technology for microwave and millimeter-wave applications,” in *IEEE Compound Semiconductor Integrated Circuit Symposium*, 2005, pp. 173–176.
  - [28] A. Brown, K. Brown, J. Chen, K. C. Hwang, N. Kolas, and R. Scott, “W-band GaN power amplifier MMICs,” in *IEEE MTT-S International Microwave Symposium Digest*, 2011, pp. 1–4.
  - [29] L. Zhou, C. Wang, Z. Chen, and P. Heydari, “A W-band CMOS Receiver Chipset for Millimeter-Wave Radiometer Systems,” *IEEE J. Solid-State Circuits*, vol. 46, no. 2, pp. 378–391, 2011.
  - [30] “IHP Microelectronics, [Online]. Available: <http://www.ihp-microelectronics.com/en/services/mpw-prototyping/sigec-bicmos-technologies.html>. [Accessed 06 August 2013].”
  - [31] A. Gustafsson, C. Samuelsson, R. Malmqvist, S. Seok, M. Fryziel, N. Rolland, B. Grandchamp, and R. Baggen, “A 0-Level Packaged RF-MEMS Switched Wideband GaAs LNA MMIC,” in *European Microwave Conference (EuMC)*, 2013, pp. 1403–1406.
  - [32] “<http://project-nanotec.com/>.”
  - [33] R. Malmqvist et al., “GaAs/SiGe RF-MEMS and MMIC Based Front-End Circuits for W-Band Passive Imaging Application,” in *Workshop at European Microwave Conference*, 2013, pp. 1–28.
  - [34] P. Song, R. L. Schmid, A. Ç. Ulusoy, and J. D. Cressler, “A High-Power, Low-Loss W-band SPDT Switch Using SiGe PIN Diodes,” in *IEEE Radio Frequency Integrated Circuits Symposium*, 2014, pp. 195–198.
  - [35] P. Bacon, “Overview of RF Switch Technology and Applications,” *Microwave Journal*, vol. 57, no. 7, pp. 76–88, 2014.

- [36] G. M. Rebeiz and J. B. Muldavin, "RF MEMS Switches and Switch Circuits," *IEEE Microwave Magazine*, pp. 59–71, 2001.
- [37] G. M. Rebeiz, K. Entesari, I. C. Reines, S. Park, M. A. El-tanani, and A. Grichener, "Tuning in to RF MEMS," *IEEE Microwave Magazine*, no. October, pp. 55–72, 2009.
- [38] M. Daneshmand and R. R. Mansour, "Redundancy RF MEMS Multiport Switches and Switch Matrices," *J. Microelectromechanical Syst.*, vol. 16, no. 2, pp. 296–303, 2007.
- [39] R. Malmqvist, C. Samuelsson, W. Simon, P. Rantakari, D. Smith, M. Lahdes, and M. Lahti, "Design , Packaging and Reliability Aspects of RF MEMS Circuits Fabricated Using a GaAs MMIC Foundry Process Technology," in *European Microwave Conference (EuMC)*, 2010, no. September, pp. 85–88.
- [40] F. Ellinger, U. Mayer, M. Wickert, N. Joram, J. Wagner, R. Eickhoff, S. Ignacio, C. Scheytt, and R. Kraemer, "Integrated Adjustable Phase Shifters," *IEEE Microwave Magazine*, no. October 2010, pp. 97–108, 2010.
- [41] K. Entesari, K. Obeidat, A. R. Brown, and G. M. Rebeiz, "A 25–75-MHz RF MEMS Tunable Filter," *IEEE Trans. Microw. Theory Tech.*, vol. 55, no. 11, pp. 2399–2405, Nov. 2007.
- [42] V. Sekar, M. Armendariz, and K. Entesari, "A 1.2–1.6-GHz Substrate-Integrated-Waveguide RF MEMS Tunable Filter," *IEEE Trans. Microw. Theory Tech.*, vol. 59, no. 4, pp. 866–876, Apr. 2011.
- [43] R. Malmqvist, C. Samuelsson, S. Reyaz, A. Gustafsson, S. Seok, M. Fryziel, P. Rolland, B. Grandchamp, and R. Baggen, "A GaAs MMIC Single-Chip RF-MEMS Switched Tunable LNA," in *Compound Semiconductor Integrated Circuit Symposium (CSICS)*, IEEE, 2013, pp. 15–18.
- [44] R. Malmqvist, C. Samuelsson, P. Rantakari, D. Smith, J. Varis, and R. Baggen, "RF MEMS and MMIC based Reconfigurable Matching Networks for adaptive multi-band RF front-ends," in *RF Front-ends for Software Defined and Cognitive Radio Solutions (IMWS)*, 2010, pp. 2–5.
- [45] T. Vähä-heikkilä and G. M. Rebeiz, "A 4-18-GHz Reconfigurable RF MEMS Matching Network For Power Amplifier Applications," *Int. J. RF Microw. Comput. Eng.*, vol. 14, no. 4, pp. 356–372, Jul. 2004.
- [46] Y. Lu, D. Peroulis, S. Mohammadi, and P. B. L. Katehi, "A MEMS Reconfigurable Matching Network for a Class AB Amplifier," *IEEE Microw. Wirel. Components Lett.*, vol. 13, no. 10, pp. 437–439, 2003.
- [47] S. Cheng, P. Rantakari, R. Malmqvist, C. Samuelsson, T. Vähä-heikkilä, A. Rydberg, and J. Varis, "Switched Beam Antenna Based on RF MEMS SPDT Switch on Quartz Substrate," *IEEE Antennas Wirel. Propag. Lett.*, vol. 8, pp. 383–386, 2009.
- [48] R. Malmqvist, C. Samuelsson, A. Gustafsson, H. Maher, and T. Vähä-heikkilä, "A K-Band Single-Chip Reconfigurable/Multi-



- Functional RF-MEMS Switched Dual-LNA MMIC,” in *Microwave Symposium Digest (MTT), IEEE MTT-S International*, 2012, pp. 10–12.
- [49] A. C. Ulusoy, M. Kaynak, T. Purtova, B. Tillack, and H. Schumacher, “A 60 to 77 GHz Switchable LNA in an RF-MEMS Embedded BiCMOS Technology,” *IEEE Microw. Wirel. Compon. Lett.*, vol. 22, no. 8, pp. 430–432, 2012.
  - [50] A. Ç. Ulusoy, M. Kaynak, T. Purtova, B. Tillack, and H. Schumacher, “24 to 79 GHz frequency band reconfigurable LNA,” *Electron. Lett.*, vol. 48, no. 25, pp. 1598–1600, Dec. 2012.
  - [51] G. M. Rebeiz, *RF MEMS Theory, Design, AND Technology*. Wiley & Sons, New York, 2003.
  - [52] P. Rantakari, R. Malmqvist, C. Samuelsson, R. Leblanc, D. Smith, R. Jonsson, W. Simon, J. Saijets, R. Baggen, and T. Vähä-Heikkiä, “Wide-band radio frequency micro electro-mechanical systems switches and switching networks using a gallium arsenide monolithic microwave-integrated circuits foundry process technology,” *IET Microwaves, Antennas Propag.*, vol. 5, no. 8, pp. 948–955, 2011.
  - [53] M. Kaynak, M. Wietstruck, W. Zhang, J. Drews, R. Barth, D. Knoll, F. Korndörfer, R. Scholz, K. Schulz, C. Wipf, B. Tillack, K. Kaletta, M. Suchodoletz, K. Zoschke, M. Wilke, O. Ehrmann, A. C. Ulusoy, T. Purtova, G. Liu, and H. Schumacher, “Packaged BiCMOS Embedded RF-MEMS Switches with Integrated Inductive Loads,” in *Microwave Symposium Digest (IMS), IEEE MTT-S International*, 2012, pp. 4–6.
  - [54] M. Sterner, N. Somjit, U. Shah, S. Dudorov, D. Chicherin, A. Räisänen, and J. Oberhammer, “Microwave MEMS devices designed for process robustness and operational reliability,” *Int. J. Microw. Wirel. Technol.*, vol. 3, no. 05, pp. 547–563, Oct. 2011.
  - [55] G. M. Rebeiz, C. D. Patel, S. K. Han, and K. M. J. Ho, “The Search for a Reliable MEMS Switch,” *IEEE Microw. Mag.*, vol. 14, no. 1, pp. 57–67, Jan. 2013.
  - [56] “<http://www.wispry.com>.”
  - [57] “<http://www.radantmems.com>.”
  - [58] S. Seok, J. Kim, M. Fryziel, N. Rolland, P. Rolland, H. Maher, W. Simon, and R. Baggen, “Wafer-level BCB CAP Packging of Integrated MEMS Switches with MMIC,” in *IEEE Microwave Symposium Digest (MTT)*, 2012, pp. 8–10.
  - [59] A. Persano, A. Tazzoli, A. Cola, P. Siciliano, G. Meneghesso, and F. Quaranta, “Reliability enhancement by suitable actuation waveforms for capacitive RF MEMS switches in III-V technology,” *J. Microelectromechanical Syst.*, vol. 21, no. 2, pp. 414–419, 2012.
  - [60] M. Kaynak, F. Korndörfer, M. Wietstruck, D. Knoll, R. Scholz, C. Wipf, C. Krause, and B. Tillack, “Robustness and Reliability of BiCMOS Embedded RF-MEMS Switch,” in *IEEE 11th Topical*

- Meeting on Silicon Monolithic Integrated Circuits in RF Systems (SiRF)*, 2011, vol. 1, pp. 177–180.
- [61] K. Chang, *RF and Microwave Wireless Systems*. John Wiley & Sons, INC., 2000.
  - [62] H. T. Friis, “Noise Figures of Radio Receivers,” in *Proceedings of the IRE*, 1944, pp. 419–422.
  - [63] J. C. Orlhac, P. Baudet, G. Dambrine, and T. Närhi, “Millimeter Wave MMIC LNA for Future Atmospheric Sounders,” in *ESA Proc. of the Microwave technique workshop*, 2006, no. 1.
  - [64] D. Smith, G. Dambrine, and J. Orlhac, “Industrial MHEMT Technologies for 80 - 220 GHz Applications,” in *European Microwave Integrated Circuit Conference, EuMIC*, 2008, no. October, pp. 214–217.
  - [65] S. Reyaz, R. Malmqvist, A. Gustafsson, and M. Kaynak, “SiGe BiCMOS high-gain and wideband differential intermediate frequency amplifier for W-band passive imaging single-chip receivers,” *IET Microwaves, Antennas Propag.*, vol. doi: 10.10, pp. 1–7.
  - [66] R. Jonsson, C. Samuelsson, S. Reyaz, R. Malmqvist, A. Gustafsson, M. Kaynak, and A. Rydberg, “SiGe wideband power detector and IF-amplifier RFICs for W-band passive imaging systems,” in *International Semiconductor Conference (CAS)*, 2013, pp. 225–228.
  - [67] A. Tomkins, P. Garcia, and S. P. Voinigescu, “A passive W-band imaging receiver in 65-nm bulk CMOS,” *IEEE J. Solid-State Circuits*, vol. 45, pp. 1981–1991, 2010.
  - [68] R. Malmqvist, A. Gustafsson, M. Danestig, S. Rudner, and C. Svensson, “Noise and temperature behaviour of tuneable recursive active MMIC-filters for on-chip receivers,” in *Radio Science and Communication (RVK), Karlskrona, Sweden*, 1999, pp. 232–236.
  - [69] C. Wang, Z. Chen, H. Yao, and P. Heydari, “A Fully Integrated 96GHz 2×2 Focal-Plane Array with On-Chip Antenna,” in *Radio Frequency Integrated Circuits Symposium (RFIC)*, 2011, pp. 1–4.
  - [70] G. Fischer, W. Eckl, and G. Kaminski, “RF-MEMS and SiC/GaN as enabling technologies for a reconfigurable multi-band/multi-standard radio,” *Bell Labs Tech. J.*, vol. 7, no. 3, pp. 169–189, Mar. 2003.
  - [71] R. L. Schmid, A. Ç. Ulusoy, P. Song, and J. D. Cressler, “A 94 GHz, 1.4 dB Insertion Loss Single-Pole Double-Throw Switch Using Reverse-Saturated SiGe HBTs,” *IEEE Microw. Wirel. Components Lett.*, vol. 24, no. 1, pp. 56–58, 2014.
  - [72] I. Kallfass, S. Diebold, H. Massler, S. Koch, M. Seelmann-Eggebert, and A. Leuther, “Multiple-throw millimeter-wave FET switches for frequencies from 60 up to 120 GHz,” in *European Microwave Integrated Circuit Conference, EuMIC*, 2008, no. October, pp. 426–429.
  - [73] J. Putnam, M. Fukuda, P. Staecker, and Y. Yun, “A 94 GHz Monolithic Switch with a Vertical PIN Diode Structure,” in *Gallium*

- Arsenide Integrated Circuit (GaAs IC) Symposium, Technical Digest*, 1994, pp. 333–336.
- [74] F. Steinhagen, H. Massler, W. H. Haydl, A. Hülsmann, and K. Köhler, “Coplanar W-band SPDT and SPTT resonated PIN diode switches,” in *European Microwave Conference, EuMC*, 1999, vol. 2, pp. 53–56.
  - [75] A. Fukuda, H. Okazaki, and S. Narahashi, “A Novel Compact Reconfigurable Quad-band Power Amplifier Employing RF-MEMS Switches,” in *European Microwave Conference*, 2006, no. September, pp. 344–347.
  - [76] R. Molfino, S. M. Lardizabal, B. Pillans, P. M. Asbeck, and G. Jerinic, “An intelligently controlled RF power amplifier with a reconfigurable MEMS-varactor tuner,” *IEEE Trans. Microw. Theory Tech.*, vol. 53, no. 3, pp. 1089–1095, Mar. 2005.
  - [77] K. Joshin, Y. Kawano, X. Mi, O. Toyoda, T. Suzuki, T. Hirose, and S. Ueda, “K-band CMOS-Based Power Amplifier Module with MEMS Tunable Bandpass Filter,” in *European Microwave Integrated Circuit Conference, EuMIC*, 2010, no. September, pp. 440–443.
  - [78] R. Malmqvist, C. Samuelsson, W. Simon, D. Smith, P. Rantakari, S. Reyaz, and J. Varis, “Reconfigurable Wideband LNAs Using Ohmic Contact and Capacitive RF-MEMS Switching Circuits,” in *Microwave Integrated Circuits Conference (EuMIC)*, 2011, no. October, pp. 160–163.
  - [79] R. Malmqvist, C. Samuelsson, A. Gustafsson, P. Rantakari, S. Reyaz, T. Vähä-Heikkilä, A. Rydberg, J. Varis, D. Smith, and R. Baggen, “A K-Band RF-MEMS-Enabled Reconfigurable and Multifunctional Low-Noise Amplifier Hybrid Circuit,” *Act. Passiv. Electron. Components*, vol. 2011, pp. 1–7, 2011.
  - [80] S. Fouladi and R. R. Mansour, “Reconfigurable Amplifier with Tunable Impedance Matching Networks Based on CMOS-MEMS Capacitors in 0.18- $\mu\text{m}$  CMOS Technology,” in *Microsystems and Nanoelectronics Research Conference*, 2009, no. c, pp. 33–36.
  - [81] T. Mukherjee and G. K. Fedder, “RF-CMOS-MEMS based frequency-reconfigurable amplifiers,” in *IEEE Custom Integrated Circuits Conference*, 2009, no. Cicc, pp. 81–84.
  - [82] M. Kim, J. B. Hacker, R. E. Mihailovich, and J. F. DeNatale, “A monolithic MEMS switched dual-path power amplifier,” *IEEE Microw. Wirel. Components Lett.*, vol. 11, no. 7, pp. 285–286, 2001.
  - [83] J. B. Hacker, M. Kim, R. E. Mihailovich, and J. F. DeNatale, “Monolithic GaAs PHEMT MMICs integrated with RF MEMS switches,” *Tech. Dig. - IEEE Compd. Semicond. Integr. Circuit Symp. CSIC*, pp. 229–232, 2004.
  - [84] E. Shumakher, J. Elkind, and D. Elad, “Key components of a 130 GHz Dicke-radiometer SiGe RFIC,” in *IEEE 13th Topical Meeting*

- on *Silicon Monolithic Integrated Circuits in RF Systems*, 2013, pp. 255–257.
- [85] T. Kosugi, H. Sugiyama, H. Matsuzaki, K. Murata, M. Nakamura, H. Satoh, and K. Thongnumchai, “A 140-GHz quad-receivers IC and sub-assembly for compact passive imaging sensors,” in *IEEE MTT-S International Microwave Symposium Digest*, 2012, pp. 1–3.
  - [86] N. Gopalsami, S. Bakhtiari, T. W. II Elmer, and A. C. Raptis, “Application of Millimeter-Wave Radiometry for Remote Chemical Detection,” *IEEE Trans. Microw. Theory Tech.*, vol. 56, no. 3, pp. 700–709, 2008.
  - [87] F. Alimenti, G. Tasselli, S. Bonafoni, D. Zito, and L. Roselli, “Inter-Wall Fire Detection by Low-Cost Microwave Radiometric Sensors,” in *European Microwave Conference, EuMC*, 2008, no. October, pp. 63–66.
  - [88] D. C. W. Lo, H. Wang, B. R. Allen, G. S. Dow, K. W. Chang, M. Biedenbender, R. Lai, S. Chen, and D. Yang, “Novel Monolithic Multifunctional Balanced Switching Low-Noise Amplifiers,” *IEEE Trans. Microw. Theory Tech.*, vol. 42, no. 12, pp. 2629–2634, 1994.
  - [89] S. Reyaz, C. Samuelsson, R. Malmqvist, S. Seok, M. Fryziel, P. Rolland, B. Grandchamp, and P. Rantakari, “W-BAND RF-MEMS DICKE SWITCH NETWORKS IN A GaAs MMIC PROCESS,” *Microw. Opt. Technol. Lett.*, vol. 55, no. 12, pp. 2849–2853, 2013.
  - [90] M. Kaynak, K. E. Ehwald, J. Drews, R. Scholz, F. Korndörfer, D. Knoll, B. Tillack, R. Barth, K. Schulz, Y. M. Sun, D. Wolansky, S. Leidich, S. Kurth, and Y. Gurbuz, “BEOL Embedded RF-MEMS Switch for mm-Wave Applications,” in *IEEE Electron Devices Meeting (IEDM)*, 2009, pp. 797–800.
  - [91] M. Kaynak, K. E. Ehwald, R. Scholz, F. Korndörfer, C. Wipf, Y. M. Sun, B. Tillack, S. Zehir, Y. Gurbuz, I. Technologiepark, and F. Oder, “Characterization of an Embedded RF-MEMS Switch,” in *SiRF Tech. Digest*, 2010, pp. 144–147.
  - [92] R. Wilke, S. Hamid, K. Schraml, R. Khunti, and D. Herberling, “Multi-layer patch antenna array design for Ka-band satellite communication,” in *International Microwave & Optoelectronics Conference (IMOC)*, 2013, pp. 1–4.
  - [93] C. Miquel, J. C. Cayrou, and J. L. Cazaux, “Flexible Ka-Band Low Noise Amplifier Sub-System for Oncoming Satellite Payloads,” in *European Microwave Conference*, 2006, no. September, pp. 890–893.
  - [94] E. Schreiber, S. Anger, and M. Peichl, “Design of an integrated Ka band receiver module for passive microwave imaging systems,” in *Semiconductor Conference Dresden (SCD)*, 2011, pp. 1–4.
  - [95] L. Aluigi, F. Alimenti, and L. Roselli, “Design of a Ka-Band LNA for SoC space-based millimeter-wave radiometers,” in *IEEE MTT-S*

- International Microwave Workshop Series on Millimeter Wave Integration Technologies*, 2011, pp. 156–159.
- [96] P. J. Riemer, B. R. Buhrow, J. D. Coker, B. A. Randall, R. W. Techentin, B. K. Gilbert, and E. S. Daniel, “Ka-Band (35 GHz) 3-Stage SiGe HBT Low Noise Amplifier,” in *IEEE Microwave Symposium Digest (MTT)*, 2005, no. C, pp. 1037–1040.
  - [97] T. Masuda, T. Nakamura, M. Tanabe, N. Shiramizu, S. Wada, T. Hashimoto, and K. Washio, “SiGe HBT based 24-GHz LNA and VCO for Short-Range Ultra-Wideband Radar Systems,” in *IEEE Asian Solid-State Circuits Conference*, 2005, pp. 425–428.
  - [98] B. Min and G. M. Rebeiz, “Ka-Band SiGe HBT Low Noise Amplifier Design for Simultaneous Noise and Input Power Matching,” *IEEE Microw. Wirel. Components Lett.*, vol. 17, no. 12, pp. 891–893, 2007.
  - [99] P. K. Saha, S. Shankar, R. Schmid, R. Mills, J. D. Cressler, and G. Tech, “Analysis and Design of a 3-26 GHz Low-Noise Amplifier in SiGe HBT Technology,” in *IEEE Radio and wireless Symposium (RWS)*, 2012, pp. 203–206.
  - [100] F. F. Dai, R. C. Jaeger, and J. D. Irwin, “An 8 – 18 GHz wideband SiGe BiCMOS low noise amplifier,” in *IEEE Microwave Symposium Digest (IMS)*, 2009, pp. 929–932.
  - [101] L. Zheng, L. Gilreath, V. Jain, and P. Heydari, “Design and Analysis of a W-Band Detector in 0.18-  $\mu$ m SiGe BiCMOS,” in *Silicon Monolithic Integrated Circuits in RF Systems (SiRF), Topical Meeting*, 2010, no. 1, pp. 196–199.
  - [102] B. Agarwal, Q. Lee, R. Pallela, D. Mensa, J. Guthrie, and M. J. W. Rodwell, “A Transferred-Substrate HBT Wide-band Differential Amplifier to 50 GHz,” *IEEE Microw. Guid. Wave Lett.*, vol. 8, no. 7, pp. 263–265, Jul. 1998.
  - [103] S. Trotta, H. Knapp, K. Aufinger, T. F. Meister, J. Böck, B. Dehlink, W. Simbürger, and A. L. Scholtz, “An 84 GHz Bandwidth and 20 dB Gain Broadband Amplifier in SiGe Bipolar Technology,” *IEEE J. Solid-State Circuits*, vol. 42, no. 10, pp. 2099–2106, 2007.
  - [104] D. C. Howard, J. Poh, T. S. Mukerjee, and J. D. Cressler, “A 3–20 GHz SiGe HBT Ultra-Wideband LNA with Gain and Return loss control for Multiband Wireless Applications,” in *53rd IEEE International Midwest Symposium on Circuits and Systems*, 2010, pp. 445–448.
  - [105] R. Chan and M. Feng, “Low Noise, and High Gain Wideband Amplifier Using SiGe HBT Technology,” in *IEEE MTT-S International Microwave Symposium Digest*, 2004, pp. 21–24.
  - [106] J. Kim, J. Plouchart, N. Zamdmer, R. Trzcenski, R. Groves, M. Sherony, Y. Tan, M. Talbi, J. Safran, and L. Wagner, “A 12dBm 320GHz GBW Distributed Amplifier in a 0.12  $\mu$ m SOI CMOS,” in *IEEE Int. Solid-State Circuits Conference*, 2004, pp. 478–540.

- [107] D. Platt, L. Pettersson, and M. Salter, "Broadband 65nm CMOS SOI LNA for a 100Gbit/s fiber-optic SCM transceiver," in *European Microwave Integrated Circuits Conference (EuMIC)*, 2012, pp. 16–19.
- [108] C. Feng, X. P. Yu, W. M. Lim, and K. S. Yeo, "A Compact 2.1-39 GHz Self-Biased LOW-Noise Amplifier in 65 nm CMOS Technology," *IEEE Microw. Wirel. Components Lett.*, vol. 23, no. 12, pp. 662–664, 2013.
- [109] J. Yoon and C. Park, "A CMOS LNA Using a Harmonic Rejection Technique to Enhance Its Linearity," *IEEE Microw. Wirel. Components Lett.*, vol. 24, no. 9, pp. 605–607, 2014.
- [110] S. P. Sah, Y. You, P. Agarwal, and D. Heo, "A 8-40 GHz, 8 mW LNA with 27 dB Peak Gain and 5.2 dB NF for Multiband Applications," in *Proc. of 9th European Microwave Integrated Circuits Conference*, 2014, pp. 182–185.



# Acta Universitatis Upsaliensis

*Digital Comprehensive Summaries of Uppsala Dissertations  
from the Faculty of Science and Technology 1220*

Editor: The Dean of the Faculty of Science and Technology

A doctoral dissertation from the Faculty of Science and Technology, Uppsala University, is usually a summary of a number of papers. A few copies of the complete dissertation are kept at major Swedish research libraries, while the summary alone is distributed internationally through the series Digital Comprehensive Summaries of Uppsala Dissertations from the Faculty of Science and Technology. (Prior to January, 2005, the series was published under the title "Comprehensive Summaries of Uppsala Dissertations from the Faculty of Science and Technology".)

Distribution: [publications.uu.se](http://publications.uu.se)  
urn:nbn:se:uu:diva-239435



ACTA  
UNIVERSITATIS  
UPSALIENSIS  
UPPSALA  
2015